

MEMOIRS
OF THE
FACULTY OF ENGINEERING
OSAKA CITY UNIVERSITY

VOL. 61

DECEMBER 2020

PUBLISHED BY THE
GRADUATE SCHOOL OF ENGINEERING
OSAKA CITY UNIVERSITY

This series of Memoirs is issued annually. Selected original works of the members of the Faculty of Engineering are compiled in the first part of the volume. Abstracts of papers presented elsewhere during the current year are compiled in the second part. List of conference presentations delivered during the same period is appended in the last part.

All communications with respect to Memoirs should be addressed to:

Dean of the Graduate School of Engineering
Osaka City University
3-3-138, Sugimoto, Sumiyoshi-ku
Osaka 558-8585, Japan

Editors

Eiji SHIKOH
Hayato NAKATANI
Masafumi MURAJI
Shigeyoshi NAKAJIMA
Kingo ARIYOSHI
Yuichiro NISHINO
Satoshi MIZUTANI

MEMOIRS OF THE FACULTY OF ENGINEERING OSAKA CITY UNIVERSITY

VOL. 61

DECEMBER 2020

CONTENTS

Regular Articles	1
------------------------	---

Physical Electronics and Informatics

Electrical and Information Engineering

An Estimation of the Number of Users by Backoff Time Distribution with Frozen Backoff in CSMA/CA

<i>Koki SAMOTO, Ikuo OKA, and Shingo ATA</i>	1
--	---

Urban Engineering

Urban Design and Engineering

Study on Pedestrian Traffic Flow in Crowded Conditions Using Mobile Location Data

<i>Naotaka NISHIMURA and Nagahiro YOSHIDA</i>	9
---	---

Abstracts of Papers Published in Other Journals	15
<i>Mechanical and Physical Engineering</i>	
<i>Mechanical Engineering</i>	17
<i>Physical Electronics and Informatics</i>	
<i>Applied Physics and Electronics</i>	22
<i>Electrical and Information Engineering</i>	30
<i>Applied Chemistry and Bioengineering</i>	
<i>Applied Chemistry and Bioengineering</i>	33
<i>Urban Engineering</i>	
<i>Architecture and Building Engineering</i>	52
<i>Urban Design and Engineering</i>	55
 List of Presentations at International Conferences	 65
<i>Mechanical and Physical Engineering</i>	
<i>Mechanical Engineering</i>	67
<i>Physical Electronics and Informatics</i>	
<i>Applied Physics and Electronics</i>	68
<i>Electrical and Information Engineering</i>	70
<i>Applied Chemistry and Bioengineering</i>	
<i>Applied Chemistry and Bioengineering</i>	71
<i>Urban Engineering</i>	
<i>Urban Design and Engineering</i>	72

MEMOIRS
OF THE
FACULTY OF ENGINEERING
OSAKA CITY UNIVERSITY

VOL. 61

DECEMBER 2020

PUBLISHED BY THE
GRADUATE SCHOOL OF ENGINEERING
OSAKA CITY UNIVERSITY

An Estimation of the Number of Users by Backoff Time Distribution with Frozen Backoff in CSMA/CA

Koki SAMOTO*, Ikuo OKA**, and Shingo ATA***

(Received October 31, 2020)

Synopsis

Recently, with the increased demand for wireless communications, the degradation of communication efficiency due to the concentration of connections to one of AP's has become a serious problem. In order to improve the communication efficiency, the number of users is an important parameter.

In this paper, an estimation method is proposed for the number of users using the probability distribution of backoff. The probability distribution is derived considering frozen backoff. The number of users is obtained by the maximum likelihood estimation with the derived probability distribution of backoff time.

Keywords: CSMA/CA, DCF, Backoff time distribution, Estimation of users, Frozen backoff

1.Introduction

In Recent years, the demand for wireless communication is increasing, and a wireless LAN is used widely in public facilities, businesses, and homes. The wireless LAN employs CSMA/CA (Carrier Sense Multiple Access with Collision Avoidance) as MAC (Medium Access Control) protocols. One of the features of CSMA/CA is the backoff algorithm to avoid collisions, where a user sends a packet after a random delay time. New backoff algorithm are proposed to improve network performance¹⁾²⁾.

In the wireless LAN, users communicate with other users by a relay access point (AP). When an access is concentrated on the same AP, the collision probability increases and the communication efficiency decreases. An algorithm was proposed that maximizes the minimum throughput of a node and selects the best AP³⁾. An AP selection and a load balancing are discussed to improve throughput based on the number of users connected to the AP⁴⁾.

The estimation of number of users is presented by an extended Kalman filter with measured number of collisions⁵⁾. The maximum likelihood estimation is applied to the probability distribution of backoff time in order to obtain the number of users⁶⁾. However, a frozen backoff time is not included in the analysis, which yields misestimation results in the frozen backoff environments.

* Student, Master Course of Department of Electrical and Information Engineering

** Professor, Department of Electrical and Information Engineering

*** Professor, Department of Electrical and Information Engineering

In this paper, an estimation method is proposed for the number of users using probability distribution of backoff considering frozen backoff. The analysis method is presented to derive the probability distribution of backoff time with frozen backoff in time axis. For 2 users, the Markov state transition diagram is considered for all possible combinations of backoff time, and the relation at time $t - 1$ and time t is derived. For 3 users or more, a time axis analysis is extended by assuming statistical independence of probability distribution in the target user and other users. As a result, the calculation time can be reduced from the exponential increase to the linear increase, as the number of users increases. Then, the number of users is obtained by the maximum likelihood estimation using the probability distribution of backoff time. Numerical results for the number of users demonstrate the estimation performance in the frozen backoff environments.

2.CSMA/CA

In CSMA/CA, each user trying to transmit a packet performs carrier sense and checks the usage status of the channel. After the channel becomes idle for the DIFS (DCF Inter Frame Space), the user generates a random number within the specified CW (Contention Window) range, and the backoff time is determined. In IEEE802.11, backoff time follows as

$$b = r \cdot s$$

where r is a random integer generated from a uniform distribution of $[0, CW - 1]$, and s is a slot time. CW is an integer between CW_{min} and CW_{max} , and determined by

$$CW = CW_{min} \times 2^m$$

where m is a number of collisions. The determined backoff time decreases for each slot time in the case of channel idle, and when it reaches 0, the user transmits a packet. In the case of channel busy, the backoff time is frozen and carried over to the next transmission opportunity.

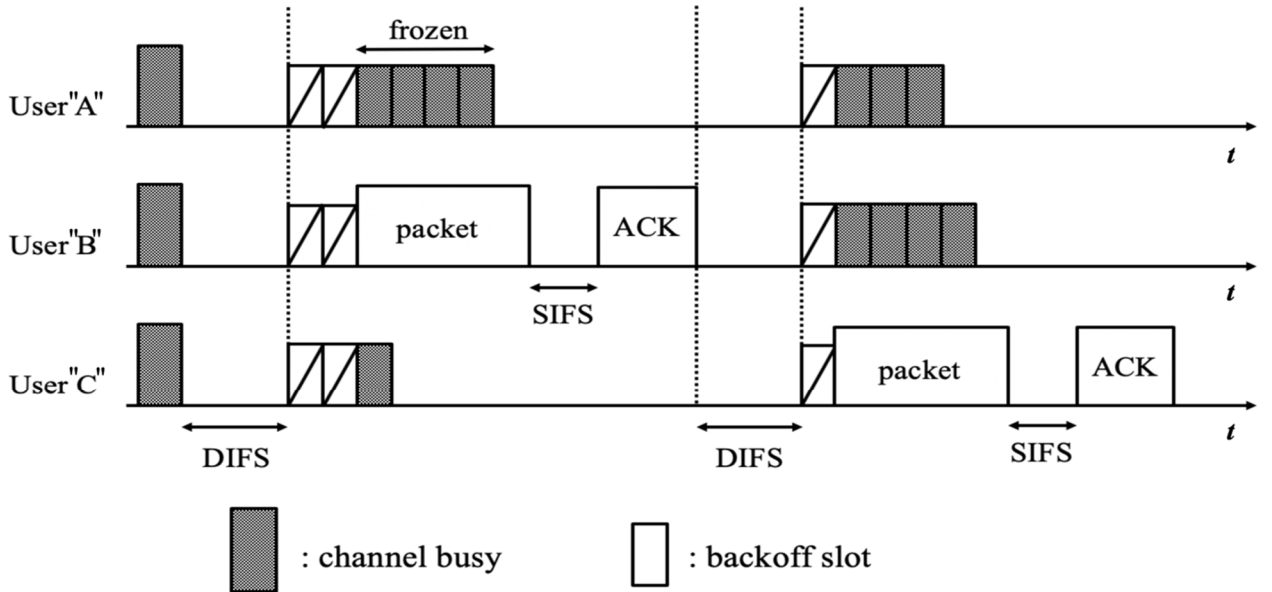


Figure 1: Example of packet transmission in CSMA/CA

Fig.1 shows an example of packet transmission in CSMA/CA. Users "A", "B" and "C" are attempting to transmit a packet to the AP. In this paper, "X" denotes the user, and X denotes a random variable of backoff slot of user "X". After each user is idle for DIFS, it uses a random number generator to set a backoff time. It is assumed that the backoff time's are set to $6 \cdot s$ for user "A", $2 \cdot s$ for user "B", and $3 \cdot s$ for user "C". User "B" with the shortest backoff time transmits a packet first. After the reception of the packet is completed, the AP sends an ACK frame after SIFS, and the packet transmission is completed. While user "B" is using the channel, users "A" and "C" freeze the decrease in backoff time. The frozen backoff time's are carried over to the next transmission opportunity. The backoff time is set again for user "B", and the same process is repeated.

3.Backoff analysis

In this section, the probability distribution of backoff time x of transmitted user with frozen backoff is derived in time axis. A window size is set to 15, and the backoff stage is not considered.

An illustrative example of the proposed time axis analysis for $N = 2$ is shown in Fig.2 (a). At time $t - 1$, it is assumed that the backoff time's are set to $7 \cdot s$ for user "A" and $4 \cdot s$ for user "B". At time t , user "A" is set to $3 \cdot s$, which has been frozen, and user "B" is reset to $x \cdot s (x: [0, 1, \dots, CW - 1])$. For all possible backoff slot combinations, the relation between time $t - 1$ and time t is expressed by

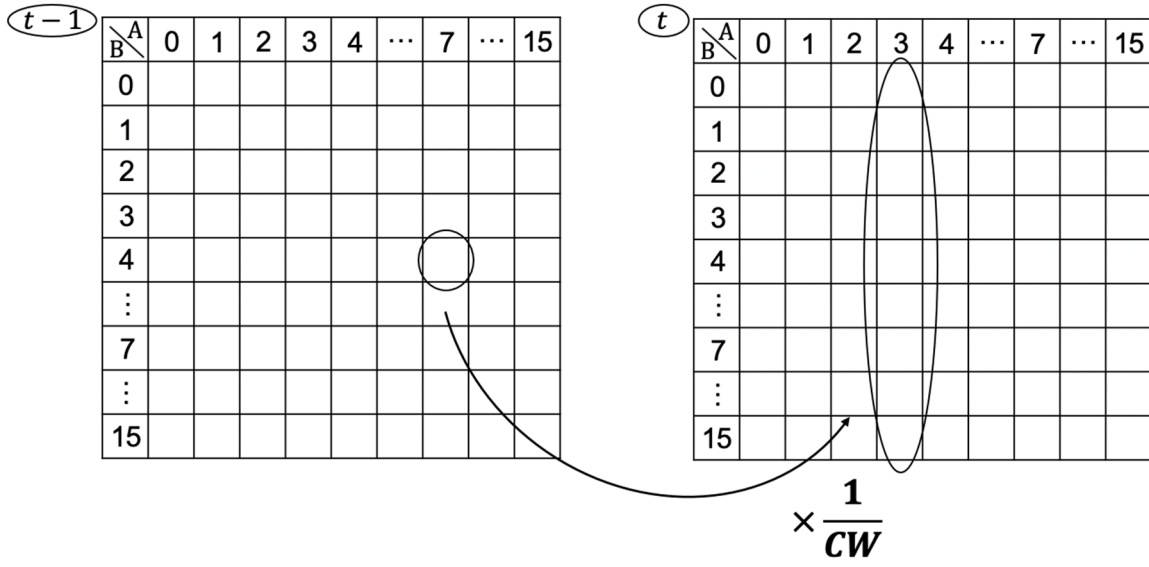
$$P_{\alpha,\beta}^{(t)} = \begin{cases} K & (\alpha = \beta = 0) \\ K + \left(\sum_{i=\alpha}^{CW-1} P_{i,i-\alpha}^{(t-1)} \right) \times \frac{1}{CW} \\ \quad + \left(\sum_{j=\beta}^{CW-1} P_{j-\beta,j}^{(t-1)} \right) \times \frac{1}{CW} & (otherwise) \end{cases}$$

where $P_{\alpha,\beta}^{(t)}$ is the occurrence probability of the combination of backoff slots of users "A" and "B" at time t , and

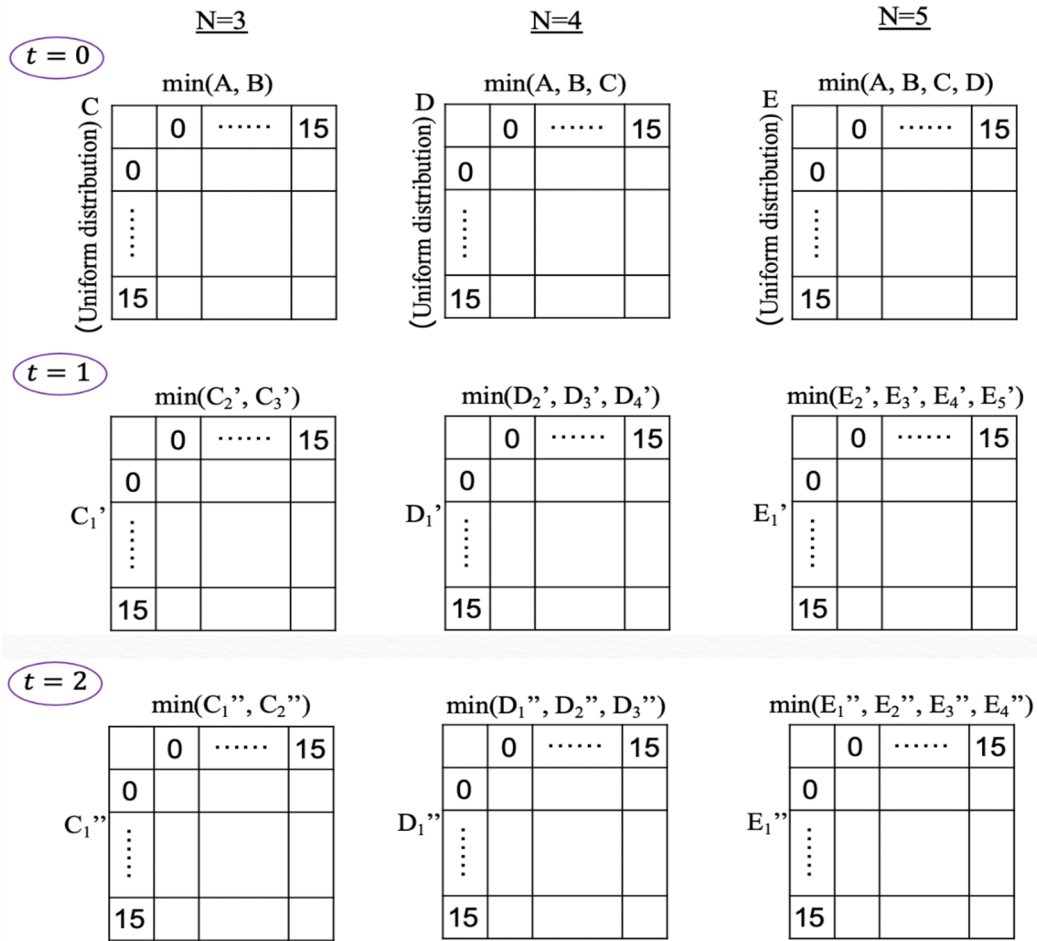
$$K = \left(\sum_{i=0}^{CW-1} P_{i,i}^{(t-1)} \right) \times \frac{1}{CW^2}$$

Iterative calculations are executed for $P_{\alpha,\beta}^{(t)}$ until the steady state is obtained. The results of the probability distribution of observed backoff is shown by the solid line $N = 2$ in Fig.3 (a).

Fig.2 (b) shows the time axis analysis when the number of users N is 3 or more. The row represents the number of backoff slots for the target user, and the column represents the minimum number of backoff slots for the other $N - 1$ users. We assume the statistical independence among probability distributions. When the number of users is 3, at $t = 0$, the element of row is a random variable C for user "C" which follows a uniform distribution, and the element of column is given by the probability distribution of the minimum value of the uniform distribution of two users "A" and "B", $\min(A, B)$ where A and B denote backoffs for user "A" and "B" respectively. The distribution of $\min(A, B)$ is derived by the distributions of A and B . At $t = 1$, the row is given by a backoff C_1' which is a result of $\min(A, \min(A, B))$ of $t = 0$. The column is given by $\min(C_2', C_3')$, where C_2' and C_3' have the independent identical distribution as that of C_1' . Similarly, when the number of users is 4, at $t = 0$, the row is given by a uniform distribution of user "D", and the column is given by the probability distribution of the minimum value of the uniform distribution of three users, $\min(A, B, C)$. At $t = 1$, the row is a backoff D_1' , which is a result of $\min(D, \min(A, B, C))$. The column is obtained by $\min(D_2', D_3', D_4')$, where D_2' , D_3' and D_4' have the independent identical distribution



(a) $N = 2$

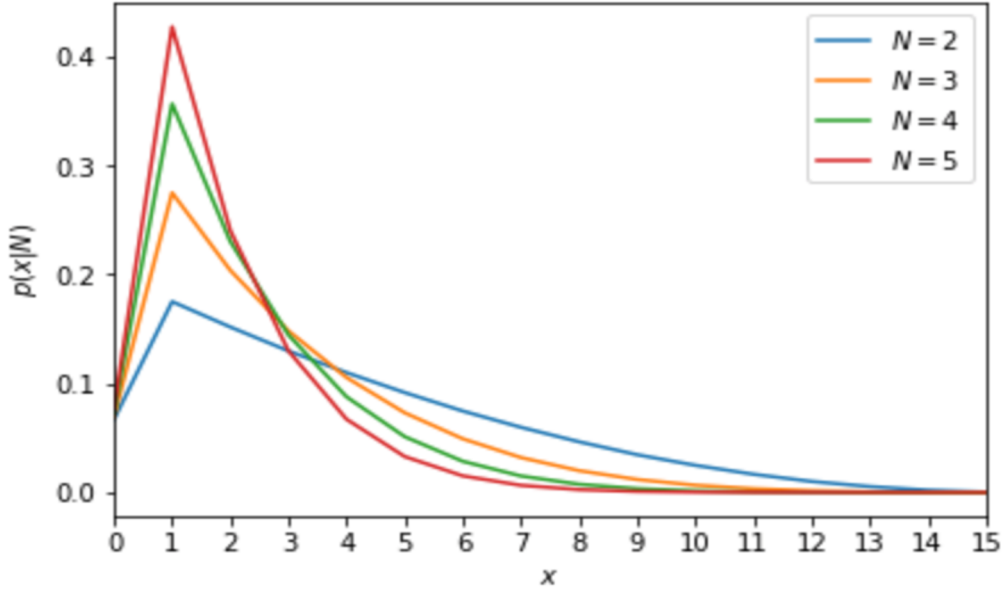


(b) $N \geq 3$

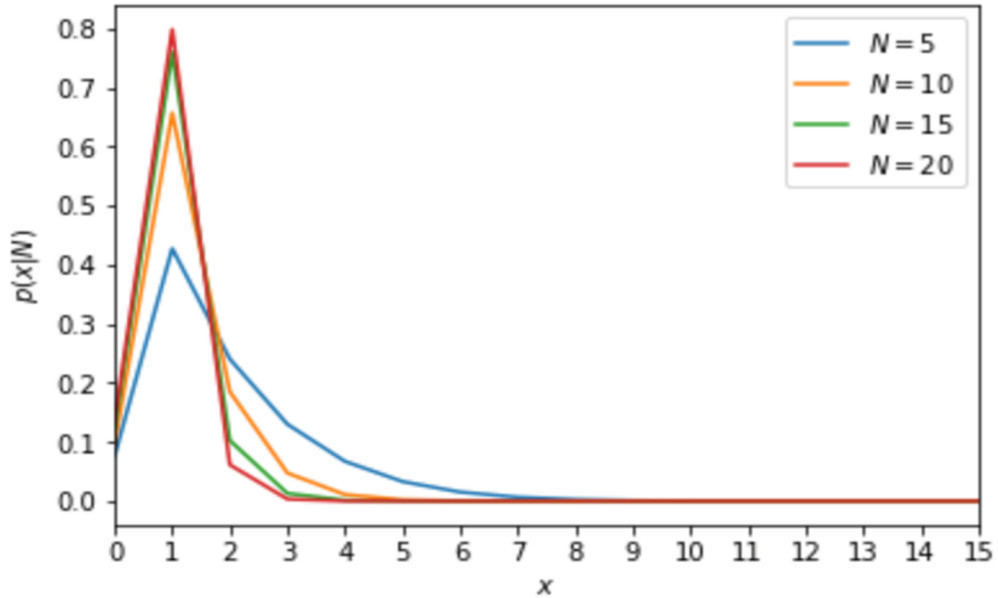
Figure2: Illustrative example of the proposed time axis analysis

as that of D_1' . For $N \geq 5$, the backoff distribution of transmitted user is derived as well as the cases of $N = 3$ and 4. Numerical calculations are executed until the steady state is obtained. The probability distributions of observed backoff for $N \geq 3$ is shown by solid line in Fig.3 (a) and Fig.3 (b).

As a result, the calculation time can be reduced from the exponential increase to the linear increase as the number of users increases. The simulation results are also depicted in Fig.3 (a) and Fig.3 (b). The analytical results have a good coincidence with the simulation results, and the validity of the proposed time axis analysis.



(a) $N = 2, 3, 4, 5$



(b) $N = 5, 10, 15, 20$

Figure 3: The probability distribution of observed backoff

4. Estimation of the number of users

The number of users is obtained by the maximum likelihood estimation using the probability distribution of the observed backoff derived in Section III. For the number of users, N , the likelihood function $L(N)$ is given by

$$L(N) = \prod_I p_N(x_i)$$

where x_i is the number of backoff slots observed at time i , $p_N(x_i)$ is the probability of x_i when the number of users is N . The estimated number \hat{N} is given by

$$\hat{N} = \operatorname{argmax} L(N)$$

Fig.4 shows the estimation results for $N = 5, 10, 15, 20$. The number of observations or samples is 2000. When $N = 20$, it is estimated from 17 to 24. As N is decreased, the estimation accuracy is improved, and when $N = 5$, there is no estimation error. Fig.4 is compared with the results of Ref.8) to confirm with the validity of the proposed method. It is found that estimation results of the proposed method and Ref.8) have a good coincidence, while the backoff distribution is given by computer simulations in Ref.8).

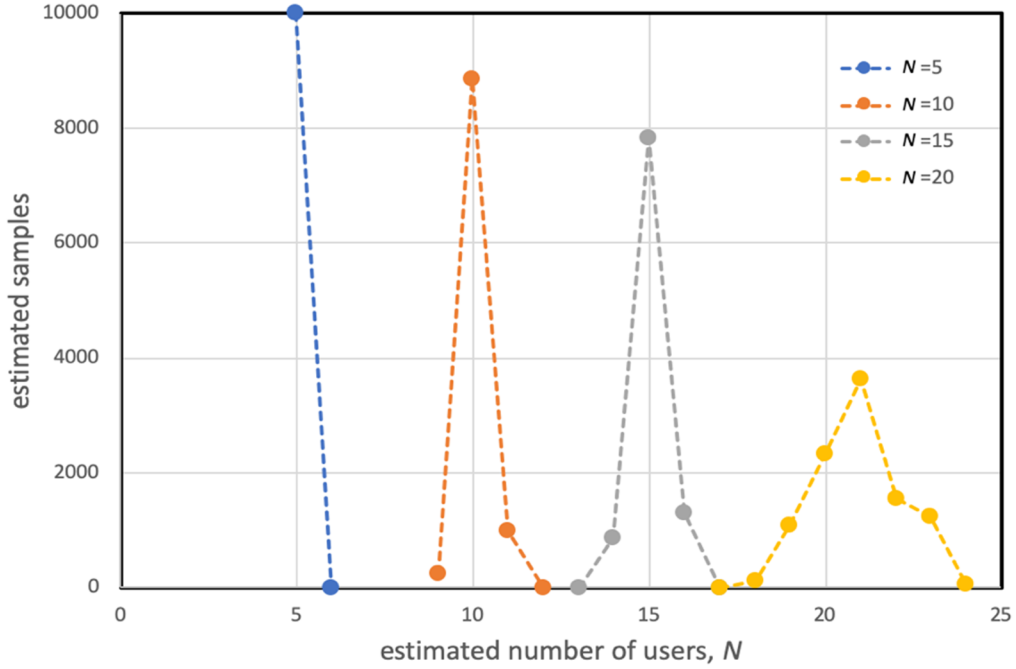


Figure 4: Estimation results for the number of users

5. Conclusions

In this paper, an analysis method has been presented for the probability distribution of backoff time with frozen backoff in time axis. For 2 users, the Markov state transition diagram for all possible combinations of backoff times gives the relation of distribution at time $t - 1$ and time t . For 3 users or more, a time axis analysis has been extended by assuming statistical independence of probability distribution in the target user and other users. The number of users has been estimated by maximum likelihood estimation using the probability distribution of backoff time. The estimation result has been shown to confirm the validity the proposed method.

6.References

- 1) Nah-Oak Song, Byung-Jae Kwak, Jabin Song, and Leonard E.Miller, "Enhancement of IEEE 802.11 Distributed Coordination Function with Exponential Increase Exponential Decrease Backoff Algorithm," *The 57th IEEE Semiannual Vehicular Technology Conference 2003*, VTC 2003-Spring.IEEE, vol.4, pp.2775-2778, 2003.
- 2) Xinghua Sun and Lin Dai, "A Comparative Study of Quadratic Backoff and Binary Exponential Backoff in IEEE 802.11 DCF Networks," *2011 45th Annual Conference on Information Sciences and Systems*, pp.1-6, 2011.
- 3) Fengyuan Xu, Xiaojun Zhu, Chiu C. Tan, Qun Li, Guanhua Yan, and Jie Wu, "SmartAssoc: Decentralized Access Point Selection Algorithm to Improve Throughput," *IEEE transactions on Parallel and distributed systems*, 24(12), 2482-2491.
- 4) Uferah Shafi, Muhammad Zeeshan, Naveed Iqbal, Nadia Kalsoom, and Rafia Mumtaz, "An Optimal Distributed Algorithm for Best AP Selection and Load Balancing in WiFi," pp.65-69, 2001.
- 5) Giuseppe Bianchi and Ilenia Tinnirello, "Kalman Filter Estimation of the Number of Competing Terminals in an IEEE 802.11 network," *Proc. IEEE International Conference on Computer Communications 2003*, vol.1-3, pp.844-852, 2003.
- 6) Norihiro Matsumoto, Ikuo Oka, and Shingo Ata, "Number of Users Estimated by Statistics of Random Backoff Time in WiFi Networks," *Proc. RISP International Workshop on Nonlinear Circuits, Communications and Signal Processing*, pp.267-270, 2018.
- 7) A.Papoulis, *Probability, Random Variables, and Stochastic Processes*, Tokyo: McGraw-Hill Kogakusha, pp.193, 1965.
- 8) Norihiro Matsumoto, Ikuo Oka, and Shingo Ata, "Estimation of Number of Users by Backoff Distribution with Frozen Backoff in RLAN," *The 41st Symposium on Information Theory and its Applications (SITA2018)*, 2018.

Study on Pedestrian Traffic Flow in Crowded Conditions Using Mobile Location Data

Naotaka NISHIMURA* and Nagahiro YOSHIDA**

(Received November 19, 2020)

Abstract

In recent years, in Japan, the number of incidents involving large crowds has been increasing for several reasons, including the increase in the number of such time-intensive events as sports events and concerts, the increase in the number of tourists, and the paralysis of traffic functions caused by natural disasters. However, the increasing sophistication of information and communication technologies and smart phones has increased the technological possibilities and improved crime prediction systems, leading to the development of pedestrian agent simulations and the analysis of crowd conditions using big data. However, there is still a lack of knowledge on crowd control at the micro level of events, such as fireworks displays and disasters. The purpose of this study was to gain new knowledge on how to understand and control crowd behavior at events by analyzing mobile location data obtained from smartphones.

KEYWORDS: crowd behavior, mobile location data, $K-V$ scatter map

1. Introduction

In recent years, the number of crowd incidents has increased because of an increase in the number of time-intensive events, such as sports and concerts, as well as the paralysis of traffic functions during natural disasters. Around the world, there have also been such crimes as mobbing and molestation in crowds, such as the sexual assault at the Etoile Arc de Triomphe during the 2018 soccer World Cup celebrations and the light truck incident at Shibuya Halloween 2018.

However, because of the sophistication of information and communication technology, in many countries, pedestrian simulation and crowd analysis using big data have been conducted. In Japan, the prediction of crowd behavior by simulation¹⁾, the analysis of crowd wave phenomena²⁾, simulations of GNSS availability for location estimation³⁾, and map matching of pedestrian trajectories using GPS and PDR⁴⁾ have been conducted, but there is still a lack of knowledge on the observation of crowd behavior in the pedestrian space and on crowd control and response in the event of a disaster.

Therefore, in this study, the target elements were classified as the direction of the crowd, walking speed, density, and spatial conditions. Psychological conditions were excluded. Mobile location data obtained from smartphones were used to gain basic knowledge about pedestrian traffic flow under crowding conditions during events.

2. Methods of analysis

2.1 Target events

The target events were Halloween in Shibuya and Luminarie in Kobe. By observing and analyzing events with different characteristics (Table 1), one can understand the characteristics of crowd behavior and differences in pedestrian traffic flow control methods.

2.2 Analysis methods and flow

The velocities and densities obtained from the field survey results and mobile location data were compared. “Crowding” was defined as a state of high density and reduced speed to understand the characteristics of pedestrian traffic flow that differ from event to event and crowding conditions under high density (Figure 1).

* Student, Master Course of Department of Urban Design and Engineering

** Associate Professor, Department of Urban Design and Engineering

Table 1. Characteristics of target events

Event	Shibuya Halloween	Kobe Luminarie
Target Location	“Shibuya Scramble Crossing ~Around Center Street”	“Motomachi Higashi Yuenchi”
Area covered	Approx.0.12 km ²	Approx.0.5 km ²
Number of mobile data acquired	12,889 units	39,445 units
Number of participants [per day]	“No organizer, unknown. (Estimated 10 to 1 million people)”	“Approx.542,000
Spatial Conditions	Streets and Intersections	Streets and Squares
Crowd movement conditions	No guidance,only Center Street is one direction in congestion	One direction with guidance

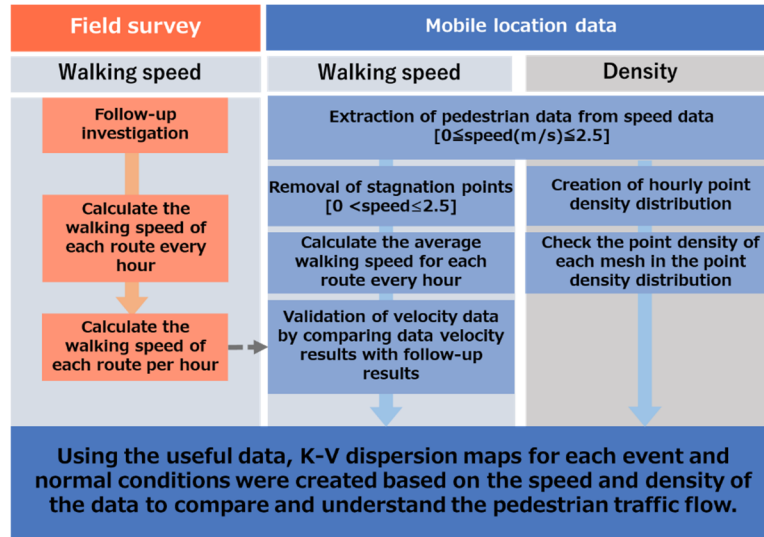


Fig. 1. Flow analysis

2.3 Outline of the field survey

A follow-up survey was conducted to understand the walking speed of people on the day of the event. In the follow-up survey, pedestrians were followed along the set course, and the speed of each route was measured every hour — five times for the Shibuya Halloween and twice for the Kobe luminarie. (Figure 2,3)

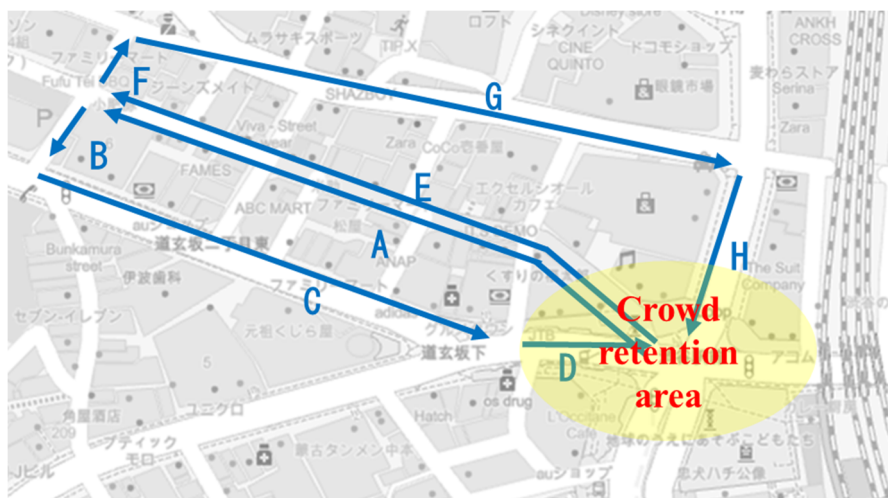


Fig. 2. Route map for Halloween in Shibuya

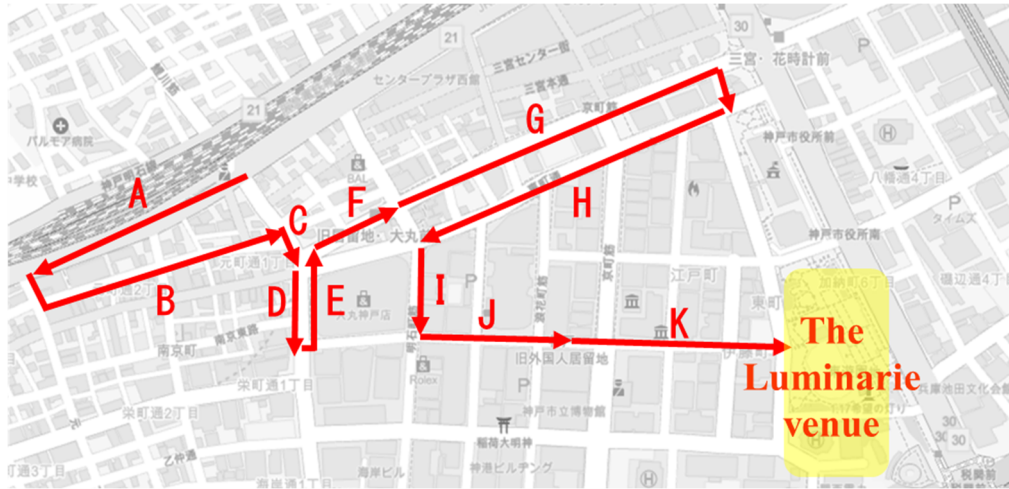


Fig. 3. Path of Kobe Luminarie

2.4 Mobile location data

The mobile location data used are the location information collected from the GPS of a smartphone with a specific app installed, with the age and gender of the user being kept secret, and provided by Agoop as point data. The information includes longitude and latitude, direction of movement, and speed.

2.4.1 Average transit speed analysis for each link path in the data

Pedestrian routes were set up for each event, and mobile location data at the time of the event were analyzed for the average hourly transit speed of each link using the Mobmap human flow analysis software.

2.4.2 Comparison of density and velocity relationships before and after the event

Using mobile location data observed on an hourly basis, point densities and velocities were aggregated hourly in 10-m meshes of the target site and compared before and after the event.

3. Results of the field survey and comparison of speed data

The results of the follow-up survey were compared with the mobile data, which were determined to be pedestrians based on the speed ($0 < \text{speed} \leq 2.5$) when passing through each route during the event. For Shibuya Halloween, the averages were similar except for route D.(Figure 4)

However, for the Kobe Luminarie, the average speed was higher for all routes in the follow-up survey results than for the data, and the average speed for Kobe Luminarie was higher than that for Shibuya Halloween. This is because the entire route of the Kobe Luminarie is unidirectional, and it is influenced by the spaciousness of the induction routes and the age range of the participants. Next, the intervals of variation were compared using Tables 2 and 3. In the Shibuya Halloween, the value of path A is small (Table 4). This may be because the movement of the crowd was unified to one way only for path A. In addition, the significant decrease in the standard deviation of path F after 7:00 p.m. was caused by the one-way flow of path A (E), which caused a backflow of participants who tried to reverse the flow of path A and a stagnation of participants who walked along path A near the start of path F.

As a result, the effect of the constant movement of the crowds was considered as a numerical value. In the Kobe Luminarie, the low values of J and K in Table 3 are considered to result from the effect of constant crowd movement at the highest density near the event destination. The results in Tables 2 and 3 show that the data had a large variation, even when crowd movements were unified, as in Kobe Luminarie.

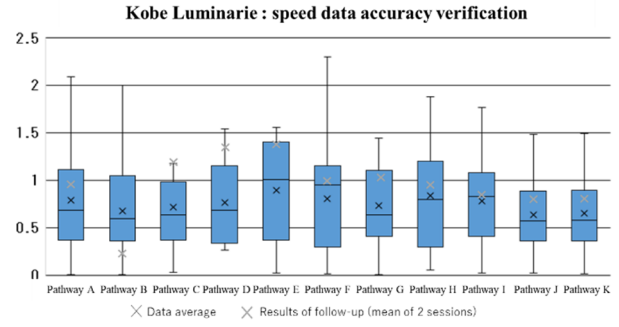
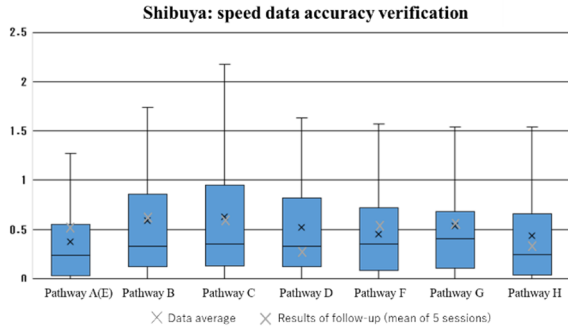


Fig. 4. Speed verification results for each link path at each event

Table 2. Standard deviation of Shibuya Halloween speed data by time and route

Standard deviation	Pathway A(E)	Pathway B	Pathway C	Pathway D	Pathway F	Pathway G	Pathway H
5:00 p.m.	0.476	0.819	0.697	0.452	1.105	0.793	0.808
6:00 p.m.	0.428	1.098	0.585	0.592	0.702	0.577	0.486
7:00 p.m.	0.363	0.443	0.55	0.528	0.183	0.565	0.454
8:00 p.m.	0.422	0.473	0.594	0.501	0.059	0.588	0.34
9:00 p.m.	0.269	0.136	0.729	0.684	0.059	0.494	0.649
10:00 p.m.	0.5	0.938	0.737	0.416	0.006	0.552	0.458
11:00 p.m.	0.329	0.479	0.372	0.215	0.331	0.496	0.405
Mean standard deviation	0.398	0.627	0.609	0.49	0.35	0.581	0.514

Table 3. Standard deviation of speed data by time and route in Kobe Luminarie

Standard deviation	Pathway A	Pathway B	Pathway C	Pathway D	Pathway E	Pathway F	Pathway G	Pathway H	Pathway I	Pathway J	Pathway K
6:00 p.m.	0.554	0.377	0.454	0.773	0.601	0.471	0.331	0.332	0.354	0.462	0.325
7:00 p.m.	0.472	0.334	0.404	0.447	0.469	0.588	0.426	0.545	0.387	0.299	0.282
8:00 p.m.	0.478	0.512	0.458			0.469	0.428	0.458	0.557	0.439	0.479
9:00 p.m.	0.557	0.454	0.679			0.371	0.211	0.412	0.465	0.402	0.387
Mean standard deviation	0.515	0.419	0.498	0.61	0.535	0.475	0.349	0.437	0.441	0.4	0.368

4. Comparison of pedestrian traffic flow analysis and K - V scatter plots for each event

The K - V scatter plots were used to compare the normal data and the data at the target event by event. In Kobe, the dots with $K > 3.0$ in Fig. 5 are the highest density symbols in Fig. 7, i.e., people in the luminary venue. Figure 7 shows the result of extracting the points with $K \leq 0.5$ and $V \leq 0.5$, as shown in Fig. 5. Because most of the points in Fig. 5 are not on the induction path, these points are mostly nonparticipants, while the points on the K - V line are mostly on the induction path and are considered to be points of the event participants.

Thus, it was possible to capture the strict division of event participants and nonparticipants by security on the K - V scatter diagram.

In the Shibuya area, points with $K \leq 1.5$ and $V \leq 0.5$ were extracted, and the above points were sparsely distributed throughout the entire area except for the high-density area (Fig. 6,8). In the normal case, the points $0 \leq K \leq 0.5$ and $0.5 \leq V \leq 2.5$ on the scatterplot flowed around the $0.5 \leq K \leq 1.5$ and $V \leq 0.5$ area. Therefore, it was found that most people walking at low speed, even at low density, during the Shibuya Halloween tended to congregate at places where there were crowds of people to a certain extent.

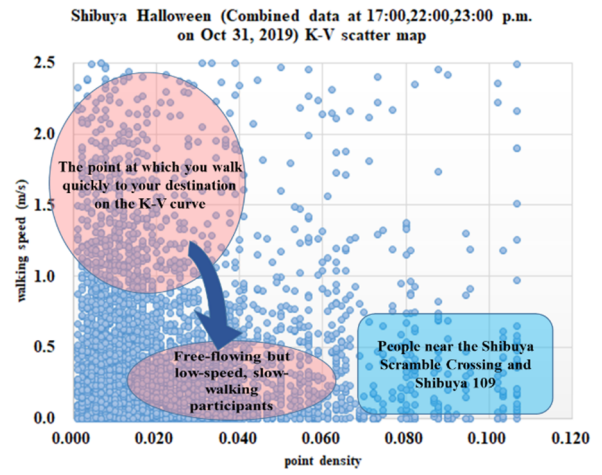
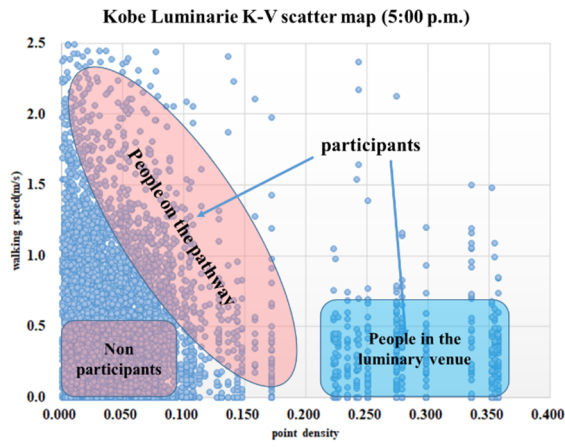


Fig. 5. Kobe Luminarie K - V scatter map

Fig. 6. Shibuya Halloween K - V scatter map ($K \leq 3$)



Fig. 7. Point extraction for Kobe Luminarie ($K \leq 0.5$ and $V \leq 0.5$)

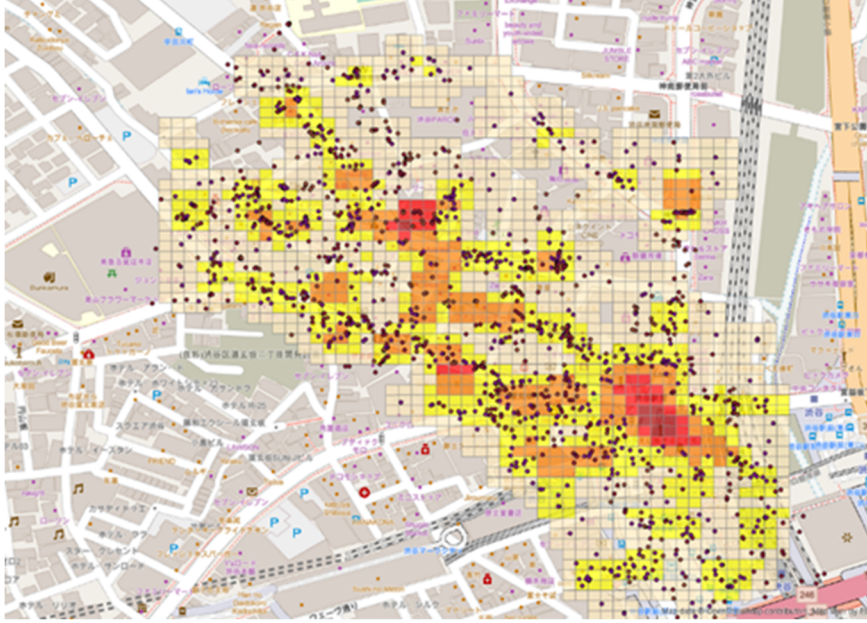


Fig. 8. Point extraction for Shibuya Halloween ($K \leq 1.5$ and $V \leq 0.5$)

5. Conclusions

The variability of the speed data was found to be relatively small when the movement of the crowd was unified or when retention was occurring. On the other hand, the variability of speed data in the whole data made us feel the limitation of the current accuracy. By creating the K - V scatter diagram, we found that many people walked at a lower speed at Shibuya Halloween than in normal times, and that people tended to gather at places with a certain amount of crowds. In Kobe Luminarie, the participants and non-participants were strictly separated by security. Thus, it was confirmed that it was possible to roughly understand the pedestrian traffic flow during the event.

In this study, we were able to capture the overall movement of people at the time of the event in an aggregate manner from the entire data, such as the variability of the entire data and the K - V scatter diagram, but we were not able to grasp the movement of each individual in detail. In the future, we would like to seek a method of analyzing pedestrian behavior and crowd behavior from mobile location data to better understand pedestrian traffic flow during events and disasters, and to gain new knowledge on how to control it.

6. References

- 1) T. Sato and T. Maruyama: Spatio-temporal analysis of smartphone-type migration survey data using kernel density estimation method, *Journal of Urban Planning*, Vol. 51 (2016)
- 2) M. Kajiji and A. Kitago: Study on crowd wave phenomenon under high-density crowd congestion leading to pedestrian accidents, *Proceedings of the Japan Society for Community Safety*, No.17 (2012)
- 3) S. Kamijo: Possibility of GNSS based Self-localization in Urban Canyon for Automated Vehicles, *ICCVE 2014 Summit Session S3*, November 4 2014, Vienna (2014)
- 4) Dailin Li and Yanlei Gu, S. Kamijo: Smartphone Based Lifelog with Meaningful Place Detection, *2018 IEEE International Conference on Consumer Electronics (ICCE)*, Las Vegas (2018)

Abstracts of Papers

Published in Other Journals

Mechanical Engineering

Color of Cooked Rice to Improve Appetite for Elderly

Pantakan SUKONTEE, Chanprapha PHUANGSUWAN, Hiroyuki IYOTA, Hideki SAKAI and Mitsuo IKEDA

Proc. of the 5th Asia Color Association Conference, Nagoya, Japan, Nov.29 - Dec.2, pp.39-43 (2019).

In the next few years, we will step into the aging society completely and many changes will take place with aging. The most common problem in the elderly is anorexia, they get bored to eat any foods. To improve this situation we hypothesized that if we change the color of rice changes from white to some other color by herbs such as butterfly pea, yellow by turmeric, red by roselle, green by pandanus leaf. Four chromatic colors and plus white rice were prepared to be presented by LCD display. In each of color rice, we changed the saturation by using Adobe Photoshop from the original color that was measured directly from real rice. Three steps of higher saturation were added to the original color and three steps of lower saturation were added to the original color. Finally, the total stimuli were 25 pictures. The preference questionnaire was “like” and “dislike” with scale 3 to -3, meaning like or dislike. We found that Thai elderlies preferred no vivid color of rice in red, yellow, green and blue. Japanese elderlies mostly preferred white color of rice and showed a small preference for red and yellow color by the reason that Japanese are familiar with the red and yellow rice for their daily life.

Device Independent Simultaneous Lightness Contrast

Saran CHANTRA, Mitsuo IKEDA, Hideki SAKAI, Hiroyuki IYOTA and Chanprapha PHUANGSUWAN

Proc. of the 5th Asia Color Association Conference, Nagoya, Japan, Nov.29 - Dec.2 pp.181-185 (2019).

The simultaneous lightness contrast phenomenon was investigated with four different devices; a paper stimulus, a two - rooms arrangement, a display, and a projector. Luminances of the central gray patch and surround were made equal among the devices. Except the paper stimulus the strength of SLC was about same among other devices to imply device independent SLC.

Measurement of Wet Colors of Bricks and Gravels by Using A Non-Contact Colorimetric System with Dome Illumination

Mai ISOMI, Hideki SAKAI, Tsugumichi WATANABE and Hiroyuki IYOTA

Proc. of the 5th Asia Color Association Conference, Nagoya, Japan, Nov.29 - Dec.2, pp.426-431 (2019).

We measured the color changes of some garden components such as bricks and gravels from completely wet to completely dry. Various colored bricks and gravels are sometimes used to decorate gardens. They easily change color when they become wet. Therefore, it is helpful to know their wet colors for designing garden scenery on a rainy day. In this experiment, beige, red and brown bricks were prepared, and white, red and green gravels were prepared. We immersed them under water for 30 minutes (completely wet condition). Then, we took them from water, and measured their color changes when drying at various intervals. To measure the colors, a non-contact colorimetric system with dome illumination was used. It consists of a hemispherical dome illumination and movable light traps. The dome illumination makes it possible to obtain the unshaded images of rough surfaces of bricks and gravels. Without a light trap, however, the unshaded images are specular component included (SCI). With a light trap in one position, a part of the image becomes specular component excluded (SCE). When the light trap is moved to another position, another part of the image becomes SCE. Then, after moving the light traps all over the inner surface of the dome, all parts of the SCE image are obtained and can be merged into a complete SCE image.

Evaluation Automatization of 2D-Image Recording System for Analysis of Change in Food Appearance using Dome Illumination with Digital Camera

Aya HIROUCHI, Hiroyuki IYOTA, Mai ISOMI, Hiroyuki YAMAMOTO and Hideki SAKAI

Proc. of the 5th Asia Color Association Conference, Nagoya, Japan, Nov.29 - Dec.2, pp.462-465 (2019).

The appearance of food, including its surface color and glossiness, is an important factor in the evaluation of quality. In general, the parameters associated with appearance change with time due to water evaporation and the chemical reactions that occur during thermal processing, drying, storing, and mundane exposure. To evaluate these parameters, quality control of food and process optimization is necessary. There are several

available instruments for the measurement of the color and glossiness of flat and dry material surfaces. However, these tools are not suitable for the characterization of the appearance of food due to the combined effects of the roughness and moisture of food surfaces. Therefore, we have developed a device for the contactless measurement of color and glossiness using a digital camera and a dome-shaped illumination device. This instrument facilitates the acquisition of color images via specular component included (SCI) and excluded (SCE) modes for subsequent analysis with/without the shading of a region of the dome-shaped illumination. In this investigation, we installed an automatic control system for the illumination device to capture the SCE and SCI images for long-duration monitoring. Electrical components were also installed to measure the temperature, humidity, and weight of food. The developed instrument facilitates the acquisition of images without the requirement of a human operator, while analyses of the color and glossiness change with time. Important experimental data can be obtained using this system, such as the effect of food appearance change on the process conditions.

Model Description on the Interface Deformation after the Release of the Pinned Contact Line

Takahiro ITO (Chubu Univ.), Souichiro FUJII (Nagoya Univ.), Tatsuya TSUNEYOSHI (Nagoya Univ.), Yoshiyuki TSUJI (Nagoya Univ.), Kenji KATOH and Tatsuro WAKIMOTO
Japanese Journal of Multiphase Flow, Vol. 34, No. 1, pp. 231-242 (2020) (in Japanese).

Contact line can be easily stuck (pinned) on the defects or boundary of the different wettability regions. The contact line remains to be trapped until the contact angle increases beyond the advancing angle or decreases below the receding angle. Once such condition is satisfied, the contact line is released from the trapping site and rapidly proceeds or recedes with the contact angle changing toward the equilibrium contact angle. In this study theoretical description on the contact line motion and the contact angle after the release from the stuck condition at the groove edge is developed. The normal stress balance and the corresponding flow field adjacent to the surface are expressed under Stokes approximation. Since the interface deformation was limited within a certain distance from the solid surface, referred as 'boundary layer', the equation on the normal stress balance equation was solved with the boundary condition at the contact line and the outer boundary of the boundary layer. The results numerically obtained were compared with the experimental data, showing fairly good agreement between them.

Removal of Micrometer-Sized Particles on a Solid Wall by High-Speed Impinging Air Jet

Tatsuro WAKIMOTO, Akihiro TAKAHASHI, Kazuhiko SOEMOTO (Shinko Co. Ltd.) and Kenji KATOH
Advanced Experimental Mechanics, Vol. 5, pp. 57-62 (2020).

In this study, a cleaning device to remove micron-sized particles on a solid surface by an air jet is developed. This device has a special nozzle containing a triangular cavity to add high intensity turbulence to the air jet, and the air jet impinges on the solid surface removing the particles. Assuming the removal of a spherical particle by rotational movement, we performed numerical simulation of the flow field in the cleaning device and estimated the rotational moment induced by drag force from the numerical results. As the results of the numerical analysis for modified nozzle shapes, it was clarified that the minimization of slit length reduced pressure loss in the slit and increased the velocity of near-wall flow. This effect enhanced the removal moment and improved removal performance.

Measuring Method of Surface Tension of Liquid

Tatsuro WAKIMOTO and Kenji KATOH

Journal of the Japanese Society for Experimental Mechanics, Vol. 20, No. 2, pp. 139-141 (2020) (in Japanese).

In order to measure the surface tension with enough accuracy and reproducibility, experimenter must be versed in the measuring method and be careful in preparing and storing the test liquids. In this paper, we explain typical four measurement methods of surface tension: capillary-rise method, Wilhelmy method, sessile drop method, and pendant drop method. Although legacy capillary-rise method is quite simple, accuracy is not enough. Wilhelmy method is the most popular and well-balanced technique between moderate accuracy of ± 0.2 mN/m and operator's effort. Sessile and pendant drop methods are capable of high-accuracy measurement below 0.1 mN/m in return for precise image data processing. Technical know-how and cost reduction of these methods are also described in this paper.

Movement Control of Falling Droplet on a Plate using Micro-Wrinkle

Kenji KATOH, Eriko SATO, Shin'ya YOSHIOKA (Osaka Electro-Communication University) and Tatsuro WAKIMOTO

Chemical Industry, Vol. 71, No. 9, pp. 562-566 (2020) (in Japanese).

In this study, we consider the control of a liquid droplet movement rolling down on an inclined plate with gravitational force using a micro-wrinkle on a wall. The micro-wrinkle was manufactured by the buckling of a thin polymer film (poly(N-vinylcarbazole), PVK) on a base polymer (poly(vinyl chloride), PVC). The PVC was stretched once and then PVK (~ 100-nm thickness) was spin-coated on the surface of the base polymer at ambient temperature. When the strain was released in a thermostatic chamber heated above the glass transition temperature of PVC, a two-dimensional micro-wrinkle having a wavelength of several micrometers was formed on the surface. The advancing and receding contact angles were measured in directions parallel and perpendicular to the wrinkle. It was observed that there were several degrees of contact angle anisotropy. When the droplet was set on the wrinkle surface inclined at 45° to the gravitational force, the direction of droplet movement could be changed by ~20° from the gravitational direction. The deflection angle was estimated from a theoretical model with the principle of minimum work of the contact line.

Development of an Archery Robot for the Selection of Arrows

Masashi OHARA, Naoki KAWASAKI, Jun NAKAHAMA, Yogo TAKADA and Hitoshi WATANABE

Proc. the 13th Conference of the International Sports Engineering Association, Online, June 22-26, 49, 115, 7 pages (2020).

The appropriate selection of arrows in the sport of archery is important to the achievement of high-quality results. In this regard, a shooting machine that is compatible with the wide variety of available bows and arrows is necessary. However, bow strength and arrow length vary among different athletes. It is also important to develop a shooting machine that reproduces the movement of the right fingers that releases an arrow, and the forward jump of a bow after shooting an arrow. In this study, a shooting machine was developed that considered these factors. Its efficacy was examined in terms of its ability to determine the characteristics of each arrow, and to distinguish between normal and flawed arrows. Based on the experimental results, we identified the factors that affected the shooting accuracy of arrows. In addition, the developed shooting machine was able to distinguish between normal and flawed arrows.

Temperature Dependence of the Growth Process of Grain Boundary Steps Formed on Ultra-precision Finished Polycrystalline Copper Surface

Tatsuya USUKI and Hiroshi KAWAKAMI

Journal of Japan Institute of Copper, 59(1), pp. 304-308 (2020) (in Japanese).

Ultra-precision cutting has its own problems that are not taken into the consideration in ordinary cutting. One of such problems is grain boundary step (GBS) formation. The GBS is a step forming along a grain boundary on ultra-precision finished surface of polycrystalline metals. The height of GBS can be higher than that of cutting marks, resulting in reducing the quality of the finished surface. Although grain boundary sliding is considered as the origin of GBS formation, the growth mechanism of GBSs is still not clear. In the studies of grain boundary sliding in creep phenomenon, the apparent activation energy was calculated from the temperature dependence of creep strain rate, and the mechanism of grain boundary sliding was proposed based on the calculated activation energy. The apparent activation energy will be effective measure to study the growth mechanism of GBSs. In this study, in order to calculate the apparent activation energy of GBS growth process, the change in the height of GBS at -30 °C, 25 °C, 60 °C and 90 °C was measured. The height of GBS saturated in shorter time at higher temperature. The height increasing with time was higher at higher temperature. The value of the apparent activation energy was about 20 kJ/mol, which was significantly smaller than the apparent activation energy of the grain boundary diffusion (104 kJ/mol). Such difference in the apparent activation energy indicates that the growth of grain boundary steps on ultra-precision finished surface originates from mechanisms different from the grain boundary diffusion.

Estimation of R-curve for Mode II Interlaminar Fracture Toughness from Tensile Strength of CFRP Laminates with Fiber Discontinuities

Hayato NAKATANI, Takaaki WAWABINO and Katsuhiko OSAKA

Proc. of the 1st Russia-Japan Joint Workshop on Composite Materials, Moscow, Russia, Oct.31 - Nov.1, 2 pages (2019).

Tensile tests for unidirectional CFRP laminates that contain three spots of fibre discontinuities dispersed at an arbitrary interval are carried out. Relations between the interval and the obtained shear strength, which is the fracture load divided by surface area created by interlaminar crack originated from fibre discontinuities, has revealed that the fracture of the laminates is dominated by interlaminar fracture toughness of this

material. Energy release rates at crack tips from different spots of fibre discontinuities are qualitatively evaluated by finite element analysis with virtual crack closure technique. A crack from thicker fibre discontinuous spot has been found to exhibit higher energy release rate at its tip. The experimentally obtained fracture stresses are converted into critical energy release rates (CERR) in mode II by applying an analytical model that calculates changes in strain energy before and after crack growth from the fibre discontinuity. As a result, relations between the fracture stress and the interval are converted into that between CERR in mode II and crack extension. The trend of CERR plots agrees well with the R-curve obtained by ENF tests.

Dependence of Vickers Hardness on Layer Thickness in Electrodeposited Ni-Co-Cu/Cu Multilayered Films

Hiroyuki HAGIWARA, Naofumi KAWAKAMI, Yoshihisa KANEKO and Makoto UCHIDA

Materials Transactions, 60(12), pp.2569-2575, (2019).

The layer thickness dependence of Vickers hardness was investigated in Ni-Co-Cu/Cu multilayered films having layer thicknesses h ranging from 10 nm to 300 nm. The Ni-Co-Cu/Cu multilayered films were fabricated by electrodeposition. In the layer thickness range of $h \geq 75$ nm, the hardness increased with decreasing layer thickness. Conversely, the hardness decreased with decreasing layer thickness at $h \leq 75$ nm. At $h = 10$ nm, the hardness decreased to 97 HV, although the local maximum at $h = 75$ nm was 210 HV. In the X-ray diffraction (XRD) profiles around the fcc (111) peak, the 10 nm multilayered film revealed a single peak, while two peaks corresponding to the Ni-Co-Cu and Cu layers were detected in the other multilayered films. The low hardness of the 10 nm film can be understood from the absence of interface strengthening, which was deduced from the single XRD peak. For $20 \text{ nm} \leq h \leq 75 \text{ nm}$, the two (111) peaks approached each other. The decreased hardness in this region could be related to sparse misfit dislocations, which can be estimated from the XRD peak angles.

Fabrication and Enhanced Vickers Hardness of Electrodeposited Co-Cu Alloy Film with High Composition Gradient

Hiroyuki HAGIWARA, Yoshihisa KANEKO and Makoto UCHIDA

Materials Transactions, 61(4), pp.801-804, (2020).

By applying an oscillating potential wave, we obtained an electrodeposited Co-Cu alloy film in which the Co concentration changed periodically at a short modulation wave length. A triangular Co concentration modulation was observed along the film growth direction. The local composition gradient became as high as 50 at%/μm. The Vickers hardness of the composition gradient film was 380 HV. Because this value was much higher than that of simple electrodeposited Co-Cu alloy films, contribution of the composition-gradient structure to hardness was suggested.

Sliding-Wear Properties of Electro-Deposited Films with Cu and Pulse-Plated Ni Multi-Layers

Hiroyuki HAGIWARA, Kohei NAKAMURA, Yoshihisa KANEKO and Makoto UCHIDA

Materials Transactions, 61(6), pp.1102-1108, (2020).

The purpose of the present study is to investigate the effect of component layer geometry on wear resistance in multilayered structures consisting of soft Cu layers and hard nanocrystalline Ni layers, which were fabricated by electrodeposition. Pulsed-potentials were applied only during the nickel layer deposition to obtain the nanocrystalline Ni microstructure. We prepared the multilayers with various component layer thicknesses and various ratios of the Ni to Cu layer thicknesses. Pulse-plated nickel films without Cu layers were also prepared for comparison. The formation of nanostructured grains was recognized in the pulse-plated nickel using transmission electron microscopy (TEM). Among the multilayered films prepared in this study, the multilayer with the nanocrystalline nickel layers of 190 nm thickness and the Cu layer of 10 nm thickness revealed the best wear resistance. The weight-loss rate and the worn depth of this multilayered film were approximately half of those measured in the nanocrystalline nickel film without the Cu layers at the vertical loads of 10 N and 20 N. These results suggest that the periodic insertion of thin Cu layers can improve the wear property of nanocrystalline nickel film.

Effect of Heating Condition on Bonding Strength of Hot-Air Welding of Stainless Steel and PA Plates

Hiroaki KOBAYASHI, Makoto UCHIDA, Hoichi KITANO and Yoshihisa KANEKO

Journal of the Society of Materials Science, Japan, 68(11), pp. 833-838, (2019).

Welding of metal and polymer is attracting example of a joining technique of different materials. However, it is expected that mechanical behavior of the polymer changes markedly due to heating exceeding the melting

point and residual stress. Plates of polyamide and SUS304 were welded using the hot-air welding machine under different welding conditions. The influence of heating time, distance and cooling conditions on the bonding strength of the welded structure were evaluated by tensile test. The obtained results demonstrated that the bonding strength in some specimens became larger than yielding strength of PA depending on the welding condition. However, the tensile responses considerably varied even for specimens obtained from same welding condition. The situation of fracture was classified in three cases, namely, fracture of interface, fracture of polymer, and fracture of welding area. The first and third cases were observed when the total heat given to the polymer were large and small, respectively. The strain distribution around the welding area under small deformation could be a indicator of predicting the fracture pattern of the welded specimen.

Numerical Analyses of Non-Uniform Deformation during Plane Strain Compression of Polycrystalline Material Using Second-Order Homogenization Method

Masashi SAKAMOTO, Takayuki OTSUKA and Makoto UCHIDA

Journal of the Society of Materials Science, Japan, 68(11), pp. 839-844, (2019).

A second-order homogenization method, in which strain gradient in macroscopic region is considered, has been proposed to evaluate the size effect on the macroscopic deformation. In this study, plane strain compression of a polycrystalline material is numerically investigated using an FE-based second-order homogenization method, and effects of size of macrostructure and friction on macroscopic non-uniform deformation is discussed. In the simulation of plane strain compression, the friction between an anvil and a specimen causes non-uniform deformation on the macroscopic region and the size of the specimen affects the compressive force and the macroscopic distribution of strain when the friction force works. The results find that under deformation with the strain gradient caused by the friction the compressive force becomes larger and the macroscopic distribution of strain becomes more inhomogeneous as the size of the specimen becomes larger. These size effects on the macroscopic region are related to deformation in microstructure that depends on the strain gradient in the macrostructure.

Effect of Metal Type and Heating Condition on Joint Strength of Metal and Polymer Prepared by Arc Welding

Hiroaki KOBAYASHI, Makoto UCHIDA, Hoichi KITANO and Yosihisa KANEKO

Quarterly Journal of the Japan Welding Society, 38(2), pp.1s-5s, (2020).

Welding is an important joining technology for dissimilar materials, such as metals and polymers. However, the joint strength of the welded structure and the mechanical behavior of the polymer change significantly owing to the thermal history of the polymer during the welding process. In this study, polyamide6 (PA6) plates were welded to stainless steel (SUS304) and aluminum (A5052) plates using arc welding at different welding conditions. The effects of the welding conditions and metal type on the joint strength were investigated using the tensile tests. The experimental results demonstrated that the joint strength of the welded structure strongly depended on the thermal history of PA6. When the temperature of the metal plate exceeded the melting temperature of PA6, the joint strength increased. However, the joint strength decreased considerably when the temperature exceeded the thermal decomposition temperature of PA6. The fracture of PA6 was classified into two categories depending on the amount of heat applied to PA6, namely, fracture of interface and fracture of polymer.

Applied Physics and Electronics

Characteristics of Multi-photon Absorption in a β -Ga₂O₃ Single Crystal

Suguru YAMAOKA, Yusuke MIKUNI, and Masaaki NAKAYAMA

Journal of the Physical Society of Japan Vol.88, 113701 (3 pages) (2019)

We have investigated the characteristics of multi-photon absorption (MPA) in a β -Ga₂O₃ single crystal at room temperature using the photoluminescence (PL) of the self-trapped exciton (STE) as a probe. From analysis of the excitation fluence dependence of the integrated STE-PL intensities at various excitation photon energies, we clearly confirmed the occurrence of two-, three-, four-, and five-photon absorption processes. The optical transition energies in the four- and five-photon absorption processes are almost consistent with the transition energies between lower-lying valence bands and the conduction-band bottom at the Γ point and those at critical points away from the Γ point, which are taken from previously reported first-principles calculations, respectively.

DOI: 10.7566/JPSJ.88.113701

Terahertz Electromagnetic Waves Radiated from Coherent Longitudinal Optical (LO) Phonons and LO-Phonon Plasmon Coupled Modes in (001)-, (110)-, and (111)-oriented Semi-insulating GaAs Single Crystals

Hideo TAKEUCHI, Takuya NISHIMURA, and Masaaki NAKAYAMA

Semiconductor Science and Technology Vol.35, 065007 (6 pages) (2020)

We report on terahertz electromagnetic waves from coherent longitudinal optical (LO) phonons and coherent LO-phonon plasmon coupled (LOPC) modes in (001)-, (110)-, and (111)-oriented semi-insulating GaAs single crystals. The coherent LO phonons and coherent LOPC modes are observed in the three samples. In contrast, coherent transverse optical (TO) phonons are not observed in the (110)- and (111)-oriented samples in spite of that the TO phonon is the Raman active mode. We conclude that only the coherent longitudinal oscillating polarization such as coherent LO phonons and coherent LOPC modes radiate the terahertz wave and that the Raman selection rule does not contribute to the terahertz-wave-radiation process. The photogenerated electron-density dependence of the frequencies of the coherent LOPC mode is almost the same in the three samples. This finding indicates that the coupling of the LO phonon with the plasmon is not influenced by the surface orientations of the three samples.

DOI: 10.1088/1361-6641/ab7d4a

Controlling the Dimension of the Quantum Resonance in CdTe Quantum Dot Superlattices Fabricated via Layer-by-Layer Assembly

TaeGi LEE, Kazushi ENOMOTO, Kazuma OHSHIRO, Daishi INOUE, Tomoka KIKITSU, Hyeon-Deuk KIM, Yong-Jin PU, and DaeGwi KIM

Nature Commun. Vol. 11, pp. 5471-1-5471-10 (2020)

In quantum dot superlattices, wherein quantum dots are periodically arranged, electronic states between adjacent quantum dots are coupled by quantum resonance, which arises from the short-range electronic coupling of wave functions, and thus the formation of minibands is expected. Quantum dot superlattices have the potential to be key materials for new optoelectronic devices, such as highly efficient solar cells and photodetectors. Herein, we report the fabrication of CdTe quantum dot superlattices via the layer-by-layer assembly of positively charged polyelectrolytes and negatively charged CdTe quantum dots. We can thus control the dimension of the quantum resonance by independently changing the distances between quantum dots in the stacking (out-of-plane) and in-plane directions. Furthermore, we experimentally verify the miniband formation by measuring the excitation energy dependence of the photoluminescence spectra and detection energy dependence of the photoluminescence excitation spectra.

<https://doi.org/10.1038/s41467-020-19337-0>

Temperature Effects on the Formation and the Relaxation Dynamics of Metal-Organic Interface States

Klaus STALLBERG, Masahiro SHIBUTA, and Ulrich HÖFER

Phys. Rev. B Vol. 102, pp. 121401-1-121401-5 (2020)

Using time-resolved two-photon photoemission, we systematically study temperature effects on the Shockley-derived unoccupied interface states of perylene- and naphthalene-tetracarboxylic dianhydride (PTCDA and NTCDA) adsorbed on Ag(111). With increasing sample temperatures from 100 to 300 K, we observe a continu-

ous decrease of the interface-state energy by 0.06 and 0.1 eV, respectively, for the two different molecule/metal systems. We relate this energy shift to a molecular lifting off the metal surface. The lifting is accompanied with an increase of the interface-state lifetime from 28 to 53 fs for PTCDA and from 60 to 110 fs for NTCDA. This is in qualitative agreement with the reduction of phase space for electron scattering associated with the thermal energy shift. The magnitude of the experimentally observed lifetime increase, however, is much stronger than would be expected from the energy shift alone.

DOI: 10.1103/PhysRevB.102.121401

Spectroscopic Ellipsometry of Monolayered CdS Nanoparticles Assembled by Layer-by-Layer Method

YongGu SHIM, Atsushi KITANO, I Kazuki WAKITA, and DaeGwi KIM

J. Appl. Phys. Vol. 128, pp. 075303-1-075303-7 (2020)

Semiconductor nanoparticles (NPs) are attractive for use as the constituent blocks of artificial solids. Furthermore, the layer-by-layer (LbL) method allows one to accurately arrange and stack NPs and is being explored widely for the fundamental research and development of artificial solids and devices based on NPs. In this study, we determined the absolute values of the dielectric function of monolayered semiconductor NPs deposited by the LbL method. The aim was to measure the structural parameters, such as the thickness, NP volume density, and NP number density, of the monolayered films composed of NPs. A novel fully optical method based on spectroscopic ellipsometry was used to evaluate thin films composed of monolayered CdS NPs deposited by the LbL method. We could successfully determine the absolute values of the dielectric function of the CdS NPs deposited as monolayered films based on the above-listed parameters with accuracy. Thus, the optical constants of monolayered semiconductor NPs as well as their structural information could be obtained successfully using the proposed method, which is highly suited for nondestructively determining the parameters of thin films, including those of semiconductor NPs.

doi: 10.1063/5.0007740

Coupled Electronic States in CdTe Quantum Dot Assemblies Fabricated by Utilizing Chemical Bonding Between Ligands

Yong-Shin LEE, Tatsuya ITO, Kunio SHIMURA, Taichi WATANABE, Hang-Beom BU, Hyeon-Deuk KIM, and DaeGwi KIM

Nanoscale Vol. 12, pp. 7124–7133 (2020)

Semiconductor quantum dot superlattices (QDSLs) have attracted much attention as key materials for realizing new optoelectronic devices such as solar cells with high conversion efficiency and thermoelectric elements with high electrical conductivity. To improve the charge transport properties in the QDSL-based optoelectronic devices, it is important for the QD structures to form minibands, which are the coupled electronic states between QDs. A shorter inter-QD distance and a periodic arrangement of QDs are the essential conditions for the formation of minibands. In this study, we use CdTe QDs capped with short ligands of *N*-acetyl-*L*-cysteine (NAC) to fabricate a three-dimensional QD assemblies by utilizing the chemical bonding between NACs. The absorption spectra clearly display the quantum resonance phenomenon originating from the coupling of the wave functions between the adjacent QDs in the CdTe QD assemblies. Furthermore, we demonstrate the formation of minibands in the CdTe QD assemblies by examining both, the excitation energy dependence of the photoluminescence (PL) spectra and the detection energy dependence of the PL excitation spectra. The fabrication method of QD assemblies utilizing the chemical bonding between NACs can be applied to all QDs capped with NAC as a ligand.

DOI: 10.1039/d0nr00194e

Photoluminescence ON/OFF Switching of CdSe/ZnS Core/Shell Quantum Dots Coated with Diarylethene Ligands

Yuya SETO, Rie YAMADA, Daichi KITAGAWA, DaeGwi KIM, and Seiya KOBATAKE

Chem. Lett. Vol. 48, pp. 1394–1397 (2019)

CdSe/ZnS core-shell quantum dots coated with diarylethene ligands were successfully synthesized, and the photoluminescence ON/OFF switching behavior of the quantum dots accompanying the photochromic reactions of the diarylethene was investigated. The quantum dots exhibited a fast photoluminescence ON/OFF switching even in the low photocyclization conversion ratio of the diarylethene.

doi:10.1246/cl.190634

Low-resistance semiconductor/semiconductor junctions with intermediate metal grids for III-V-on-Si multijunction solar cells

Takashi HISHIDA, Jianbo LIANG, and Naoteru SHIGEKAWA

Japanese Journal of Applied Physics, 59, SBBB04 [5 pages] (2020)

We fabricate semiconductor//metal grid/semiconductor junctions by using surface activated bonding (SAB) of heavily-doped Si and GaAs substrates to metal grids. The metal grids are self-aligned to SiO₂ layers on other Si substrates. The current–voltage characteristics of these junctions show linear properties. A low junction resistance of 1.99 mΩ/cm² is achieved for an n⁺-GaAs//metal grid/n⁺-Si junction by successively annealing the junction at 300 °C for 1 h and 400 °C for 1 min in N₂ gas ambient. This value is much smaller than an interface resistance of SABbased GaAs//ITO/Si junctions. These results demonstrate that metal grids could be useful for bonding subcells with low parasitic resistances in fabricating hybrid multijunction solar cells by SAB.

Impact of focused ion beam in the structural analysis of semiconductor interfaces fabricated by surface activated bonding

Yutaka OHNO (Univ. of Tohoku), Hideto YOSHIDA (Univ. of Osaka), Naoto KAMIUCHI (Univ. of Osaka), Ryotaro ASO (Univ. of Osaka), Seiji TAKEDA (Univ. of Osaka), Yasuo SHIMIZU (Univ. of Tohoku), Naoki EBISAWA (Univ. of Tohoku), Yasuyoshi NAGAI (Univ. of Tohoku), Jianbo LIANG, and Naoteru SHIGEKAWA

Japanese Journal of Applied Physics, 59, SBBB05 [5 pages] (2020)

We have shown that the structural and compositional properties of semiconductor interfaces fabricated by surface activated bonding (SAB) would be modified during focused ion beam (FIB) processes operated at room temperature (RT), especially for wide band-gap materials, and such a modification can be suppressed by FIB processes operated at lower temperatures. During FIB processes operated at RT, SAB-fabricated Si/Si and GaAs/GaAs interfaces are amorphized along the interfaces, even at the internal locations deeper than the penetration depth of the FIB, and the impurity distribution across the interfaces is modified. This phenomenon is presumably due to the atomic diffusion assisted by the point defects that are introduced by FIB irradiation. By using FIB processes operated at –150 °C, the FIB-induced atomic diffusion would be ignored for Si/Si interfaces. Meanwhile, the diffusion would be still effective for GaAs/GaAs interfaces, presumably due to the effects of recombination-enhanced defect motion under FIB irradiation.

Characterization of Nanoscopic Cu/Diamond Interfaces Prepared by Surface-Activated Bonding: Implications for Thermal Management

Jianbo LIANG, Yutaka OHNO (Univ. of Tohoku), Yuichiro Yamashita (National Metrology Institute of Japan, National Institute of Advanced Industrial Science and Technology), Yasuo SHIMIZU (Univ. of Tohoku), Naoki EBISAWA (Univ. of Tohoku), Seongwoo KIM (Adamant Namiki Precision Jewel. Co., Ltd.), Koyama KOJI (Adamant Namiki Precision Jewel. Co., Ltd.), Yasuyoshi NAGAI (Univ. of Tohoku), Makoto KASU (Univ. of SAGA), and Naoteru SHIGEKAWA

ACS Applied Nano Materials, 3, 2455-2462 (2020)

The microstructures of Cu/diamond interfaces prepared by surface-activated bonding at room temperature are examined by cross-sectional scanning transmission electron microscopy (STEM). A crystalline defect layer composed of Cu and diamond with a thickness of approximately 4.5 nm is formed at the as-bonded interface, which is introduced by irradiation with an Ar beam during the bonding process. No crystalline defect layer is observed at the 700 °C annealed interface, which is attributed to the recrystallization of the defect layer due to the high-temperature annealing process. Instead of the defect layer, a mating interface layer and a copper oxide layer are formed at the interface. The mating interface layer and the copper oxide layer play a role in relieving the residual stress caused by the difference between the thermal expansion coefficients of diamond and Cu. The thermal boundary resistance (TBR) of the as-bonded interface is measured to be $1.7 \pm 0.2 \times 10^{-8}$ m²·K/W by the time domain pulsed-light-heating thermoreflectance technique. These results indicate that the direct bonding of diamond and Cu is a very effective technique for improving the heat-dissipation performance of power devices.

Effects of post bonding annealing on GaAs//Si bonding interfaces and its application for sacrificial-layer-etching based multijunction solar cells

Naoteru SHIGEKAWA, Ryo KOZONO, Sanji YOON, Tomoya HARA, Jianbo LIANG, and Akira YASUI (Japan Synchrotron Radiation Research Institute (JASRI/Spring-8))

Solar Energy Materials and Solar Cells, 210, 110501 [7 pages] (2020)

By using the sacrificial layer (SL) etching, GaAs substrates are separated from III-V epi substrate//Si substrate junctions that are made by surface activated bonding (SAB) technologies. The post-bonding low-temperature

(300-°C) annealing plays an essential role in achieving a promising (~90%) bonding yield. The effects of the post-bonding annealing are investigated by hard X-ray photoemission spectroscopy and current–voltage measurements of GaAs//Si bonding interfaces. It is found that the concentration of oxygen atoms at interfaces is reduced and the resistance decreases to 1.6–2.1 mΩ/cm² by the low-temperature annealing. Aluminum fluoride complexes are not observed by X-ray photoelectron spectroscopy on the exposed surfaces of separated GaAs substrates. The roughness average of the surfaces is ≈0.25–0.30 nm. The characteristics of double junction cells fabricated on the GaAs//Si junctions prepared by the SL etching are almost the same as those of cells fabricated by dissolving GaAs substrates after bonding. These results indicate that multijunction cells could be fabricated in a process sequence compatible with reuse of GaAs substrates by combining the SL etching and SAB.

Chemical bonding at room temperature via surface activation to fabricate low-resistance GaAs/Si hetero-interfaces

Yutaka OHNO (Univ. of Tohoku), Jianbo LIANG, and Naoteru SHIGEKAWA, Hideto YOSHIDA (Univ. of Osaka), Seiji TAKEDA (Univ. of Osaka), Reina MIYAGAWA (Nagoya Institute of Technology), Yasuo SHIMIZU (Univ. of Tohoku), and, Yasuyoshi NAGAI (Univ. of Tohoku)

Applied Surface Science, 525, 146610 [5 pages] (2020)

Bonding mechanism at room temperature (RT) in GaAs/Si heterointerfaces fabricated by surface-activated bonding (SAB) is examined using cross-sectional scanning transmission electron microscopy combined with low temperature focused ion beam and time-of-flight secondary ion mass spectrometry. In the bonding process at RT, atomic intermixing at the interfaces, presumably due to the transient enhanced diffusion assisted by the point defects introduced in the surface activation process, is confirmed. The defect-assisted atomic diffusion at the interfaces, as well as the formation of atomically clean and activated surfaces, would be the key concept of SAB, by which we can create tough heterointerfaces at RT. Meanwhile, the defects on the activated surfaces would degrade the interface resistance. The degraded properties can be recovered by an appropriate annealing after the SAB processes, although the atomistic structure around the heterointerfaces would be modified during the annealing. By controlling SAB and subsequent annealing conditions, we can obtain low-resistance heterointerfaces via the optimization of the trade-off relationship between the chemical bonding strength and the electronic properties, determined by the activated surfaces before bonding.

Direct bonding of GaAs and diamond for high power device applications

Jianbo LIANG, Yuji NAKAMURA, Yutaka OHNO (Univ. of Tohoku), Yasuo SHIMIZU (Univ. of Tohoku), Tianzhuo ZHAN (Waseda Univ.), Takanobu WATABABE (Waseda Univ.), Naoto KAMIUCHI (Osaka Univ.), Yasuyoshi NAGAI (Univ. of Tohoku), Naoteru SHIGEKAWA

Extended Abstracts of Pacific Rim Meeting on Electrochemical and Solid State Science (PRiME), G01-1634 (2020)

The direct integrating of GaAs and diamond is achieved at room temperature via a surface activated bonding method. An ultrathin crystal defect layer composed of GaAs and diamond was formed at the bonding interface. The thickness of the GaAs and diamond crystal defect layers was determined to be 0.4 and 1.6 nm, respectively. After annealing at 400 °C, no changes were observed in the thickness of the crystal defect layer and the interfacial structure. The thermal characterization of the transmission line model (TLM) patterns formed on the GaAs layer bonded to diamond and sapphire substrates is demonstrated. The thermal resistance of the GaAs TLM patterns formed on the diamond and sapphire substrates was determined to be 6 and 34.9 K/W, respectively. The GaAs TLM patterns formed on the diamond showed an excellent heat dissipation property due to the high thermal conductivity of diamond.

Fabrication of Diamond/Cu Direct Bonding for Power Device Applications

Shinji KANDA, Yasuo SHIMIZU (Institute of Materials Research (IMR), Tohoku Univ.), Yutaka OHNO (Institute of Materials Research (IMR), Tohoku Univ.), Kenji SHIRASAKI ((Institute of Materials Research (IMR), Tohoku Univ.), Yasuyoshi NAGAI (Institute of Materials Research (IMR), Tohoku Univ.), Makoto KASU (Univ. of SAGA), Naoteru SHIGEKAWA, and Jianbo LIANG

Japanese Journal of Applied Physics, 59, SB3B03 [5 pages] (2020)

Direct bonding of diamond and Cu was successfully fabricated by surface activated bonding (SAB) method at room temperature. The interfacial structures of the diamond/Cu bonding interface before and after annealing at 500 and 700 °C were investigated by transmission electron microscope (TEM) and electron energy-loss spectroscopy (EELS). A 4-nm-thick transition layer was formed at the bonding interface, the transition layer thickness decreased with annealing temperature. It was found that the atomic ratio of sp² bonding in the bonding in-

interface was larger than that of the diamond separated from the bonding interface by approximately 50 nm, which indicated that the transition layer was composed of the amorphous or graphite and diamond. After annealing at 700 °C, an intermediate layer of about 2 nm thick was observed at the bonding interface. There were no nano-voids and micro-cracks observed at the interface with annealing at a temperature as high as 700 °C. These results indicated that the diamond/Cu bonding interface has high thermal stability and can withstand the temperature rise of power devices during operating.

III-V Thin-Film Solar Cells Bonded to Si substrates via Metal Grids

Takashi HISHIDA, Jianbo LIANG, and Naoteru SHIGEKAWA

Extended Abstracts of 2019 Extended Abstracts of Pacific Rim Meeting on Electrochemical and Solid State Science (PRiME), G01-1635 (2020)

III-V on Si multijunction (MJ) solar cells are promising as next-generation solar cells since they can provide high efficiency with low cost in comparison with conventional Si and III-V MJ cells. In fabricating such III-V/Si MJ cells, III-V subcells are placed on Si bottom cell by hybrid approaches such as surface-activated bonding (SAB). The bonding interfaces with lower interface resistances are strongly required so as to achieve better performance of hybrid MJ cells. It was found that the resistance across the directly-bonded III-V/Si interfaces in MJ cells was higher than the resistance in junctions made of heavily-doped substrates because of the thin heavily-doped bonding layers in actual subcell structures. It was reported that indium tin oxide (ITO) films as intermediate layers between III-V and Si subcells played a role of lowering the series resistance of MJs [1]. It was found, however, that the resistance of GaAs//ITO/Si junctions increased by annealing them [2]. Furthermore, the quantum efficiency of Si bottom cells was lowered by inserting the ITO layers because of the free carrier absorption of ITO layers.

Nanostructural Investigation on GaAs//Indium Tin Oxide/Si Junctions for III-V-on-Si Hybrid Multijunction Cells

Tomoya HARA, Jianbo LIANG, Kenji ARAKI (Toyota Technological Institute), Takefumi KAMIOKA (Toyota Technological Institute), Hassanet SODABANLU (The Univ. of Tokyo), Kentaroh WATABABE (The Univ. of Tokyo), Masakazu SUGIYAMA (The Univ. of Tokyo), and, Naoteru SHIGEKAWA

Extended Abstracts of Pacific Rim Meeting on Electrochemical and Solid State Science (PRiME), G01-1636 (2020)

Hard X-ray photoemission spectroscopy (HAXPES) measurements and transmission electron microscopy (TEM) observations are performed on GaAs thin film//Indium tin oxide (ITO)/Si junctions fabricated by surface-activated bonding and selective wet etching. Both of the Ga-O/Ga-As ratio in the Ga 2p_{3/2} HAPES core spectrum (Fig. 1(a)) and As-O/As-Ga ratio in the As 2p_{3/2} HAXPES core spectrum (Fig. 1(b)) demonstrate that the GaAs layers are oxidized after annealing at 400 °C. This observation is consistent with the formations of a ~1-nm-thick intermediate layer in the cross-sectional TEM image of the junctions after the 400 °C annealing, as is shown in Figs. 2(a) and 2(b). It is found by using in-house X-ray photoelectron spectroscopy in combination with Ar⁺ bombardment that the oxide layers are formed at GaAs//ITO bonding interfaces after annealing at 200 °C or higher temperatures. The observation of the oxide layers corresponds with the onset of resistivity increase in GaAs//ITO/Si junctions due to the annealing [1]. These results suggest that annealing brings about the reaction between GaAs and ITO layers and hence the oxidation of GaAs layers, which causes the degradation of the electrical properties of GaAs//ITO/Si junctions. A fabrication process at lower temperatures is likely to be required so as to fully exploit the advantage of ITO as intermediate layers in III-V//Si hybrid tandem solar cells with lower series resistance.

Microscopic Picture of Direct Bonding Via Surface Activation for Low-resistance Si/Wide-Gap Semiconductor Heterointerface

Yutaka OHNO (Institute of Materials Research (IMR), Tohoku Univ.), Jianbo LIANG, Naoteru SHIGEKAWA, Hideto YOSHIDA (Univ. of Osaka), Reina MIYAGAWA (Nagoya Institute of Technology), Yasuo SHIMIZU (Institute of Materials Research (IMR), Tohoku Univ.), and, Yasuyoshi NAGAI Institute of Materials Research (IMR), Tohoku Univ.)

Extended Abstracts of Pacific Rim Meeting on Electrochemical and Solid State Science (PRiME), G01-1648 (2020)

Surface-activated bonding (SAB) [1], that is a direct wafer bonding process without additional buffer layers, is a promising method to fabricate tough and steep heterointerfaces at low cost. SAB can fabricate any heterointerfaces free from dislocations and cracks, even for dissimilar materials with different crystal structures and lattice

constants, without high-temperature annealing. Recently, SAB is applied to the next-generation semiconductors such as diamond, SiC, and GaN, as well as to the basic semiconductors such as Si and GaAs, towards low-resistance semiconductor-to-semiconductor heterointerfaces free from adherent layers. Even though such bonding is successfully demonstrated, the principle of the SAB is still controversial due to the difficulty of analyzing their non-equilibrium heterostructures at an atomistic level.

Mechanism of direct bonding via surface activation to fabricate Si/GaAs heterointerfaces towards tandem solar cells

Yutaka OHNO (Institute of Materials Research (IMR), Tohoku Univ.), Jianbo LIANG, Naoteru SHIGEKAWA, Hideto YOSHIDA (Univ. of Osaka), Seiji TAKEDA (Univ. of Osaka), Reina MIYAGAWA (Nagoya Institute of Technology), Yasuo SHIMIZU (Institute of Materials Research (IMR), Tohoku Univ.), and, Yasuyoshi NAGAI Institute of Materials Research (IMR), Tohoku Univ.)

Extended Abstracts of 2020 European Materials Research Society (E-MRS) Spring Meeting, Congress & Exhibition Centre, Strasbourg, France, May 25-29, 2020

We have examined the bonding mechanism in Si/GaAs heterointerfaces towards tandem solar cells fabricated by surface-activated bonding (SAB) at room temperature (RT), by scanning transmission electron microscopy combined with focused ion beam operated at low-temperatures [1]. In the SAB process, wafer surfaces are activated by the irradiation of inert atoms in a high vacuum, and the surfaces are then bonded by the contact. In the bonding process at RT, atomic intermixing across the interfaces, due to the transient enhanced diffusion assisted by the point defects introduced in the surface activation process, forms a nanolayer having gradient composition. Spontaneous formation of the gradient nanolayer, acting as a buffer layer that can reduce the interface energy, as well as forming strong chemical bonds, would be the key concept of SAB, by which we can create tough and steep heterointerfaces of dissimilar materials at low cost. On the other hand, those point defects can degrade the electric properties such as interface resistances. The decrease of the defects would play a crucial role in fabricating electronic devices with SAB techniques. By controlling SAB conditions, we can obtain low-resistance Si/GaAs heterointerfaces via the optimization of the trade-off relationship between the chemical bonding strength and the electric properties, determined by the distribution of point defects beneath the activated surfaces.

Mechanism of surface activated bonding for low-resistance Si/diamond and Si/GaAs heterointerfaces

Yutaka OHNO (Institute of Materials Research (IMR), Tohoku Univ.), Jianbo LIANG, Naoteru SHIGEKAWA, Hideto YOSHIDA (Univ. of Osaka), Reina MIYAGAWA (Nagoya Institute of Technology), Yasuo SHIMIZU (Institute of Materials Research (IMR), Tohoku Univ.), and, Yasuyoshi NAGAI Institute of Materials Research (IMR), Tohoku Univ.)

Extended Abstracts of The 15th International Conference Beam Injection Assessment of Microstructures in Semiconductors, Saint Petersburg, Russia, July 19-24, 2020

We have examined the bonding mechanism in Si/GaAs and Si/diamond heterointerfaces fabricated by surface-activated bonding (SAB) at room temperature (RT), using high-angle annular dark-field (HAADF) and energy dispersive x-ray spectroscopy (EDX) under scanning transmission electron microscopy (STEM) combined with time-of-flight secondary ion mass spectrometry (TOF-SIMS). In the SAB process, wafer surfaces are activated at RT by the irradiation of inert atoms in a high vacuum, and the surfaces are then bonded by the contact under a pressure. In the bonding process at RT, atomic intermixing across the interfaces, due to the transient enhanced diffusion assisted by the point defects introduced in the surface activation process, forms an intermediate layer of 4-5 nm thick having gradient composition (see Fig. 1 for Si/GaAs interface). Interestingly, no structural defect, such as cracks and dislocations, is introduced at the heterointerfaces even after high-temperature annealing, presumably due to the gradient nanolayer acting as a buffer layer that can reduce the interface energy, as well as forming strong chemical bonds. Spontaneous formation of the gradient nanolayer is, therefore, the key concept of SAB, by which we can create tough and steep heterointerfaces of dissimilar materials at low cost. On the other hand, since the point defects can degrade the electronic properties such as interface resistances, the decrease of the defects would play a crucial role in fabricating electronic devices with SAB techniques. The degraded properties can be recovered by an appropriate annealing after the SAB processes, although the atomistic structure around the heterointerfaces would be modified during the annealing. By controlling SAB and subsequent annealing conditions, we can obtain low-resistance hetero-interfaces via the optimization of the trade-off relationship between the chemical bonding strength and the electronic properties, determined by the distribution of point defects beneath the activated surfaces before bonding.

Acoustic Signal Production in Ethanol by Energetic Xenon Ions

Masanori KOBAYASHI(Chiba Institute of Technology), Takashi MIYACHI(Chiba Institute of Technology), Osamu OKUDAIRA(Chiba Institute of Technology), Seiji TAKECHI, Atsuma KUROSUMI, Takefumi UNO, Maki NAKAMURA(Nagoya University), Hiromi SHIBATA(Osaka University), Nagaya OKADA(Honda Electronics Co., Ltd.), Masayuki FUJII(Famscience Co., Ltd.), Takeshi MURAKAMI(National Institutes for Quantum and Radiological Science and Technology) and Yukio UCHIHORI(National Institutes for Quantum and Radiological Science and Technology)

Jpn. J. Appl. Phys., Vol. 59, pp. 028004-1-028004-3 (2020)

Acoustic signals produced by irradiating ethanol with 400 MeV/n Xe ions were experimentally studied. The signals were detected by an array of piezoelectric PZT elements. They were categorized into two types: one was a primary product of the incident fast ions; the other was a secondary product resulting from an energy release to ethanol just before the ions stopped and subsequently diffused in ethanol. A possible mechanism of the secondary signal is discussed in association with the Bragg peak formation.

On Cold Atmospheric-pressure Plasma Jet Induced DNA Damage in Cells

Nishtha GAUR (University of Lancaster), Hirofumi KURITA (Toyohashi University of Technology), Jun-Seok OH, Saki MIYACHIKA (Toyohashi University of Technology), Masafumi ITO (Meijo University), Akira MI-ZUNO (Toyohashi University of Technology), Allison COWIN (University of South Australia), Sarah ALLIN-SON (University of Lancaster), Robert D. SHORT (University of Lancaster) and Endre J. SZILI (University of South Australia)

J. Phys. D: Appl. Phys. Vol. 54, 034203 (11 pages) (2021)

To investigate the potential role of the hydroxyl radical ($\bullet\text{OH}$) in cold atmospheric plasma (CAP) jet treatment, two fluorescence-based methodologies are utilised to measure DNA strand breaks. The first comprises a model system of a double-stranded DNA oligomer, where the respective strand ends are tagged with fluorophore and quencher molecules; and the second, a cell culture system reporting DNA strand breaks using the $\gamma\text{-H2AX}$ assay. During the various CAP jet treatments, optical emission spectroscopy is used to detect the $\bullet\text{OH}$ in the gas phase and electron spin resonance is used to detect the $\bullet\text{OH}$ in solution. The CAP jet production of the $\bullet\text{OH}$ is shown to correlate to CAP jet induced DNA damage both with the DNA model and in biological cells. Results indicate that the CAP jet induces a higher degree of DNA damage when the CAP plume is in contact with the target solution. The potential of a ‘plasma screen’ based upon a hydrogel film, as a method to remove the DNA-damaging $\bullet\text{OH}$ species from reaching skin cells, is shown to significantly reduce DNA damage whilst facilitating the delivery of hydrogen peroxide. These findings could aid in the development of CAP jet-based applications where DNA damage is the objective (e.g. in cancer treatment) and others where it is to be avoided, e.g. in open-wound treatment and dermatology.

DOI: <https://doi.org/10.1088/1361-6463/abb8ab>

Atomic Oxygen Radical-induced Intracellular Oxidization of Mould Spore Cells

Yuta TANAKA (Meijo University), Jun-Seok OH, Hiroshi HASHIZUME (Nagoya University), Takayuki OHTA (Meijo University), Masashi KATO (Meijo University), Masaru HORI (Nagoya University), and Masafumi ITO (Meijo University)

Plasma Process Polym. Vol. 17, e2000001 (8 pages) (2020)

The inactivation mechanism of mould spores using plasma-generated neutral reactive oxygen species (ROS) was investigated in this paper. Typical cell viability using a counting of colony forming unit assay indicated a major state of the spore cells. Both intracellular and extracellular damages have been investigated by a couple of well-established cell visualization techniques: confocal fluorescence emission microscopy, scanning electron microscopy, and transmission electron microscopy. It is revealed in this paper that the combination of the spore cell viability with those visualization results strongly suggested an early stage of the cell inactivation when ROS can induce intracellular lipid peroxidation through both nanometer-thick lipid cell membrane and less damaged several hundred nanometer-thick cell wall.

DOI: <https://doi.org/10.1002/ppap.202000001>

Oxidation Processes of NO for Production of Reactive Nitrogen Species in Plasma Activated Water

Kunihide TACHIBANA (Kyoto University), Jun-Seok OH and Toshihiro NAKAMURA (Kyoto University)

J. Phys. D: Appl. Phys. Vol. 53, 385202 (14 pages) (2020)

To understand the mechanisms for selective productions of NO_2^- and NO_3^- as reactive nitrogen species (RNS) in plasma activated water, we studied the oxidation reactions of NO as the primary species supposing O, O_2 , O_3 ,

OH, and H₂O₂ as possible oxidants. A coaxial-type dielectric barrier discharge reactor was employed in cascade connection to a reservoir and/or a water bubbler. First, the densities of NO and NO₂ in the gas phase were measured with gas sensors in two gas systems: N₂ admixed with water vapor and N₂ admixed with O₂, for comparison. It was found that while the density of NO in the latter case was one third of that in the former case owing to the difference in the first-step oxidation to NO₂ or HNO₂, the total yields of RNS in both cases were comparable. To investigate the oxidation pathways, admixing NO and NO₂ in the downflow of the reactor was attempted to estimate their reactions with those oxidants and accommodation behaviours on the water surface. Injecting the effluent gas from discharge plasma into solutions of O₂, O₃, and H₂O₂, and injecting O₃ into PAW, vice versa, were attempted to inspect the reactions in the liquid phase or at the gas–water interface. Based on the obtained results, it was found that, in the N₂-H₂O gas system, OH functions as the oxidant of NO to HNO₂, exclusively yielding NO₂⁻ in solution with no effective second-step oxidation to NO₃ or HNO₃. On the other hand, in the N₂-O₂ gas system, O₃ functions as the major oxidant in the successive oxidation from NO to NO₂ to NO₃, producing NO₃⁻ predominant PAW; however, the second-step oxidation in the gas phase is competing with the oxidation reactions in the liquid phase.

DOI: <https://doi.org/10.1088/1361-6463/ab91eb>

Microplasma Discharge in Deionized Water and Artificial Seawater

Akimitsu HATTA (Kochi University of Technology), Vladislav GAMALEEV (Nagoya University), Jun-Seok OH and Hiroshi FURUTA (Kochi University of Technology)

Intl. J. Plasma Environ. Sci. Technol. Vol. 13, 1 (6 pages) (2019)

Microplasma discharges in deionized water and artificial seawater were investigated using pin-to-plate electrodes with a gap of a several tens of microns. By using a pulse voltage source, microdischarge was operated in deionized water and diluted artificial seawater and compared with discharge in ambient air. To operate the microdischarge in undiluted artificial seawater, a pulse current source (impulse generator) was used to supply the breakdown voltage with sufficient current. Even in seawater with an electrical conductivity of 45 mS/cm, microplasma discharges were reproducibly ignited at applied voltages below 1 kV. In the optical emission spectrum for the microplasma in artificial seawater, the main components of Na, Mg, Ca, K, S, H, and O were observed as distinguishable isolated lines, including lines for Pd, Ag and Fe from the electrodes.

DOI: <https://doi.org/10.34343/ijpest.2019.13.01.001>

The Measurement of Yeast Status by analyzing the electrical response waveform -using the phase angles of harmonics-

Keita TAMURA, Naoto HIGASHIHARA, Daichi TANAKA, Masafumi MURAJI, Kenji TANAKA, Tatsuru SHIRAFUJI

Record of the 2019 Kansai-section Joint Convention of Institutes of Electrical Engineering, Japan, G2-10, p.51 (2019) (in Japanese)

Further Crosstalk Reduction Method with Eye-Tracking for Glasses-Free Stereoscopic Display in Both Portrait and Landscape Modes

Yukiya YAMAGUCHI, Hiroyuki NAKAMURA, Goro HAMAGISHI, Kayo YOSHIMOTO, Takuya MATSUMOTO (Kyocera Corp.), Kaoru KUSAFUKA (Kyocera Corp.), Hideya TAKAHASHI

Proc. The International Display Workshops, Sapporo, Nov. 29, Vol.26, pp.982-985 (2019).

We previously proposed the glasses-free stereoscopic display using the slanted parallax barrier with the eye-tracking system. The previously proposed system had very high image quality. If we adopted the LC panel as the active parallax barrier, it was possible to switch into two different patterns of barriers correspond to the portrait and the landscape modes. Each barrier pattern corresponding to the two modes had the same barrier pitch and slanted angle, so basically the same eye-tracking algorithm could be applied in sensing the viewing position. Moreover, by dividing the screen into multiple areas and controlling the image positions in each area according to the viewing position, it was possible to keep the stereoscopic vision even if the viewer moved in the depth direction toward the screen. However, as the moving distance from the optimum viewing distance increased, the number of subpixels observed simultaneously with both eyes increased. We call these subpixels “crosstalk subpixels.” As the number of the crosstalk subpixels increases, the effect of stereoscopic vision is reduced. Therefore, the expansion of the viewing area in the depth direction was limited. Therefore, in this paper, we propose a method to reduce the crosstalk by displaying black images on the crosstalk subpixels. By this method, the crosstalk ratio can be stably suppressed low even if the viewer moves far from the OVD in the depth direction, so the viewing area can be expanded compared to the previous proposed system. To verify the effectiveness of the proposed system, we evaluated the crosstalk ratio at each viewing distance for both portrait and landscape modes in the prototype system.

Development of vessel position estimation system based on pixelwise refocusing using light field imaging

Kayo YOSHIMOTO, Hideya TAKAHASHI, Kohei YAMAMOTO, Kenji YAMADA (Osaka University)

Proc. SPIE Advanced Biomedical and Clinical Diagnostic and Surgical Guidance Systems XVIII, San Francisco, Feb. 21, Vol.11229, 112291N CD-ROM (2020).

Venipuncture is a medical practice which is ordinarily performed in hospital. However, it is a difficult procedure as the occurrence of many failure of the puncture and sometimes medical accidents such as nerve damage and blood vessel damage are reported. This is caused by the difficulty of visually identification of the blood vessel. Although the depth information of the blood vessel is also important, the existing system in clinical practice can visualize vessels only by two dimensional images. In our previous work, we proposed a method that adds angle filtering to a refocus-based system using light field imaging to estimate the three-dimensional position of blood vessels. Angular filtering can reduce blurring of blood vessel image obtained using infrared light due to the strong scattering properties of biological tissue. By applying the refocusing technique to an image with reduced blur, it is possible to obtain enhanced cross-sectional information of a blood vessel using near-infrared light at each depth. However, in the previous study, only phantom model results were reported, and it was not possible to study practicality. In this paper, we report the results of applying and verifying the effectiveness of the proposed method to human hand.

Control method of active parallax barrier and binocular image for glasses-free stereoscopic display according to viewing position Analysis of displayable depth range for retinal projection type super multi-view 3D head-mounted display using the time division projection optical system

Hiroyuki NAKAMURA, Tomoya KITADA, Goro HAMAGISHI, Kayo YOSHIMOTO, Kaoru KUSAFUKA (Kyocera Corp.), Hideya TAKAHASHI

Proc. SPIE Advanced in Display Technologies X, San Francisco, Feb. 26, Vol.11304, 1130414 CD-ROM (2020).

In 3D displays based on parallax barriers, active parallax barriers that can change the barrier pattern according to the viewing position have been proposed to expand the viewing area. However, the production cost increases because the active barrier requires a special LC panel. Therefore, to lower the cost, we propose a glasses-free stereoscopic display using an active parallax barrier of an LC panel with the same specifications as the image LC panel. The ideal image pattern cannot be formed because the minimum control unit of the LC panel is equal to one subpixel. However, by using an image cycle pitch method (ICPM) that periodically increases the horizontal pitch of one pair of binocular images by one subpixel, we can realize the ideal relationship between the average pitch of the binocular image and the barrier pitch. In

our previous research, we could make the average pitch match to the ideal pitch on the discrete optimum viewing distances (OVDs), but we could not follow the viewing position between the discrete OVDs. In this paper, we propose the ICPM that can keep the stereoscopic vision even at any viewing position. In order to verify the effectiveness of the proposed method, we made the prototype displays and evaluated them. As a result, we showed the crosstalk ratio could be suppressed low over a very wide range by using the proposed method. Also, we confirmed we could obtain the stereoscopic vision at the viewing distance from 300 mm to 729 mm by a subjective evaluation.

Retinal image generation method for retinal projection type super multi-view 3D head-mounted display

Junya KOHNO, Kayo YOSHIMOTO, Hideya TAKAHASHI

Proc. SPIE Advanced in Display Technologies X, San Francisco, Feb. 26, Vol.11304, 1130413, CD-ROM (2020).

We have proposed the retinal projection type super multi-view head mounted display (HMD). The super multi-view method provides stereoscopic information by inducing the accommodation of the human eye by blurring the retinal image. This method uses the principle of Maxwellian view and reconstruct the blur image by overlapping projected each parallax image on the retina. However, considering only the degree of the overlap of the projected parallax images on the retina is not enough for reconstructing the real blur. In order to overcome this problem, we propose the optimal method considering not only the degree of the overlap of the parallax images projected on the retina but also the light intensity of each parallax image to reconstruct the real blur. From the evaluation experiment, we verified that the proposed method improves the reproducibility of blur compared to the method considering only the degree of superimposition of the parallax images projected on the retina. Furthermore, it was also confirmed that the prototype system can display 3D images in the depth range of human ocular accommodation from 200mm to 2000mm. The super multi-view HMD based on the proposed method can induce the accommodation of the human eye with the high reproducibility blur and provide more natural 3D images.

Expanding Tree-Based Classifiers Using Meta-Algorithm Approach: An Application for Identifying Students' Cognitive Level

Yuni YAMASARI (ITS), Supeno Mardi Susiki NUGROHO (ITS), Kayo YOSHIMOTO, Hideya TAKAHASHI, Mauridhi Hery PURNOMO (ITS)

International Journal of Innovative Computing, Information and Control, Vol.15, No.6, pp.2085-2107 (2019).

Accurate identification of student cognitive levels is a crucial problem for a teacher in deciding the appropriate method for a teaching and learning process. Nevertheless, not much research focuses on this area. Therefore, in this paper, we investigate the problem of how to improve the classification performance to discover the more suitable students' cognitive level. We expand tree-based classifiers using a meta-algorithm called "LogitBoost" in the mining process. Then, to support this meta-algorithm to work optimally, we introduce the multivariate normality test and the combination of the discretization method and k-NN on the pre-processing stage. These designed schemes are intended to find the student data normality and to specify the number of the students' cognitive levels. Also, we propose a feature selection approach: correlation- and reliefbased feature selection to eliminate unnecessary features. The experimental results show that our proposed method can enhance the classification performance in the identification process significantly.

Identifying Dominant Characteristics of Students' Cognitive Domain on Clustering-based Classification

Yuni YAMASARI (ITS), Supeno Mardi Susiki NUGROHO (ITS), Kayo YOSHIMOTO, Hideya TAKAHASHI, Mauridhi Hery PURNOMO (ITS)

International Journal of Intelligent Engineering & Systems, Vol.13, No.1, pp.167-180 (2020).

The rapid growth of information and communications technology-based educational tools generates a large volume of student data with many features (characteristics). However, the mining process in the clustering task of student data is not often done optimally, so the performance of the system decreases. To overcome this problem, we propose a discretization method on logistic regression to determine the most optimal number of clusters. Additionally, we introduce a technique that combines the features selection using a filter- and wrapper-based procedures (HFS) to identify the dominant features of the students' cognitive domains. Furthermore, we evaluate the identification result by three clustering methods, namely: K-means, EM, and

Farthest first. Finally, we propose the clustering-based classification so the results can be measured by using the classification metrics. Here, we apply two evaluation techniques, namely: cross-validation and percentage split. The experimental results indicate that our approach describes predominance, in terms of classification metrics over conventional methods. Our approach is around 10,847-11,134 percent higher in terms of accuracy average than the original features on both the assessment techniques. Also, this approach significantly reduces the time taken to create a prototype between 0.0167-0.027 seconds. This gives the impact on a significant reduction in the model created to the number of unsuitable students on classes based on the cognitive domain, namely: 3-12 students.

Spin-Pump-Induced Spin Transport in a Thermally-Evaporated Pigment-Red Film

Kazuhiro NISHIDA, Yoshio TEKI (Graduate School of Science, OCU), Eiji SHIKOH

Solid State Communications, Vol.312, pp.113898-1 ~ 113898-5 (2020).

We report the spin transport properties in a pigment-red (perylene-3,4,9,10-tetracarboxylic dianhydride: PTCDA) film prepared by thermal evaporation. In a palladium(Pd)/PTCDA/Ni₈₀Fe₂₀ tri-layer sample, a pure spin-current is generated in the PTCDA layer by using the spin-pumping driven by the ferromagnetic resonance of the Ni₈₀Fe₂₀ film. The generated spin current is absorbed into the Pd layer, converted into a charge current with the inverse spin-Hall effect in Pd, and detected as an electromotive force. This is clear evidence for the spin transport in a PTCDA film, and it is confirmed that a PTCDA film is useful not only as a robust protection layer material but also as a spintronic material.

Creation and Stabilisation of Tuneable Open Metal Sites in Thiocyanato-Bridged Heterometallic Coordination Polymers to Be Used as Heterogeneous Catalysts

Hiroyasu TABE, Masaaki MATSUSHIMA, Rika TANAKA, Yusuke YAMADA

Dalton Trans., Vol. 48, pp. 17063-17069 (2019)

A series of thiocyanato-bridged heterometallic coordination polymers with 3D reticular network have been synthesised by the reaction of $[\text{Pt}^{\text{IV}}(\text{SCN})_6]^{2-}$ with M^{II} ions to form $\{\text{M}^{\text{II}}[\text{Pt}^{\text{IV}}(\text{SCN})_6]\}_n$ and $\{[\text{M}^{\text{II}}(\text{CH}_3\text{OH})_2][\text{Pt}^{\text{IV}}(\text{SCN})_6]\}_n$ ($\text{M}^{\text{II}} = \text{Mn}^{\text{II}}, \text{Fe}^{\text{II}}, \text{Co}^{\text{II}}, \text{Ni}^{\text{II}}$ or Cu^{II}) in water and methanol, respectively. Single-crystal X-ray analyses manifested the absence of open metal sites in $\{\text{M}^{\text{II}}[\text{Pt}^{\text{IV}}(\text{SCN})_6]\}_n$ s and formation of potential open metal sites at M^{II} ions of $\{[\text{M}^{\text{II}}(\text{CH}_3\text{OH})_2][\text{Pt}^{\text{IV}}(\text{SCN})_6]\}_n$ s by coordination of methanol. One of the two coordinating methanol molecules in $\{[\text{Co}^{\text{II}}(\text{CH}_3\text{OH})_2][\text{Pt}^{\text{IV}}(\text{SCN})_6]\}_n$ was replaced by pyridine to stabilise the open metal sites, because the methanol molecules are too labile to maintain open metal sites in water. Heterogeneous catalysis of coordination polymers with and without open metal sites was examined for organophosphate hydrolysis and photocatalytic water oxidation to clarify requisites to be used as heterogeneous catalysts.

Unique Half Embedded/Exposed PdFeCu/C Interfacial Nanoalloy as High-Performance Electrocatalyst for Oxygen Reduction Reaction

Biraj Jyoti BORAH, Himadri SAIKIA, Chiranjita GOSWAMI, Kumar Kashyap HAZARIKA, Yusuke YAMADA, Pankaj BHARALI

ChemCatChem, Vol. 11, pp. 3522-3529 (2019)

Design of high-performance non-Pt electrocatalyst for fuel cell applications is greatly anticipated. Herein, we have developed a unique half-embedded and half-exposed interfacial PdFeCu nanoalloy anchored onto carbon matrix. The stable electronic coupling between the carbon matrix and PdFeCu nanoalloy possess very fast interfacial electron transfer which in turn enhances the electron conductivity. This makes the trimetallic nanoalloy high performing oxygen reduction reaction (ORR) electrocatalyst in both basic and acidic media. The PdFeCu/C nanoalloy exhibits enhanced electrochemically active surface area than various PdFe/C bimetallics as well as benchmark 20 wt% Pt/C and Pd/C. As a result, it offers larger active sites for ORR and eased the electron transport during the electrocatalysis. It exhibits 1.5- and 2.4-fold higher mass activity in comparison to the Pt/C and Pd/C. Furthermore, it exhibits long-term stability and low onset potential compared to those of the other catalysts. Thus, the present investigation shows potential strategy for the design and synthesis of Pt-free electrocatalyst with remarkable catalytic activity and stability.

Utilization of Core-Shell Nanoparticles to Evaluate Subsurface Contribution to Water Oxidation Catalysis of $[\text{Co}^{\text{II}}(\text{H}_2\text{O})_2]_{1.5}[\text{Co}^{\text{III}}(\text{CN})_6]$ Nanoparticles

Hiroyasu TABE, Akira KITASE, Yusuke YAMADA

Appl. Catal. B, Vol. 262, Article No. 118101 (8 pages) (2020)

Nanoparticles of a cyano-bridged polynuclear metal complex, $[\text{Co}^{\text{II}}(\text{H}_2\text{O})_2]_{1.5}[\text{Co}^{\text{III}}(\text{CN})_6]$, have been reported as highly efficient heterogeneous catalysts for photocatalytic water oxidation, however, reasons for the high catalytic activity have yet to be clarified. Herein, the water oxidation catalysis was investigated for a series of core-shell nanoparticles composed of cyano-bridged polynuclear metal complexes employing $[\text{Co}^{\text{II}}(\text{H}_2\text{O})_2]_{1.5}[\text{Co}^{\text{III}}(\text{CN})_6]$ as the shell to assess subsurface contribution. The catalytic activity of the core-shell nanoparticles closely related to that of the core parts suggests that the subsurface contributes to the nanoparticle catalysis. Then, catalysis of the core-shell nanoparticles employing $[\text{Cu}^{\text{II}}(\text{H}_2\text{O})_2]_{1.5}[\text{Fe}^{\text{III}}(\text{CN})_6]$ as the catalytically inactive core but isostructural to $[\text{Co}^{\text{II}}(\text{H}_2\text{O})_2]_{1.5}[\text{Co}^{\text{III}}(\text{CN})_6]$ was examined to determine the thickness directly involved in the catalytic reaction. The catalytic activity depending on the thickness of the $[\text{Co}^{\text{II}}(\text{H}_2\text{O})_2]_{1.5}[\text{Co}^{\text{III}}(\text{CN})_6]$ shell suggests the involvement of Co^{II} ions at the subsurface up to 7 nm. These results suggest that the microporous structure of $[\text{Co}^{\text{II}}(\text{H}_2\text{O})_2]_{1.5}[\text{Co}^{\text{III}}(\text{CN})_6]$ enlarged by intrinsic defects is a reason for the high catalytic activity, where the photosensitizer and water molecules utilize the subsurface Co^{II} ions as active sites.

Immobilization of $\text{Ir}(\text{OH})_3$ Nanoparticles in Mesospaces of Al-SiO_2 Nanoparticles Assembly to Enhance Stability for Photocatalytic Water Oxidation

Gentarō SAKAMOTO, Hiroyasu TABE, Yusuke YAMADA

Catalysts, Vol. 10, Article No. 1015 (14 pages) (2020)

Iridium hydroxide ($\text{Ir}(\text{OH})_3$) nanoparticles exhibiting high catalytic activity for water oxidation were immobilized inside mesospaces of a silica-nanoparticles assembly (SiO_2NPA) to suppress catalytic deactivation due to agglomeration. The $\text{Ir}(\text{OH})_3$ nanoparticles immobilized in SiO_2NPA ($\text{Ir}(\text{OH})_3/\text{SiO}_2\text{NPA}$) catalyzed water oxidation by visible light irradiation of a solution containing persulfate ion ($\text{S}_2\text{O}_8^{2-}$) and tris(2,2'-bipyridine)ruthenium(II) ion ($[\text{Ru}^{\text{II}}(\text{bpy})_3]^{2+}$) as a sacrificial electron acceptor and a photosensitizer, respectively. The yield of oxygen (O_2) based on the used amount of $\text{S}_2\text{O}_8^{2-}$ was maintained over 80% for four repetitive runs using $\text{Ir}(\text{OH})_3/\text{SiO}_2\text{NPA}$ prepared by the co-accumulation method, although the yield decreased for the reaction system using $\text{Ir}(\text{OH})_3/\text{SiO}_2\text{NPA}$ prepared by the equilibrium adsorption method or $\text{Ir}(\text{OH})_3$ nanoparticles without SiO_2NPA support under the same reaction conditions. Immobilization of $\text{Ir}(\text{OH})_3$ nanoparticles in Al^{3+} -doped SiO_2NPA ($\text{Al-SiO}_2\text{NPA}$) results in further enhancement of the catalytic stability with the yield of more than 95% at the fourth run of the repetitive experiments.

Single-Crystal-to-Single-Crystal Installation of $\text{Ln}_4(\text{OH})_4$ Cubanes in an Anionic Metallosupramolecular Framework

Nobuto YOSHINARI, Natthaya MEUNDAENG, Hiroyasu TABE, Yusuke YAMADA, Satoshi YAMASHITA, Yasuhiro NAKAZAWA, Takumi KONNO

Angew. Chem. Int. Ed., Vol. 59, pp. 18048-18053 (2020)

Post-synthetic installation of lanthanide cubanes into a metallosupramolecular framework via a single-crystal-to-single-crystal transformation is presented. Soaking single crystals of $\text{K}_6[\text{Rh}_4\text{Zn}_4\text{O}(\text{L-cys})_{12}]$ ($\text{L-H}_2\text{cys} = \text{L-cysteine}$) in a water/ethanol solution containing $\text{Ln}(\text{OAc})_3$ ($\text{Ln}^{3+} = \text{lanthanide ion}$) results in the exchange of K^+ by Ln^{3+} with retention of the single crystallinity, producing $\text{Ln}_2[\text{Rh}_4\text{Zn}_4\text{O}(\text{L-cys})_{12}]$ and $\text{Ln}_{0.33}[\text{Ln}_4(\text{OH})_4(\text{OAc})_3(\text{H}_2\text{O})_7][\text{Rh}_4\text{Zn}_4\text{O}(\text{L-cys})_{12}]$ for early and late lanthanides, respectively. While the Ln^{3+} ions in $\text{Ln}_2[\text{Rh}_4\text{Zn}_4\text{O}(\text{L-cys})_{12}]$ exist as disordered aqua species, those in $\text{Ln}_{0.33}[\text{Ln}_4(\text{OH})_4(\text{OAc})_3(\text{H}_2\text{O})_7][\text{Rh}_4\text{Zn}_4\text{O}(\text{L-cys})_{12}]$ form ordered hydroxide-bridged cubane clusters that connect $[\text{Rh}_4\text{Zn}_4\text{O}(\text{L-cys})_{12}]^{6-}$ anions in a 3D metal-organic framework through coordination bonds with carboxylate groups. This study shows the utility of an anionic metallosupramolecular framework with carboxylate groups for the creation of a series of metal cubanes that have great potential for various applications, such as magnetic materials and heterogeneous catalysts.

Unravelling the Role of Metallic Cu in Cu-CuFe₂O₄/C Nanohybrid for Enhanced Oxygen Reduction Electrocatalysis

Biraj Jyoti BORAH, Yusuke YAMADA, Pankaj BHARALI

ACS Appl. Energy Mater., Vol. 3, pp. 3488-3496 (2020)

Interface engineering of metal and semiconductive spinel oxides is an efficient approach to improve conductivity and ultimately boosting electrocatalytic property. Herein, we present the synthesis of Cu-CuFe₂O₄ nanohybrid coupled with conductive carbon (Cu-CuFe₂O₄/C) as a highly efficient electrocatalyst for oxygen reduction reaction (ORR). The metallic Cu and semiconductive oxide CuFe₂O₄ interface provides better electronic conductivity, and carbon matrix offers conductive support for electron/ion transfer process. Consequently, the Cu-CuFe₂O₄/C electrode exhibits superior current density (4.35 mA cm^{-2}) in comparison to the standard Pt/C (3.81 mA cm^{-2}) along with other catalyst systems toward ORR. Thus, the nanohybrid that combines the advantages of metallic Cu and chemical interaction of carbon matrix along with its magnetic behavior establishes remarkable enhancement in ORR activity. Furthermore, it also exhibits superior mechanical and electrochemical stability compared to that of Pt/C. Thus, the unique structural design offers a new approach for the fabrication of magnetic metal-oxides electrodes with enhanced ORR performance via interface engineering.

Relationship between Changes in Ionic Radius and Lattice Dimension of Lithium Manganese Oxide Spinel during Lithium Insertion/Extraction

Kingo ARIYOSHI, Hiroya YAMAMOTO, Yusuke YAMADA

Solid State Ionics, Vol. 343, Article No. 115077 (5 pages) (2019)

Dimensional stability is critical for the cyclability of Li insertion materials in Li-ion batteries. Thus, in this study, we characterize the dimensional change in a series of spinel-structured Li-Co-Mn oxides ($\text{LiCo}_x\text{Mn}_{2-x}\text{O}_4$) during Li insertion using ex-situ X-ray diffraction technique. We deduce that a change in the cubic lattice parameters of the $\text{LiCo}_x\text{Mn}_{2-x}\text{O}_4$ compounds during Li insertion depends on the solid-state redox reactions; in particular, a smaller dimensional change is observed for the $\text{Co}^{3+}/\text{Co}^{4+}$ redox

reaction, while a larger change is observed for the $\text{Mn}^{3+}/\text{Mn}^{4+}$ redox reaction. Through our X-ray diffraction studies, a linear relationship between the change in ionic radii of the redox species and dimensional change in the lattice structure of the compounds was observed during the reactions, which can be adopted for other Li-Mn oxide spinels as well. Hence, this relationship provides useful insight for designing Li insertion materials with high dimensional stability for long-life Li-ion batteries.

Elucidation of the Origin of Voltage Hysteresis in $x\text{Li}_2\text{MnO}_3 \cdot (1-x)\text{LiCoO}_2$ using Backstitch Charge-Discharge Method

Kingo ARIYOSHI, Takayuki INOUE, Yusuke YAMADA

Electrochim. Acta, Vol. 334, Article No. 135623 (8 pages) (2020)

Lithium-excess (LEX) materials with a composition of $x\text{Li}_2\text{MnO}_3 \cdot (1-x)\text{LiMO}_2$ ($\text{M} = \text{Fe}, \text{Co}, \text{or Ni}$) exhibit large reversible capacities and are therefore promising positive electrode materials for Li-ion batteries. However, the widespread application of these materials is hindered by their large voltage hysteresis, cycling-induced voltage decay, and long initial-cycle voltage plateau. Herein, Co-LEX materials with the composition of $x\text{Li}_2\text{MnO}_3 \cdot (1-x)\text{LiCoO}_2$ are synthesized and electrochemically characterized using the backstitch charge-discharge method to elucidate the origin of voltage hysteresis. A trade-off relationship between reversible capacity and energy efficiency is observed, and both reversible capacity and voltage hysteresis extent increase with increasing Mn content. Quantitative analysis of voltage hysteresis by the backstitch charge-discharge method reveals that the energy loss per cycle due to the difference in reversible potentials during charge and discharge is proportional to oxide redox reaction-derived capacity, which indicates that voltage hysteresis is caused by the solid-phase redox reactions of lattice oxide ions. Thus, electrode potentials of solid-state oxide redox reactions are necessary to be matched in order to achieve both high reversible capacity and low voltage hysteresis for LEX materials.

Mechanism of Mg Extraction from MgMn_2O_4 during Acid Digestion

Kingo ARIYOSHI and Shumpei MASUDA

Phys. Chem. Chem. Phys., Vol. 22, pp. 4677-4684 (2020)

MgMn_2O_4 having a spinel structure is a very attractive material for the positive electrode in Mg-ion batteries, since its reversible Mg extraction/insertion reaction can lead to a large reversible capacity. While the Mg extraction from MgMn_2O_4 has been reported, the reaction mechanism remains unclear. In this paper, Mg ions were chemically extracted from MgMn_2O_4 by acid digestion at various concentrations to produce $\text{Mg}_x\text{Mn}_2\text{O}_4$ ($0 < x < 1$). The results showed that Mg extraction from MgMn_2O_4 is a two-step two-phase reaction, via the intermediate $\text{Mg}_{0.5}\text{Mn}_2\text{O}_4$ to the fully oxidized Mn_2O_4 . The kinetics of Mg extraction was clarified using acid digestion experiments of different durations, and the direct reaction pathway of MgMn_2O_4 oxidation to $\lambda\text{-MnO}_2$ was the fastest process. This may explain the difficulty in Mg extraction from MgMn_2O_4 using electrochemical methods.

Improvement of Float Charge Durability for LiCoO_2 Electrodes under High Voltage and Storage Temperature by Suppressing O1-Phase Transition

Motoyuki HIROOKA, Tomohito SEKIYA, Yoshitomo OMOMO, Masayuki YAMADA, Hideaki KATAYAMA, Takefumi OKUMURA, Yusuke YAMADA, Kingo ARIYOSHI

J. Power Sources, Vol. 463, Article No. 228127 (7 pages) (2020)

To produce electronic devices with high functionality and longer operating times, the energy density of lithium ion batteries (LIBs) has to be increased while maintaining a long battery life and high reliability. The energy density of LIBs can be increased by increasing the charge cut-off voltage. The float charge durability of LIBs containing LiCoO_2 under high voltage is one of the most important issues in practical use. The leakage current during float charge conditions is caused by the O1 phase transition of LiCoO_2 . In this study, metal-substituted lithium cobalt oxides, $\text{LiCo}_{1-x}\text{M}_x\text{O}_2$ ($\text{M} = \text{Co}, \text{Ni}, \text{Al}, \text{Mg}, \text{and Zr}$), were investigated to suppress degradation during float charge conditions. When Ni was substituted for Co at an amount of 5%, the float charge durability improved more than 4 times compared to bare- LiCoO_2 without lowering the energy density. According to the structural analysis, we proposed the mechanism for improving float charge durability by $\text{LiCo}_{1-x}\text{Ni}_x\text{O}_2$; Ni ions partially migrate to the lithium layer and then stabilize the O3 structure. This Ni ions substitution in LiCoO_2 greatly contributes to extending life and the safety of high energy density LIBs containing layered positive materials.

Reaction Mechanism and Kinetic Analysis of the Solid-State Reaction to Synthesize Single-Phase $\text{Li}_2\text{Co}_2\text{O}_4$ Spinel

Kingo ARIYOSHI, Kazuki YUZAWA, Yusuke YAMADA

J. Phys. Chem. C, Vol. 124, pp. 8170-8177 (2020)

Lithium cobalt oxide has two polymorphs that display different electrochemical properties despite their identical redox reactions: a high temperature phase having a layered structure (LiCoO_2 ; HT-LCO) and a low temperature phase with a spinel framework ($\text{Li}_2\text{Co}_2\text{O}_4$; LT-LCO). The synthetic conditions of the single-phase LT-LCO were determined by thermogravimetric analysis performed on the solid-state reaction of Li_2CO_3 and Co_3O_4 . The results revealed that LCO synthesis was a second-order reaction with an activation energy of $E_a = 150 \text{ kJ mol}^{-1}$ and a pre-exponential factor of $A = 9.2 \times 10^7 \text{ s}^{-1}$. XRD studies indicated that low-temperature synthesis below 350°C is necessary to obtain the single-phase LT phase because the HT phase fraction increased with increasing synthesis temperature. Virtually single-phase LT-LCO obtained by calcining at 325°C for 240 h exhibited zero-strain lithium insertion. These results contribute toward the establishment of a synthetic method for novel materials with reduced spinel structure.

Self-Discharge Tests to Measure Side-Reaction Currents of a $\text{Li}[\text{Li}_{1/3}\text{Ti}_{5/3}]\text{O}_4$ Electrode

Kingo ARIYOSHI, Takahide TODA, Yusuke YAMADA

J. Electroanal. Chem., Vol. 864, Article No. 228127 (5 pages) (2020)

The lifetime performance of lithium-ion batteries is a critical issue for automobile and stationary applications. The difference in the side-reaction current (I_{SR}) of electrodes causes deviations of the state of charge (SOC) of the electrodes leading to the capacity fading of lithium-ion batteries. Establishment of a method to measure the I_{SR} is important for understanding the capacity fading mechanism. We report herein that a novel and simple method to determine the ISR in lithium-ion batteries, the self-discharge test, was developed and applied to lithium-ion cells with lithium titanium oxide ($\text{Li}[\text{Li}_{1/3}\text{Ti}_{5/3}]\text{O}_4$, LTO), lithium aluminum manganese oxide ($\text{Li}[\text{Li}_{0.1}\text{Al}_{0.1}\text{Mn}_{1.8}]\text{O}_4$, LAMO), and lithium nickel manganese oxide ($\text{Li}[\text{Ni}_{1/2}\text{Mn}_{3/2}]\text{O}_4$, LiNiMO) as electrodes. According to the self-discharge test results, the I_{SR} of LTO is affected by another electrode of LAMO or LiNiMO. The I_{SR} of LTO in LTO/LiNiMO cells larger than that in LTO/LAMO cells is explained by the additional- I_{SR} of LTO, which results from side reactions such as the reduction of oxidized products generated at the positive electrode. The side reactions at the positive electrode are accelerated with increasing electrode potential, meaning that the higher potential of the positive electrode resulted in the larger additional- I_{SR} of LTO. The real side-reaction current of the LTO electrode in lithium-ion cells is the sum of the intrinsic and the additional current (real- $I_{\text{SR}} = \text{intrinsic-}I_{\text{SR}} + \text{additional-}I_{\text{SR}}$).

Examining the Long-Term Cyclabilities of $\text{Li}[\text{Ni}_{1/2}\text{Mn}_{3/2}]\text{O}_4$ and $\text{Li}[\text{Li}_{0.1}\text{Al}_{0.1}\text{Mn}_{1.8}]\text{O}_4$ Using a Full-Cell Configuration Including LTO-Counter Electrodes with Extra Capacity

Kingo ARIYOSHI, Makoto EGUCHI, Motoyuki HIROOKA

J. Electrochem. Soc., Vol. 167, Article No. 060532 (5 pages) (2020)

In this study, a novel cell configuration was developed for evaluating the cyclabilities of lithium insertion materials. In this cell, the $\text{Li}[\text{Li}_{1/3}\text{Ti}_{5/3}]\text{O}_4$ (LTO) counter electrode has excess capacity on both the charge and discharge sides (EQ-LTO). The EQ-LTO/ $\text{Li}[\text{Ni}_{1/2}\text{Mn}_{3/2}]\text{O}_4$ (LiNiMO) cell shows superior cyclability when compared to other cell configurations, such as Li/LiNiMO and LTO/LiNiMO cells. In Li/LiNiMO cells, drastic capacity fading is observed within 100 cycles. While LTO/LiNiMO cells are suited for long-term use, capacity fading occurs mainly due to the different charge states of LTO and LiNiMO rather than the deterioration of LiNiMO. Herein, long-term (more than 6 months) cycling tests are performed for $\text{Li}[\text{Li}_{0.1}\text{Al}_{0.1}\text{Mn}_{1.8}]\text{O}_4$ (LAMO) in an EQ-LTO cell to assess whether this cell configuration is suitable for evaluating long term cyclabilities; LAMO in this cell shows higher capacity retention than that in an LTO cell. The capacity fading as a function of cycle number is found to be very small for LAMO ($10 \text{ ppm cycle}^{-1}$). From these results, we concluded that the EQ-cell configuration provides accurate capacity fading values for lithium insertion materials.

Scanning and Full Field X-Ray Fluorescence Imaging with Laboratory X-ray Source

Kouichi TSUJI, Momotaro NAKANISHI, Ryouta OZEKI, Tsugufumi MATSUYAMA

Extended Abstract of PSA-19(review), *Journal of Surface Analysis*, Vol. 26, No. 2, pp. 116-117 (2019)

Many applications of x-ray fluorescence (XRF) analysis have been reported in various fields, such as in the environmental, archeological, biological, and forensic sciences as well as in industry. Elemental analysis near surface region is performed by XRF. Advanced x-ray focusing optics such as polycapillary optics enables a micro x-ray beam with a laboratory x-ray source, leading to micro-XRF analysis and scanning-mode XRF

imaging. A confocal micro-XRF technique has been applied for the visualization of elemental distributions inside the samples. In parallel, the authors have studied a wavelength dispersive XRF (WDXRF) imaging spectrometer for a fast elemental imaging. A full-field energy dispersive X-ray fluorescence (FF-EDXRF) imaging spectrometer using single photon counting analysis with xray camera was also studied. We evaluated and discussed the performance of laboratory-made these scanning- and FFimaging spectrometers concerning energy resolution, spatial resolution, quantitative performance and elemental imaging. At the end, compressed sensing which is one of general information processing technique was applied for high-resolution XRF images.

Depth Elemental Imaging during Corrosion of Hot-Dip Galvanized Steel Sheet by Confocal Micro XRF Analysis

Koji AKIOKA, Takashi DOI, Shohei MITA, Tsugufumi MATSUYAMA, Kouichi TSUJI
Analytical Sciences, Vol. 36, pp 55-59 (2020)

The elucidation of the mechanism for steel corrosion under a coating layer has been attracting research attention. Herein, we utilized a confocal micro-X-ray fluorescence (XRF) analytical instrument to conduct non-destructive elemental obtained without sample destruction. To confirm corrosion suppression in the presence of Mg ions, we observed the corrosion behavior of hot-dip galvanized steel sheets immersed in an aqueous NaCl solution to which Mg ions were added. By using the confocal micro XRF system, the elution of the coating components and the precipitation process of the corrosion products were confirmed.

Development of Full-field XRD (FFXRD) Imaging Method Realized in the Laboratory Using a Straight Polycapillary and in situ Observation of the Oxidation Process of Cu by Heat Treatment

Masaki YAMANASHI, Kouichi TSUJI
e-Journal of Surface Science and Nanotechnology, Vol. 18, pp. 1–7 (2020)

We developed a full-field X-ray diffraction (FFXRD) imaging method using a straight polycapillary realized in the laboratory that can obtain X-ray diffraction (XRD) images with a large area in a short time throughout the simple process without the synchrotron radiation facility. The FFXRD imaging instrument can obtain the XRD images of several millimeter sizes in several hundreds of seconds at each lattice plane. The positional resolution and the spatial resolution was improved by using a straight polycapillary with long type. The FFXRD imaging instrument was attached to the heat treatment system and Cu plate was heat-treated at 300°C. As an example of *in situ* monitoring of the change in the crystal structure distribution, a high-temperature oxidation process of Cu was observed. The XRD images of Cu, Cu₂O, and CuO at each lattice plane were obtained every hour. While the crystal structure distribution of Cu was reduced, the crystal structure distribution of Cu₂O and CuO were increased with the oxidation process of Cu by the heat treatment. The change of the crystal structure distribution near the surface by the oxidation process of Cu was confirmed. The XRD image obtained by the FFXRD imaging instrument was analyzed by micro-XRD measurements and confirmed that the FFXRD imaging instrument can accurately obtain the crystal structure distribution. In order to obtain the XRD image with a large area, the FFXRD imaging instrument that can be realized in the laboratory has advantages regarding the exposure time of X-rays and *in situ* analysis.

Super Resolution Analysis of X-ray Fluorescence Imaging Using Compressed Sensing Technique

Tsugufumi MATSUYAMA, Aoi YAMAUCHI, Masahiro IWASAKI, Kazunori HAYASHI, Kouichi TSUJI
Adv. X-Ray. Chem. Anal., Japan, Vol.51, pp. 49-56 (2020) (in Japanese)

Full field type X-ray fluorescence analysis is useful technique for obtaining element distribution images by using 2D camera. This method is expected to be applied to various fields, however it is required to improve the resolution of elemental images. Therefore, we aimed to obtain high-quality elemental distribution images by applying a compressed sensing technique to full-field X-ray fluorescence imaging. In this paper, usefulness of the analytical method was demonstrated by showing the elemental images of a metal sample composed of copper and titanium plates.

Improvement of Spatial Resolution of Micro-XRF Instrument by Shifted Confocal Micro-XRF Configuration

Kazuhiko NAKANO, Shintaro KOMATANI, Atsushi BANDO, Hiroshi UCHIHARA, Kouichi TSUJI
Adv. X-Ray. Chem. Anal., Japan, Vol.51, pp. 57-63 (2020) (in Japanese)

An improvement of spatial resolution of micro-XRF by a “shifted confocal micro-XRF configuration” was investigated. In the shifted confocal configuration, the focus points on the incident side and the detection side are intentionally shifted from the conventional confocal setup, and the area where both the focal points coincide with each other is narrowed to improve the spatial resolution. Although the obtained XRF intensities were

reduced, the spatial (depth and in-plane) resolutions were improved by more than 10%.

Trace Element Analysis Using Total Reflection X-ray Fluorescence Spectrometry and Research Trends of the Countries ~TXRF2019 Conference Report~

Tsugufumi MATSUYAMA, Yukie IZUMOTO, Hiroshi YOSHII, Kouichi TSUJI

Adv. X-Ray. Chem. Anal., Japan, Vol.51, pp. 261-270 (2020) (in Japanese)

Monochromatic Confocal Micro X-Ray Fluorescence Spectrometry

Naoki KAWAHARA, Shota SONODA, Shohei MITA, Tsugufumi MATSUYAMA, Kouichi TSUJI

Advances in X-ray Analysis, Vol. 63, pp. 125-131 (2020)

Confocal micro x-ray fluorescence (CM-XRF) spectrometry enables non-destructive elemental analysis, allowing collection of 3D spatially resolved data to probe the inside of samples. In laboratory CM-XRF instruments, polychromatic x-ray focusing sources formed by using an x-ray tube and a polycapillary full-lens optic have been utilized. In this case, high background is one of the problems for trace elemental analysis. In this paper, we report the preliminary results from a CM-XRF using a monochromatic source. Clear XRF elemental images were obtained with low background.

Development of Fly-scan mode Confocal Micro X-ray Fluorescence Analysis

Tsugufumi MATSUYAMA, Shohei MITA, Momotaro NAKANISHI, Kouichi TSUJI

Advances in X-ray Analysis, Vol. 63, pp. 132-139 (2020)

Confocal micro-X-ray fluorescence (CM-XRF) is a useful technique for 3D element mapping of various types of samples. In CM-XRF, a micro X-ray beam is generated through optical focusing of X-rays. Thus far, CM-XRF has only been performed in step-by-step mode, with the drawback of prolonged measurement times required for elemental mapping, depending on the area being measured. In our study, we have applied CM-XRF in fly-scan mode, where continuous XRF is performed simultaneously with sample scanning. Because fly-scan mode collects XRF data during the sample scanning stage without stopping the motor at illumination spots, elemental mapping is achieved in a shorter time compared with the conventional method. In this study, a copper plate was selected as the illumination sample, and its profiles were measured using fly-scan and step-by-step CM-XRF methods. In fly-scan mode, the sample stage motor was moved at four different speeds, and we found that more distinct profiles were obtainable at lower scanning speeds. The copper profile was obtained within approximately 30 min with fly-scan mode, while step-by-step mode required approximately 150 min. Therefore, by employing CM-XRF with fly-scan mode, it is possible to produce clear elemental profiles in a short scanning time.

Elemental Mapping of Pasta Sample Using Confocal Micro X-Ray Fluorescence Spectrometry

Hitomi NAKANO, Yumiko NAKANISHI, Shohei MITA, Momotaro NAKANISHI, Shintaro KOMATANI, Kouichi TSUJI

Advances in X-ray Analysis, Vol. 63, pp. 140-150 (2020)

X-ray fluorescence (XRF) spectrometry enables non-destructive elemental analysis. In this paper, we visualized chlorine (Cl) distribution in boiled pasta by using confocal micro X-ray fluorescence (C-M-XRF). C-M-XRF can obtain 3D mapping images. A problem is that XRF from the inner area of sample is susceptible to absorption. It was found that the XRF intensity of Cl was higher on the surface of the pasta and lower at the center. It was identified that Cl was detected at 300 μm depth by C-M-XRF. In this study, we corrected the influence of the XRF absorption effect inside the sample when confocal X-ray fluorescence analysis was used. It was confirmed that the Cl distribution of the C-M-XRF was consistent with the Cl distribution of sample cross section measured by the conventional micro-XRF. Therefore, we conclude that CM-XRF is an effective non-destructive method for the evaluation of salt penetration near the surface of food samples.

Concept model of atomic hydrogen dry developing process for photolithographic patterning

Yuki Takemori, Masao GOHDO, Yuta KODA, Hideo HORIBE

AIP Advances, Vol.10, Article No.105223 (2020)

Atomic hydrogen dry etching was used for microstructure fabrication. Photolithography was proposed and achieved by a dry development process using atomic hydrogen irradiation. The reaction system of poly(methyl methacrylate) mixed with molecular benzophenone was examined as a model system for a proof-of-concept study. Optical patterning was experimentally made on a thin layer of poly(methyl methacrylate) with benzophenone by UV light exposure with a photomask. The reaction system acted as a negative tone resist in the proposed process. Thus, a model system for a new atomic hydrogen dry development process was proposed

and successfully demonstrated.

Effect of *pgsE* expression on the molecular weight of poly (γ -glutamic acid) in fermentative production
Ken-Ichi FUIJITA, Takashi TOMIYAMA, Takahiro INOI, Takashi MISHIYAMA, Eriko SATO, Hideo HORIBE, Ryosuke TAKAHASHI, Shinichi KITAMURA, Yoshihiro YAMAGUCHI, Akira OGITA, Toshio TANAKA

Polymer J., in print (2020)

Poly(γ -glutamic acid) (PGA) is a biopolymer produced by *Bacillus* spp. via the γ -amide linkages of D- and/or L-glutamate. Although high-molecular-weight (HMW) PGA possesses many attractive properties, such as flocculating, wound healing, and immune-stimulating effects, no studies have reported factors useful for increasing the molecular weight of PGA during microbial production. PgsB, PgsC, and PgsA are the minimum protein sets required for PGA production in *B. subtilis*, and PgsE improves PGA productivity. Analysis by size-exclusion chromatography combined with multiangle laser light scattering revealed that the molecular weight of PGA was $M_w = 2,900,000 \text{ g mol}^{-1}$ and predominantly $M_w = 47,000 \text{ g mol}^{-1}$ in preparations derived from *B. subtilis* cells with and without *pgsE*, respectively. PgsE may be required to increase the molecular weight of PGA.

Thermoresponsive Conductivity of Acrylamide-Based Polymers and Ni Microparticle Composites

Hayato ONISHI, Yuta KODA, Hideo HORIBE

Chem. Lett., vol.49(10), in print (2020)

Composite materials with polymers and inorganic fillers enable the preparation of a variety of functional polymer materials. In particular, composites with crystalline polymers and Ni microparticles (NiMPs) can be applied to thermoresponsive conductive materials which are called PTC (positive temperature coefficient) materials. These materials are conductive around room temperature, and turn to insulators at high temperature. This phenomenon is induced by the volume expansion of the crystalline domains, therefore, the design of matrix polymers has been limited. Herein, we showed PTC phenomena by using polyacrylamide-based (co)polymers in lieu of crystalline polymers. Those materials showed PTC phenomena regarding conductivity probably owing to the hydrogen bonding, yet polyacrylamides are amorphous polymers.

Microanalysis of Single Poly(*N*-isopropylacrylamide) Droplet Produced by an Optical Tweezer in Water: Isotacticity Dependence of Growth and Chemical Structure of the Droplet

Kenta USHIRO, Tatsuya SHOJI, Mitsuhiro MATSUMOTO, Taka-Aki ASOH, Hideo HORIBE, Yukiteru KATSUMOTO, Yasuyuki TSUBOI

J. Phys. Chem. B, vol.124(38), pp8454–8463 (2020)

Thermoresponsive phase separation mechanisms of aqueous poly(*N*-isopropylacrylamide) (PNIPAM) solutions were investigated using an optical tweezer combined with a Raman microspectroscope. A near-infrared laser beam ($\lambda = 1064 \text{ nm}$) was focused into the solution to produce and trap a single polymer microdroplet under an optical microscope. The laser beam played two important roles: The first role is to locally heat the solution to induce phase separation in which numerous polymer microdroplets are generated around the focus, while the second one is to collect these microdroplets. Eventually, a single polymer droplet was stably produced and trapped at the focus. Our method enabled us to perform two types of microanalysis for the droplet. Analysis I is real-time monitoring the growth of the polymer droplets by which we can determine the growth rate of droplets. Analysis II is Raman microspectroscopy to reveal chemical components of the droplets. By means of these two analyses, we revealed important phase separation mechanisms in terms of stereoregularity (isotacticity) dependence. From analysis I, we show that droplet growth is governed by the Ostwald ripening mechanism and the growth is accelerated by increasing the isotacticity. From analysis II, we show that the gelation is promoted in the droplet (physical gel formation) with increasing isotacticity. Our technique should be a versatile tool to explore liquid–liquid phase separation mechanisms for various binary solution systems.

Effects of Nitrogen Dilution on the Photoresist Removal Rate by Hydrogen Radicals

Masashi YAMAMOTO, Hiroto NISHIOKA, Koki AKITA, Shiro NAGAOKA, Hironobu UMEMOTO, Hideo HORIBE

J. Photopolymer Sci. and Technol., vol.33(4), pp427–431(2020)

We have previously demonstrated that photoresist removal rate comparable to oxygen plasma is accomplished by optimizing the removal conditions with H radicals produced on hot metal filament surfaces from H_2/N_2 mixtures ($\text{H}_2:\text{N}_2 = 10:90 \text{ vol}\%$). N_2 gas was used to dilute the concentration of the H_2 gas and to reduce

the risk of explosion. However, it is not clear how the dilution of H₂ by N₂ affects the removal rate. In this paper, we examined the relationship between the removal rate and the H₂ content; the flow rate ratio of H₂ to H₂+N₂. The removal rate increased with increasing the H₂ content. In addition, the removal rate increased with increasing the substrate temperature according to an Arrhenius equation, when the H₂ content was over 90%. However, below 60%, the removal rate decreased with increasing the temperature over 230 ± 5 °C. Denaturation of photoresist, e.g. hardening and/or crosslinking, may be induced by substrate heating when the H-radical density is low. The removal rate decreases not only by the deficiency of H radicals but also by the denaturation of films in H₂/N₂ mixed systems.

Evaluation of Decomposition Property of Photoresist by Oxygen Radicals Using Helium-Oxygen Mixtures

Masashi YAMAMOTO, Koki AKITA, Koki AKITA, Shiro NAGAOKA, Hironobu UMEMOTO, Hideo HORIBE

J. Photopolymer Sci. and Technol., vol.33(4), pp433-437(2020)

We have previously demonstrated that photoresist removal rate is enhanced by adding a trace amount of O₂ to the atmosphere in which H radicals are produced from H₂ on a hot metal filament. In this case, not only H radicals but also O and OH radicals are produced. The populations of O and OH radicals are a few hundredth parts of that of H radicals, but these radicals must play important roles. It is not clear which radicals contribute more to the enhancement of the removal rate. We used He/O₂ mixtures in this study, instead of H₂/O₂, to produce O radicals without co-producing H and OH to make clear the contribution of O radicals on the removal rate. The removal rate increased slightly with increasing the O₂ additive amount when the filament was unheated. This may be caused by thermal oxidation. On the other hand, the removal rate with a hot filament decreased by the addition of O₂. In short, the removal rate is not enhanced by O radicals. The enhancement in H₂/O₂ mixtures must only be ascribed to OH radicals.

Facile Synthesis of Graft Copolymers Containing Rigid Poly(dialkyl fumarate) Branches by Macromonomer Method

Eriko SATO, Noboru TAMARI, Hideo HORIBE

J. Polym. Sci.: Part A, Polym. Chem., Vol. 40(24), pp. 2474-2480 (2019)

Graft copolymers show microphase separated structure as seen in block copolymers and have lower intrinsic viscosity than block copolymers because of a branching structure. Therefore, considering molding processability, especially for polymers containing rigid segments, graft copolymers are useful architectures. In this work, graft copolymers containing rigid poly(diisopropyl fumarate) (PDiPF) branches were synthesized by full free-radical polymerization process. First, synthesis of PDiPF macromonomers by addition-fragmentation chain transfer (AFCT) was investigated. 2,2-Dimethyl-4-methylene-pentanedioic acid dimethyl ester was found to be an efficient AFCT agent for diisopropyl fumarate (DiPF) polymerization because of the suppression of undesired primary radical termination, which significantly took place when common AFCT agent, methyl 2-(bromomethyl)acrylate, was used. Copolymerization of PDiPF macromonomer with ethyl acrylate accomplished the generation of the graft copolymer having flexible poly(ethyl acrylate) backbone and rigid PDiPF branches. The graft copolymer showed a microphase separated structure, high transparency, and characteristic thermal properties to PDiPF and poly(ethyl acrylate).

Synthesis and Evaluation of Thermally Curable Hyperbranched Polymers with Low Glass Transition Temperature

Izumi UEHARA, Seidai OKADA, Hideo HORIBE, Eriko SATO

Journal of Network Polymer, Japan, Vol. 41(3), pp. 113-120 (2020) (in Japanese)

Network polymers show excellent properties such as a high mechanical strength and solvent resistance. On the other hand, the removal of network polymers is difficult due to insolubility. In order to solve the issue, de-cross-linkable network polymers have attracted much attention. In this review, the design of network polymers having degradable units is introduced with focusing on the main-chain degradable polyperoxides-based network polymers and curable hyperbranched polymers having dense degradable linkages. Curable adhesives are one of the applications of network polymers, and de-cross-linkable network polymers can be used as dismantlable adhesives, which demonstrate both sufficient bonding strength in use and easy debonding on demand. Increase in bonding strength by the network formation and debonding by decreasing a mechanical strength and solubilization in response to de-cross-linking are reported.

Tuning of Optical Properties and Thermal Cycloreversion Reactivity of Photochromic Diarylbenzene

by Introducing Electron-Donating Substituents

Tatsumoto NAKAHAMA, Daichi KITAGAWA, Seiya KOBATAKE

J. Phys. Chem. C, Vol. 123(51), pp. 31212-31218 (2019).

Thermally reversible photochromic compounds having excellent physicochemical properties can be exploited for many practical applications, such as ophthalmic lenses, real-time holography, and super-resolution microscopy. In this study, we have designed and synthesized novel 1,2-diarylbenzene derivatives bearing various electron-donating substituents at the *p*-position of the phenyl ring to tune the optical and thermal properties for practical applications. The introduction of the electron-donating groups resulted in the red shift of the absorption spectra, an increase in the absorption coefficients of the open-ring isomers, and deceleration of the thermal cycloreversion of the closed-ring isomers. Theoretical analysis based on Hammett's substituent constant and density functional theory revealed that the rate of thermal cycloreversion became lower in proportion to the electron-donating ability of the substituent. The novel 1,2-diarylbenzene derivatives synthesized here could undergo photocyclization upon irradiation with UV-A light and fast thermal cycloreversion with a half-life of a few hundred milliseconds to seconds.

Synthesis and Fluorescence On/Off Switching of Hyperbranched Polymers Having Diarylethene at the Branching Point

Katsuya SHIMIZU, Rémi MÉTIVIER, Seiya KOBATAKE

J. Photochem. Photobiol. A: Chem., Vol. 390, Article No. 112341 (8 pages) (2020).

We designed and synthesized hyperbranched polymers (HBPs) having diarylethene (DE) at branching points and having fluorene (FL) and DE derivatives between branching points in order to investigate the effect of the polymer structure to fluorescence on/off switching efficiency induced by the photochromic reaction of DE. First, HBP was synthesized by polymerization of an FL monomer (FL-St) in the presence of a DE monomer with reversible addition-fragmentation chain transfer unit (St-DE-RAFT) in the feed ratio of [FL-St]/[St-DE-RAFT]=10. The fluorescence intensity of the resulting HBP decreased linearly as a function of the photocyclization conversion of DE. The change in the fluorescence intensity accompanied by the photochromic reactions indicates that one DE closed-ring isomer can quench 16.9 neighboring FL moieties. However, the switching rate and on/off contrast of fluorescence were relatively low because the number of FL in the polymer chain is much larger than that of DE. Therefore, we synthesized two types of HBPs having DE positioned not only at the branching points but also integrated in the polymer chains with different branching degrees. The fluorescence intensity of FL for such HBPs showed a non-linear dependence on the photocyclization conversion of DE, and a significant emission decrease with high on/off contrast even in low conversion was demonstrated. One DE closed-ring isomer quenched 5.4–6.4 FL moieties, whereas the fluorescence quantum yield in the “on” state was found to be around 0.15. The quenching of FL molecules is more pronounced for higher branching degrees in the polymers, indicating that DE closed-ring isomer can quench efficiently FL molecules when located within the polymer chains as well as at the branching points of the polymer.

A Dominant Factor of the Cycloreversion Reactivity of Diarylethene Derivatives as Revealed by Femtosecond Time-Resolved Absorption Spectroscopy

Hikaru SOTOME, Kanako UNE, Tatsuhiro NAGASAKA, Seiya KOBATAKE, Masahiro IRIE, Hiroshi MIYASAKA

J. Chem. Phys., Vol. 152(3), Article No. 034301 (9 pages) (2020).

Dynamics of the cycloreversion reaction of a photochromic diarylethene derivative with a small ring-opening reaction yield (~1%) was investigated by using femtosecond transient absorption spectroscopy. The reaction rate constant and activation barrier on the reaction coordinate were quantitatively analyzed on the basis of the temperature and excitation wavelength dependencies of the reaction yield and excited state dynamics. From the comparison of the present results with those in a more reactive derivative, we concluded that a key factor regulating the overall reaction yield is the branching ratio at the conical intersection where the excited state population is split into the product and the initial reactant. The excitation wavelength dependence of the dynamics indicated that the geometrical relaxation and vibrational cooling proceed in a few picosecond time scale behind the cycloreversion process, and the vibrational excess energy assists the molecule to climb up the energy barrier.

Synthesis and Multicolor Emission Properties of Polystyrene with Difluoroboron Avobenzene Complexes at Side Chains

Katsuya SHIMIZU, Arisa OKUMA, Shiho KATSUMI, Fuyuki ITO, Seiya KOBATAKE

Dyes and Pigments, Vol. 177, Article No. 108283 (7 pages) (2020).

Random copolymers (poly(ABSt-co-St)) consisting of avobenzene-BF₂ complex monomer (ABSt) and styrene (St) were synthesized and used for emission color tuning including white-like emission in the solid state using St units as a spacer. The emission color of ABSt in the resulting copolymers changed from green to blue via bluish-white by changing the content of St. The fluorescence quantum yields of the polymers in the solid state were relatively high ($\Phi_f = 0.30$ -0.51) independent of the composition contents. The polymers have two main emission bands around 440 and 540 nm, which were derived from the emission of single-molecule and amorphous aggregation, respectively. The fluorescence color changed according to a change in the ratio of the fluorescence intensity at 440 and 540 nm (F_{440}/F_{540}). The absorption and fluorescence properties of the polymers in tetrahydrofuran were independent of the composition ratio of ABSt and St, which indicates no intermolecular interaction between avobenzene-BF₂ (AB) fluorophores in the intra-polymer chain. The emission color of all polymers in the solution was blue and the fluorescence spectra were the same as that of ABSt in the solution. Thus, emission color changes observed in the solid state were mainly derived from the intermolecular interaction between AB fluorophores in inter-polymer chains because the polymers intertwined each other in the solid state. When the polymers in the solid state were annealed, F_{440}/F_{540} increased and all of the fluorescence spectra became similar to that of monomer emission according to the arrangement change of the polymer chain. It is concluded that emission color changes of the polymers are mainly derived from intermolecular interaction between AB fluorophores in the inter-polymer chains. We have demonstrated that poly(ABSt-co-St) forms excellent homogeneous fluorescence polymer films. In contrast, the mixture of methoxy AB (ABOMe) and poly(St) undergoes crystallization even in the low content of ABOMe in poly(St).

Mechanical Actuation and Patterning of Rewritable Crystalline Monomer-Polymer Heterostructures via Topochemical Polymerization in a Dual-Responsive Photochromic Organic Material

Ranita SAMANTA, Daichi KITAGAWA, Amit MONDAL, Manjima BHATTACHARYA, Mari ANNADHASAN, Saikat MONDAL, Rajadurai CHANDRASEKAR, Seiya KOBATAKE, C. Malla REDDY *ACS Appl. Mater. Interf.*, Vol. 12(14), pp. 16856-16863 (2020).

The dark-orange monomer single crystals of 1,1'-dioxo-1*H*-2,2'-biindene-3,3'-diyl didodecanoate (BIT-dodeca₂) convert to a transparent single-crystalline polymer (PBIT-dodeca₂) material via a single-crystal-to-single-crystal (SCSC) polymerization reaction under sunlight, which then undergoes reverse thermal transformation into BIT-dodeca₂ single crystals, leading to reversible photo-/thermochromism, coupled with mechanical actuation. We exploit the properties of this unique material to demonstrate the formation of monomer-polymer heterostructures in selected regions of single crystals with micrometer-scale precision using a laser. This is the first example of heterostructure patterning involving monomer-polymer domains in single crystals. We reveal that the speed of photomechanical bending induced by the polymerization reaction in this example is comparable to those of the well-known diarylethene derivatives, in which electrocyclic ring-closing and ring-opening reactions operate. Furthermore, we characterize the distinct mechanical properties of the monomer and polymer using a quantitative nanoindentation technique as well as demonstrate photopatterning on a monomer-coated paper for potential use in security devices. These crystals with several advantages, such as photomechanical bending (weight lifting) even when the crystal size is large, responsiveness to both UV and visible light, distinct solubilities (the polymer is insoluble, whereas the monomer is soluble in most organic solvents) and colors, provide unique opportunities for their use at different length scales of the sample (μm to mm) for various purposes.

Improving Photosensitivity without Changing Thermal Reactivity in Photochromic Diarylbenzenes Based on Accurate Prediction by DFT Calculations

Daichi KITAGAWA, Naoko TAKAHASHI, Tatsumoto NAKAHAMA, Seiya KOBATAKE *Photochem. Photobiol. Sci.*, Vol. 19(5), pp. 644-653 (2020).

1,2-Diarylbenzenes (DABs) have been developed as a new family of fast T-type photochromic switches. However, the molecular design strategy for DABs with desired optical and thermal properties is not established. In this work, we explored the best functional in quantum chemical calculations to predict the properties of DABs. Furthermore, we newly designed and synthesized DABs based on the calculation using the best functional, resulting in the improvement of the photosensitivity in the UV-A region (i.e. a shift of absorption to lower energies and an increase in the absorption coefficient) without changing the thermal back-reaction rate.

Enhancement of Coloring under Ultraviolet Irradiation in Photochromic Diarylbenzenes

Shota HAMATANI, Daichi KITAGAWA, Tatsumoto NAKAHAMA, Seiya KOBATAKE

Tetrahedron Lett., Vol. 61(24), Article No. 151968 (5 pages) (2020).

1,2-Diarylbenzenes have been developed as a new family of T-type photochromic switches that have potential applications such as ophthalmic lenses, real-time holography, and super-resolution microscopy. In this work, we have designed and synthesized novel diarylbenzenes bearing thiazole and oxazole rings as the aryl groups to improve the coloring under ultraviolet (UV) irradiation. The substitution of the aryl groups with thiazole and oxazole rings having lower aromaticity than thiophene brought about the deceleration of the thermal bleaching reaction, the blue-shift of the absorption spectra of the closed-ring isomers, and the increase of the photocyclization reactivity, which results in the enhancement of the coloring when exposed to UV light. The results would provide useful information for the development of practical applications using diarylbenzene chromophores.

Photoreversible Birefringence Change of Diarylethene Single Crystals as Revealed by Change in Molecular Polarizability Anisotropy

Kohei MORIMOTO, Hajime TSUJIOKA, Daichi KITAGAWA, Seiya KOBATAKE

J. Phys. Chem. A, Vol. 124(23), pp. 4732-4741 (2020).

Stimuli-responsive organic crystals represent a new frontier of material chemistry. Recently, we have reported photoreversible interference color change to multicolor in single crystals composed of a photochromic diarylethene derivative, 1,2-bis(2-ethyl-5-phenyl-3-thienyl)perfluorocyclopentene (**1a**), accompanied by the photochromic reaction. The origin of the interference color change is due to the photoinduced birefringence change in the photoisomerization of diarylethenes. In this study, we newly found that single crystals composed of 1,2-bis(2,5-dimethyl-3-thienyl)perfluorocyclopentene (**2a**) also exhibit a photoreversible interference color change. The birefringence value for crystal **2a** increased with the photocyclization conversion, while that for crystal **1a** decreased. The relationship between the photoinduced birefringence changes for crystals **1a** and **2a** and their molecular structures was discussed based on the change in the molecular polarizability anisotropy accompanied by the photochromic reaction. These results would provide not only new opportunities for the application of photochromic crystals but also useful strategies for the design of crystalline materials that exhibit the desired birefringence change.

Nanosecond Laser Photothermal Effect-Triggered Amplification of Photochromic Reactions in Diarylethene Nanoparticles

Yukihide ISHIBASHI, Shoki NAKAI, Keisuke MASUDA, Daichi KITAGAWA, Seiya KOBATAKE, Tsuyoshi ASAH

Chem. Commun., Vol. 56(52), pp. 7088-7091 (2020).

Intense nanosecond 532-nm pulse laser excitation to aqueous nanoparticle colloids of a photochromic diarylethene induced drastic amplification of the cycloreversion reaction yield depending on a laser fluence of 1 to 37 mJ cm⁻² pulse⁻¹. The conversion from the closed-ring form to the open-ring form by a single-shot nanosecond pulse showed the third-order increase against the laser fluence. The enhancement of the cycloreversion quantum yield was discussed in terms of the transient laser heating of the nanoparticle in a nanosecond time scale. We propose the nanoscale laser heating model where ultrafast photothermal conversion enhances the cycloreversion reaction of molecules neighbouring an excited one. For this model, an intense nanosecond-laser pulse plays two roles; one is to heat the nanoparticle composed of the closed-ring form quickly and the second is to induce the cycloreversion reaction in the “hot” nanoparticle keeping the temperature high during the nanosecond laser pulse. Consequently, a photosynergetic interaction between multi-chromophore and multi-photon is indispensable for the drastic enhancement of the cycloreversion reaction of the nanoparticle composed of the closed-ring form. Thus, the mechanism was explained as a ‘photosynergetic response’ coupled with nanoscale laser heating and the photochemical reaction in nanoparticles.

Geometrical Evolution and Formation of the Photoproduct in the Cycloreversion Reaction of a Diarylethene Derivative Probed with Molecular Vibrations

Hikaru SOTOME, Hajime OKAJIMA, Tatsuhiko NAGASAKA, Yuka TACHII, Akira SAKAMOTO, Seiya KOBATAKE, Masahiro IRIE, Hiroshi MIYASAKA

ChemPhysChem, Vol. 21(14), pp. 1524-1530 (2020).

The geometrical evolution of the reactant and formation of the photoproduct in the cycloreversion reaction of a diarylethene derivative were probed using time-resolved absorption spectroscopies in the visible to near-infrared and mid-infrared regions. The time-domain vibrational data in the visible region show that the initially formed Franck-Condon state is geometrically relaxed into the minimum in the excited state potential

energy surface, concomitantly with the low-frequency coherent vibrations. Theoretical calculations indicate that the nuclear displacement in this coherent vibration is nearly parallel to that in the geometrical relaxation. Time-resolved mid-infrared spectroscopy directly detected the formation of the open-ring isomer with the same time constant as the decrease of the closed-ring isomer in the excited state minimum. This observation reveals that no detectable intermediate, in which the population is accumulated, is present between the excited closed-ring isomer and the open-ring isomer in the ground state.

Photoluminescence ON/OFF Switching of a Single Colloidal Quantum Dot Using Photochromic Diarylethene

Nanoka YANO, Mitsuaki YAMAUCHI, Daichi KITAGAWA, Seiya KOBATAKE, Sadahiro MASUO

J. Phys. Chem. C, Vol. 124(31), pp. 17423-17429 (2020).

Photoluminescence (PL) on/off switching systems using photochromic molecules have a high potential for a wide range of applications, such as optical memories, chemo- and biosensing, and super-resolution microscopy. The combination of diarylethene derivatives (DAEs) and colloidal semiconductor quantum dots (QDs) is the most promising candidate system. The PL on/off switching behavior of the systems has been observed in ensemble solutions. In this work, we investigated the PL on/off switching behavior of CdSe/ZnS core/shell QDs at the single QD level by dispersing the QDs and DAEs in a poly(methyl methacrylate) thin film. The photoswitching behavior of the PL intensity and the lifetime of single QDs accompanied by the photoisomerization of the DAE were successfully observed based on Förster-type fluorescence resonance energy transfer (FRET) from the excited QDs to the closed-ring form of the DAEs. By controlling the concentration of DAEs and the photoirradiation time for the photoisomerization of DAEs, average FRET efficiency of approximately 80% was achieved. However, a completely reversible photoswitching was difficult to achieve. Based on the PL lifetime change of the single QDs with the photoisomerization of DAEs, details of the system are discussed. The present results provide important insights into creating PL on/off switching systems using a single QD and photochromic molecules.

Symmetry Breaking and Photomechanical Behavior of Photochromic Organic Crystals

Daichi KITAGAWA, Christopher J. Bardeen, Seiya KOBATAKE

Symmetry, Vol. 12(9), Article No. 1478 (16 pages) (2020).

Photomechanical materials exhibit mechanical motion in response to light as an external stimulus. They have attracted much attention because they can convert light energy directly to mechanical energy, and their motions can be controlled without any physical contact. This review paper introduces the photomechanical motions of photoresponsive molecular crystals, especially bending and twisting behaviors, from the viewpoint of symmetry breaking. The bending (right-left symmetry breaking) and twisting (chiral symmetry breaking) of photomechanical crystals are based on both intrinsic and extrinsic factors like molecular orientation in the crystal and illumination conditions. The ability to design and control this symmetry breaking will be vital for generating new science and new technological applications for organic crystalline materials.

Photomechanical Behavior of Photochromic Diarylethene Crystals, Chapter 1

Seiya KOBATAKE, Daichi KITAGAWA

Mechanically Responsive Materials for Soft Robotics, Ed.: H. Koshima, Wiley-VCH Verlag, pp. 3-28 (2020).

Photochromic compounds undergo photoreversible transformation reactions between two isomers having different absorption spectra. Diarylethene derivatives exhibit photochromism even in the crystalline phase. Photochromic crystals may be potentially useful for optoelectronic devices, such as optical memories, photoswitchable color filters, photoswitchable polarizers, and photomechanical actuators. This chapter focuses on recent development of photomechanical behavior of photochromic diarylethene crystals, as crystal deformation, bending, twisting, and breaking.

Solid-State Fluorescence Switching Using Photochromic Diarylethenes, Chapter 15

Seiya KOBATAKE, Tatsumoto NAKAHAMA

Advances in Organic Crystal Chemistry, Comprehensive Reviews 2020, Eds.: M. Sakamoto, H. Uekusa, Springer, Singapore, pp. 299-323 (2020)

Solid-state fluorescence-switchable materials that show large changes in fluorescence intensities and/or colors in response to various external stimuli have attracted much attention in various applications, such as optical memories, display devices, and sensor materials. In particular, fluorescence switching using photochromic diarylethenes has been widely investigated because of the excellent performance of diarylethene with high thermal stabilities, high fatigue-resistant properties, and high reactivity in the solid states. Although many

researchers investigated the fluorescence switching properties only in solution, the evaluation in solid states is essential for the practical applications. This chapter has focused on solid-state fluorescence switching behavior using diarylethene and reviewed the rational design and the properties for various types of the fluorescence-switchable materials.

Photoresponsive Molecular Crystals for Light-Driven Photoactuators, Chapter 25

Seiya KOBATAKE, Daichi KITAGAWA

Photosynergetic Responses in Molecules and Molecular Aggregates, Eds.: H. Miyasaka, K. Matsuda, J. Abe, T. Kawai, Springer, Singapore, pp. 427-447 (2020)

Various types of photomechanical motion have drawn much attention because there is a potential to create photomechanical actuators from molecular-scale to macro-scale. To construct photoactuators, it is necessary to utilize a molecular assembly with a small free volume. Photochromic compounds undergo photoreversible isomerization between the original colorless isomer and the photo-generated colored isomer upon alternating irradiation with UV and visible light. Among many known photochromic compounds, diarylethenes undergo photochromic reactions even in the crystalline phase. The present review introduces recent development in the study of photomechanical crystals including crystal shape changes, bending velocity, dependence of the bending behavior on irradiation wavelength, the behavior in mixed crystal, new types of photomechanical motion, and applications. These photomechanical behaviors are based on geometrical structure changes in the crystalline phase and can be applied to macro-sized light-driven photoactuators.

Treatment of Wastewater Containing Persistent Organic Pollutants by Catalytic Hydrothermal Oxidation Method

Noritsugu KOMETANI

Catalysts and Catalysis, Vol. 62, No. 3, p. 173-177 (2020)

Degradation of persistent organic pollutants contained in wastewater can be substantially facilitated using copper-based materials as a catalyst for catalytic hydrothermal oxidation. The mechanism has been attributed to the dramatic acceleration of Fenton-like reaction by copper ion under the hydrothermal condition. Copper-nickel binary catalyst has been recently found to show a higher catalytic action.

Development of Advanced Wastewater Treatment Technique by Hydrothermal Oxidation Method

Noritsugu KOMETANI

Newletter of the Technical Association of Photopolymers, Vol. 90, p. 7-9 (2020)

Chemically Crosslinked Bispecific Antibodies for Cancer Therapy: Breaking from the Structural Restrictions of the Genetic Fusion Approach

Asami UEDA, Mitsuo UMETSU, Takeshi NAKANISHI, Kentaro HASHIKAMI, Hikaru NAKAZAWA, Shuhei HATTORI, Ryutaro ASANO, Izumi KUMAGAI

Int. J. Mol. Sci., Vol. 21, Article No. 711 (15 pages) (2020)

Antibodies are composed of structurally and functionally independent domains that can be used as building blocks to construct different types of chimeric protein-format molecules. However, the generally used genetic fusion and chemical approaches restrict the types of structures that can be formed and do not give an ideal degree of homogeneity. In this study, we combined mutation techniques with chemical conjugation to construct a variety of homogeneous bivalent and bispecific antibodies. First, building modules without lysine residues—which can be chemical conjugation sites—were generated by means of genetic mutation. Specific mutated residues in the lysine-free modules were then re-mutated to lysine residues. Chemical conjugation at the recovered lysine sites enabled the construction of homogeneous bivalent and bispecific antibodies from block modules that could not have been so arranged by genetic fusion approaches. Molecular evolution and bioinformatics techniques assisted in finding viable alternatives to the lysine residues that did not deactivate the block modules. Multiple candidates for re-mutation positions offer a wide variety of possible steric arrangements of block modules, and appropriate linkages between block modules can generate highly bioactive bispecific antibodies. Here, we propose the effectiveness of the lysine-free block module design for site-specific chemical conjugation to form a variety of types of homogeneous chimeric protein-format molecule with a finely tuned structure and function.

Turn-on fluorescence and photodynamic activity of β -(1,3-1,6)-D-glucan-complexed porphyrin derivative inside HeLa cells

Shodai HINO, Rikushi FUNADA, Kouta SUGIKAWA, Kazuya KOUMOTO, Toshio SUZUKI, Takeshi

NAGASAKI, Atsushi IKEDA

Photochem. Photobiol. Sci., Vol.18, pp. 2854-2858 (2019).

Fluorescence intensities of water-soluble β -(1,3-1,6)-D-glucan (β -1,3-glucan)-complexed porphyrin derivatives were very weak as a result of self-quenching. However, β -1,3-glucan-complexed tetra (aminophenyl)porphyrin exhibited 'off-state' to 'on-state' fluorescence switching activity by intracellular uptake. Furthermore, the internalised complex showed a high level of photodynamic activity toward HeLa cells under photoirradiation at long wavelengths.

Improved Stability and Photodynamic Activity of Water-Soluble 5,15-Diazaporphyrins Incorporated in β -(1,3-1,6)-D-Glucan with On-Off Switch

Shodai HINO, Shuhei SATAKE, Hideyuki SHINMORI, Kouta SUGIKAWA, Riku KAWASAKI, Kazuya KOUMOTO, Toshio SUZUKI, Takeshi NAGASAKI, Atsushi IKEDA

Chemistry-An Asian Journal., Vol.15, pp. 365-370 (2020).

5,15-Diazaporphyrins, which have a large absorption at wavelengths over 600 nm, were dissolved in water by complex formation with β -(1,3-1,6)-D-glucans. Aqueous solutions of these complexes were relatively stable compared with their trimethyl- β -cyclodextrin-complexed analogues. β -Glucan-complexed diazaporphyrins showed quenched fluorescence and had low singlet-oxygen-generation abilities owing to random self-aggregation. However, external stimuli, such as the presence of liposomes or intra-cellular uptake, restored the fluorescence and singlet-oxygen-generation abilities of β -glucan-complexed diazaporphyrins. Consequently, β -glucan-complexed diazaporphyrins showed very high photodynamic activities toward HeLa cells.

Mechanism Toward Turn-on of Polysaccharide-Porphyrin Complexes for Fluorescence Probes and Photosensitizers in Photodynamic Therapy in Living Cells

Shodai HINO, Rikushi FUNADA, Kouta SUGIKAWA, Riku KAWASAKI, Kazuya KOUMOTO, Toshio SUZUKI, Takeshi NAGASAKI, Atsushi IKEDA

ChemMedChem, in press.

β -(1,3-1,6)-D-Glucan, λ -carrageenan, tamarind gum, and pullulan can dissolve various porphyrin derivatives via the formation of complexes in water using a high-speed vibration milling method. The aqueous solutions of the resulting complexes exhibit long-term stability. Despite the adverse effects of the self-quenching process, notable fluorescence and improved photodynamic activity of the polysaccharide-complexed porphyrin derivatives were observed in the presence of liposomes, micelles, cyclodextrins, and HeLa cells. It was noted that the type of porphyrins was more important than the type of polysaccharides present in the complex. Porphyrin self-aggregates were monodispersed in the lipid membranes of the liposomes and lysosomes. The polysaccharide-complexed porphyrin derivatives showed increased photodynamic activity toward HeLa cells under photoirradiation between 610 and 740 nm.

Preparation and Characterization of a Novel Bispecific Antibody That Targets Her2 and BSH for Boron Neutron Capture Therapy

Taisei KANAI, Taro TACHIBANA, Takeshi NAKANISHI, Takeshi NAGASAKI, Mitsunori Kiriata, Yoshihide HATTORI, Yu SANADA, Yoshinori SAKURAI, Shin-ichiro MASUNAGA

KURNS Progress Report 2019, in press.

Construction of a Circularly Connected VHH Bispecific Antibody (Cyclobody) for the Desirable Positioning of Antigen-Binding Sites

Saki HEMMI, Ryutaro ASANO, Kouki KIMURA, Mitsuo UMETSU, Takeshi NAKANISHI, Izumi KUMAGAI, Koki MAKABE

Biochem. Biophys. Res. Commun., Vol. 523, pp. 72-77 (2020)

A bispecific antibody (bsAb) is an emerging class of next-generation biological therapeutics. BsAbs are engineered antibodies possessing dual antigen-binding paratopes in one molecule. The circular backbone topology has never been demonstrated, although an enormous number of bispecific constructs have been proposed. The circular topology is potentially beneficial for fixing the orientation of two paratopes and protection from exopeptidase digestion. We construct herein a circularly connected bispecific VHH, termed cyclobody, using the split-intein circular ligation of peptides and proteins. The constructed cyclobodies are protected from proteolysis with a retained bispecificity. The anti-EGFR \times anti-GFP cyclobody can specifically stain EGFR-positive cells with GFP. The anti-EGFR \times anti-CD16 cyclobody shows cytotoxic activity against EGFR-positive cancer cells with comparative activity of a tandem VHH construct. Successful demonstration

of a new topology for the bispecific antibody will expand the construction strategy for developing antibody-based drugs and reagents.

Build-Up Functionalization of Anti-EGFR × Anti-CD3 Bispecific Diabodies by Integrating High-Affinity Mutants and Functional Molecular Formats

Ryutaro ASANO, Katsuhiro HOSOKAWA, Shintaro TAKI, Shota KONNO, Ippei SHIMOMURA, Hiromi OGATA, Mai OKADA, Kyoko ARAI, Masayoshi ONITSUKA, Takeshi OMASA, Takeshi NAKANISHI, Mitsuo UMETSU, Izumi KUMAGAI

Sci. Rep., Vol. 10, Article No. 4913 (8 pages) (2020)

Designing non-natural antibody formats is a practical method for developing highly functional next-generation antibody drugs, particularly for improving the therapeutic efficacy of cancer treatments. One approach is constructing bispecific antibodies (bsAbs). We previously reported a functional humanized bispecific diabody (bsDb) that targeted epidermal growth factor receptor and CD3 (hEx3-Db). We enhanced its cytotoxicity by constructing an Fc fusion protein and rearranging order of the V domain. In this study, we created an additional functional bsAb, by integrating the molecular formats of bsAb and high-affinity mutants previously isolated by phage display in the form of Fv. Introducing the high-affinity mutations into bsDbs successfully increased their affinities and enhanced their cytotoxicity in vitro and in vivo. However, there were some limitations to affinity maturation of bsDb by integrating high-affinity Fv mutants, particularly in Fc-fused bsDb with intrinsic high affinity, because of their bivalency. The tetramers fractionated from the bsDb mutant exhibited the highest in vitro growth inhibition among the small bsAbs and was comparable to the in vivo anti-tumor effects of Fc-fused bsDbs. This molecule shows cost-efficient bacterial production and high therapeutic potential.

Identification of yeast-derived emulsification proteins through analyses of proteins distributed into the emulsified phase

Masaya ONISHI, Mana UEDA, Daiki SAITO, Mao TAKATA, Yoshihiro OJIMA, Masayuki AZUMA

Food Hydrocoll., in press (2020)

Emulsifiers are widely used in food manufacturing, and cell wall mannoproteins from *Saccharomyces cerevisiae*, a representative food yeast, have been proposed as potential new emulsifiers. However, their use has not become widespread. One reason is that the protein responsible for emulsification has not been identified so no efficient preparation method has been established. In this study, the emulsification substances were identified. Many mannoproteins are fixed to the cell wall via a glycosylphosphatidylinositol (GPI) anchor. Because emulsifying activity was found in the culture supernatant (CS) in *gup1Δ* with a mutation of GPI anchor synthesis, a protein distributed from the CS into the emulsified phase by emulsification treatment was analyzed. Using mass spectrometry, it was identified to be Gas1, a mannoprotein localized to the cell wall via a GPI anchor. Further, recombinant Gas1 without a C-terminal GPI anchor binding signal was purified, and it showed activity similar to bovine serum albumin, a well-known protein emulsifier. Gas1 also retained its activity under a wide range of pH and high salt conditions. *Saccharomyces cerevisiae* has Gas3 and Gas5, proteins homologous to Gas1, and recombinant Gas3 and Gas5 without the C-terminal signal were also purified and found to have emulsifying activity similar to that of recombinant Gas1. These results strongly suggest that Gas proteins take part in the emulsifying activity of yeast mannoproteins. It was also demonstrated that emulsification proteins could be identified by analyzing proteins distributed in an emulsified phase, so this method will be effective in finding new emulsification proteins.

Enhanced floc formation by degP-deficient Escherichia coli cells in the presence of glycerol

Yoshihiro OJIMA, Hiroaki HONMA, Mio OTSUKA, Satsuki MATANO, Masayuki AZUMA

J. Biosci. Bioeng., in press (2020)

Floc formation is an aggregation phenomenon of microbial cells in which the cells form flocs. In this study, it was found that addition of glycerol to a complex glucose medium promoted spontaneous floc formation by an *Escherichia coli degP*-deficient mutant strain ($\Delta degP$) in a dose-dependent manner. In the presence of 10% (v/v) glycerol, the amount of floc formation (quantified as floc protein) reached its maximum value (230 mg/L), five times that in its absence. 10% (v/v) glycerol was the limit concentration that does not inhibit cell growth of $\Delta degP$ strain. Glycerol was not consumed by $\Delta degP$ cells during floc formation. To provide media having nearly the same viscosity as that containing 10% (v/v) glycerol, carboxymethyl cellulose (CMC) or polyvinylpyrrolidone (PVP) were added to medium as viscosifying agents. Floc formation was not promoted by increasing the medium viscosity with CMC or PVP. However, addition of ethylene glycol also significantly promoted floc formation in the same manner as glycerol. Addition of short-chain polyols decreased the number of viable $\Delta degP$ cells in the floc structure and enhanced outer membrane vesicle (OMV) production by $\Delta degP$

cells; polyols-induced damage of outer membrane in *ΔdegP* cells may contribute to the promoted floc formation.

Mineralization induced by phosphorylated dry baker's yeast

Yoshihiro OJIMA, Maya KIHARA, Mami YOSHIDA, Koichi IGARASHI, Tomoko YOSHIDA, Masayuki AZUMA

PLOS ONE, Vol.15, No. 9, p. e0239774 (2020)

We found the mineralization of Cu during long-term Cu^{2+} adsorption onto dry baker's yeast cells phosphorylated using sodium cyclo-triphosphate. Field emission scanning electron microscopy (FESEM) with energy-dispersive X-ray spectroscopy confirmed that the elemental composition of minerals were copper, phosphorus, and oxygen. Synchrotron-based X-ray absorption fine structure showed that the local structure around Cu atoms deposited on the mineral was almost identical to that of commercial copper (II) phosphate $\text{Cu}_3(\text{PO}_4)_2 \cdot 3\text{H}_2\text{O}$. However, the crystallinity was low, and the structure was slightly distorted. Time profile analysis using FESEM revealed that copper phosphate mineralization was first apparent on Day 3 of adsorption, whereas mineral formation plateaued at around Day 7. It seems that mineralization occurs by the local saturation of phosphate and Cu^{2+} on the yeast cells. Mineralization of the rare earth ion Dy^{3+} was also demonstrated during long-term adsorption. Mineralization on phosphorylated yeast cells appears to follow a common path for various types of metal ions and provides a promising technique for metal recovery via irreversible adsorption.

Cell surface changes that advance the application of using yeast as a food emulsifier

Shinsuke NEROME, Masaya ONISHI, Daiki SAITO, Ayano MIZOBUCHI, Tatsuya ANDO, Yui DAIRA, Azusa MATSUMOTO, Yoshihiro OJIMA, Masayuki AZUMA

Food Chem., Vol. 315, p. 126264 (2020)

A previous study revealed that *Saccharomyces cerevisiae mcd4Δ*, a cell wall mutant with a defect in the synthesis of the glycosylphosphatidylinositol anchor, has a strong macrophage activation ability. In this study, remarkable emulsion formation after cell suspensions of *mcd4Δ* and *anp1Δ* (which exhibit an extreme reduction of mannan) were mixed with oil was found. Moreover, the relationship between cell wall mutation and emulsion formation was investigated, suggesting that *och1Δ* with a defect in the formation of N-linked glycans also had a strong emulsification ability and that high molecular weight materials released from the cells were involved in emulsion formation. Furthermore, two strains (*asc1Δ* and *scp160Δ*) with a strong emulsification ability without a large decrease in mannan content were also found from the wide screening of strains that exhibit an emulsifying activity using more than 5,000 gene-deficient strains. These results provide valuable information for the development of a yeast-derived emulsifier.

Construction of hypervesiculation Escherichia coli strains and application for secretory protein production

Yoshihiro OJIMA, Tomomi SAWABE, Katsuya KONAMI, Masayuki AZUMA

Biotechnol. Bioeng., Vol. 117, No. 3, pp. 701-709 (2020)

Outer membrane vesicles (OMVs) are extracellular vesicles released from the surface of Gram-negative bacteria, including *Escherichia coli*. Several gene-deficient mutants relating to envelope stress (*nlpI* and *degP*) and phospholipid accumulation in the outer leaflet of the outer membrane (*miaA* and *miaE*) increase OMV production. This study examined the combinatorial deletion of these genes in *E. coli* and its effect on OMV production. The *nlpI* and *miaE* double-gene-knockout mutant (*ΔmiaEΔnlpI*) showed the highest OMV production. Sodium dodecyl sulfate–polyacrylamide gel electrophoresis-based quantitative analysis showed that OMV production by strain *ΔmiaEΔnlpI* was ~30 times that by the wild-type. In addition, to evaluate the protein secretion capacity of OMVs, green fluorescent protein (GFP) fused with outer membrane protein W (OmpW) was expressed in OMVs. Western blot analysis showed that GFP secretion through OMVs reached 3.3 mg/L in the culture medium of strain *ΔmiaEΔnlpI /gfp*, 500 times that for the wild-type. Our approach using OMVs for extracellular protein secretion in *E. coli* is an entirely new concept compared with existing secretion systems.

Chromatin-bound CRM1 recruits SET-Nup214 and NPM1c onto HOX clusters causing aberrant HOX expression in leukemia cells

Masahiro OKA, Sonoko MURA, Mayumi OTANI, Yoichi MIYAMOTO, Jumpei NOGAMI, Kazumitsu MAEHARA, Akihito HARADA, Taro TACHIBANA, Yoshihiro YONEDA, Yasuyuki OHKAWA

Elife 8:e46667. doi: 10.7554/eLife.46667. (2019)

We previously demonstrated that CRM1, a major nuclear export factor, accumulates at *Hox* cluster regions to recruit nucleoporin-fusion protein Nup98HoxA9, resulting in robust activation of *Hox* genes (Oka et al., 2016). However, whether this phenomenon is general to other leukemogenic proteins remains unknown. Here, we show that two other leukemogenic proteins, nucleoporin-fusion SET-Nup214 and the NPM1 mutant, NPM1c, which contains a nuclear export signal (NES) at its C-terminus and is one of the most frequent mutations in acute myeloid leukemia, are recruited to the *HOX* cluster region via chromatin-bound CRM1, leading to *HOX* gene activation in human leukemia cells. Furthermore, we demonstrate that this mechanism is highly sensitive to a CRM1 inhibitor in leukemia cell line. Together, these findings indicate that CRM1 acts as a key molecule that connects leukemogenic proteins to aberrant *HOX* gene regulation either via nucleoporin-CRM1 interaction (for SET-Nup214) or NES-CRM1 interaction (for NPM1c).

Detection of Rhizopus-specific antigen in human and murine serum and bronchoalveolar lavage.

Wataru SHIBATA, Mamiko NIKI, Kanako SATO, Hiroki FUJIMOTO, Koichi YAMADA, Watanabe Tetsuya WATANABE, Miyazaki Yoshitsugu MIYAZAKI, Asai Kazuhisa ASAI, Yoko OBATA, Taro TACHIBANA, Tomoya KAWAGUCHI, Yukihiro KANEKO, Hiroshi KAKEYA.

Med. Mycol. myaa001. doi: 10.1093/mmy/myaa001. (2020)

Mucormycosis is a deep-seated fungal infection that mainly develops in patients with severe immunodeficiencies such as those with malignant hematological diseases. Despite poor prognosis, there is no reliable and minimally invasive diagnostic method-such as serodiagnosis-for making a clinical decision regarding the condition. As early diagnosis and early treatment improve the prognosis of mucormycosis, the development of a sensitive early diagnostic method is important. We had previously identified a *Rhizopus*-specific antigen (RSA) by signal sequence trapping and retrovirus-mediated expression (SST-REX), and evaluated its utility as a diagnostic antigen by constructing a sandwich enzyme-linked immunosorbent assay (ELISA) system to detect serum RSA levels in inoculated mice. In this study, we used the RSA-specific rabbit monoclonal antibodies generated by novel hybridoma technology to improve the sensitivity of the ELISA system. We observed an increase in serum and bronchoalveolar lavage fluid (BALF) levels of RSA in mouse model 1 day after inoculation, suggesting that this newly developed monoclonal antibody-based ELISA system may be useful for the diagnosis of mucormycosis in the early stages of infection. In addition, we measured RSA levels in human serum and BALF, and found that serum RSA level was higher in mucormycosis patients (15.1 ng/ml) than that in invasive pulmonary aspergillosis patients (0.53 ng/ml) and the negative control (0.49 ng/ml). Our results suggest that RSA may be a powerful tool for the diagnosis of pulmonary mucormycosis, and its differentiation from other deep-seated mycoses such as aspergillosis.

PACT/PRKRA and p53 regulate transcriptional activity of DMRT1.

Kazuko FUJITANI, Asako OTOMO, Yuto NAGAYAMA, Taro TACHIBANA, Rika KATO, Yusuke KAWASHIMA, Yoshiro KODERA, Tomoko KATO, Shuji TAKADA, Kei TAMURA, Nobuhiko TAKAMATSU, Michihiko ITO.

Genet. Mol. Biol. 43(2):e20190017. doi: 10.1590/1678-4685-GMB-2019-0017. (2020)

The transcription factor DMRT1 (doublesex and mab-3 related transcription factor) has two distinct functions, somatic-cell masculinization and germ-cell development in some vertebrate species, including mouse and the African clawed frog *Xenopus laevis*. However, its transcriptional regulation remains unclear. We tried to identify DMRT1-interacting proteins from *X. laevis* testes by immunoprecipitation with an anti-DMRT1 antibody and MS/MS analysis, and selected three proteins, including PACT/PRKRA (Interferon-inducible double-stranded RNA dependent protein kinase activator A) derived from testes. Next, we examined the effects of PACT/PRKRA and/or p53 on the transcriptional activity of DMRT1. In transfected 293T cells, PACT/PRKRA and p53 significantly enhanced and repressed DMRT1-driven luciferase activity, respectively. We also observed that the enhanced activity by PACT/PRKRA was strongly attenuated by p53. Moreover, in situ hybridization analysis of PACT/Prkra mRNA in tadpole gonads indicated high expression in female and male germline stem cells. Taken together, these findings suggest that PACT/PRKRA and p53 might positively and negatively regulate the activity of DMRT1, respectively, for germline stem cell fate.

Generation of the Rat Monoclonal Antibody Against the Extracellular Domain of Human CD63 by DNA Immunization.

Liu XU, Kan-Ichiro IHARA, Saori YOSHIMURA, Daijiro KONNO, Akira TACHIBANA, Takeshi NAKANISHI, Taro TACHIBANA.

Monoclon. Antib. Immunodiagn. Immunother. 39(3):74-76. doi: 10.1089/mab.2020.0007. (2020)

Human cluster of differentiation 63 (hCD63) is one of the tetraspanin receptors that is abundant on the surface

of exosomes. Exosomes are involved in cell-to-cell communication, including from cancer cells to normal cells. It is very important to detect exosomes as a marker for the diagnosis of various diseases. In this study, we report the generation and characterization of a monoclonal antibody (mAb) against the extracellular domain of hCD63 using DNA immunization. This mAb, clone 1C8-2B11, exhibits high performance for use in immunofluorescence and flow cytometry, and it has 10-fold higher affinity than the control antibody that is commercially available. mAb 1C8-2B11 has great potential to be a tool for research and clinical diagnosis.

Uniform straw-like cell architecture for three-dimensional cell-cell communication assay

Yusaku INUBUSHI, Yoshiki SAKAGUCHI, Akira TACHIBANA

Biosci. Biotechnol. Biochem. Vol.84, pp.1681-1684. (2020)

We fabricated uniform straw-like cell architecture with central lumen using a suture thread within 1 h. The architecture consisting of cancer cells and mature adipocyte was used for cell-cell communication assay, although mature adipocyte could not form spontaneous multi-cellular spheroids. Using the system, it is possible to investigate three-dimensional cell-cell communication as an alternative to animal experiments.

Improvement of a miRNA inhibitor by intracellular selection

Akira TACHIBANA, Aiko YAMAMOTO

Biosci. Biotechnol. Biochem. Vol.84, pp.1451-1454. (2020)

Sequences surrounding the miRNA binding domain of the miRNA inhibitor LidNA were selected intracellularly. The library was transfected into cells, and then, inhibitors that were associated with argonaute 2 were selected. The potent inhibitors were slowly degraded intracellularly, while the lower-activity inhibitors were rapidly degraded. A combination of the selected sequences surrounding the miRNA binding domain enhanced miRNA inhibitory activity.

Structural improvement of LidNA: delta-type LidNA is a potent miRNA inhibitor constructed with unmodified DNA

Akira TACHIBANA, Yoshiki KOMEDA, Aiko YAMAMOTO

Biosci. Biotechnol. Biochem. Vol.84, pp. 1168-1175. (2020)

Many miRNA inhibitors have been developed, including chemically modified oligonucleotides, such as 2'-O-methylated RNA and locked nucleic acid (LNA). Unmodified DNA has not yet been reported as a miRNA inhibitor due to relatively low DNA/miRNA binding affinity. We designed a structured DNA, LidNA, which was constructed with unmodified DNA, consisting of a complementary sequence to the target miRNA flanked by two structured DNA regions, such as double-stranded DNA. LidNA inhibited miRNA activity more potently than 2'-O-methylated RNA or LNA. To optimize LidNA, two double-stranded regions were joined, causing the molecule to assume a delta-like shape, which we termed delta-type LidNA. Delta-type LidNAs were developed to target endogenous and exogenous miRNAs, and exhibited potent miRNA inhibitory effects with a duration of at least 10 days. Delta-type LidNA-21, which targeted miR-21, inhibited the growth of cancer cell lines. This newly developed LidNA could contribute to miRNA studies across multiple fields.

LidNA, a miRNA inhibitor constructed with unmodified DNA, requires an xxxA insertion sequence in miRNA binding site for its potent inhibitory activity

Akira TACHIBANA, Satoshi SAITO, Yukiko FUJIYAMA, Toshizumi TANABE

FEBS Lett. Vol.594, pp.1608-1614. (2020)

The involvement of miRNAs in the pathogenesis of various diseases, including cancer, poses the need for developing miRNA inhibitors. Previously, using unmodified DNA, we designed LidNA, which inhibited miRNA function more potently than 2'-O-methylated RNA and locked nucleic acid. LidNA consists of a complementary sequence to miRNA flanked by two structured DNAs. Alterations in the connected sequences between the complementary region and structured region modestly affect miRNA inhibition activity. Surprisingly, variations in the mismatched insertion sequence in the center of the complementary sequence significantly affect activity. The central insertion sequence xxxA is required for the potent miRNA inhibitory effects of LidNA. This suggests that both the structure and insertion sequence of LidNA and other miRNA inhibitors should be considered for maximal miRNA inhibitory activity.

Improved cancer inhibition by miR-143 with a longer passenger strand than natural miR-143

Hiroyuki IDA, Toshizumi TANABE, Akira TACHIBANA

Biochem. Biophys. Res. Commun. Vol.524, pp.810-815. (2020)

We improved miR-143, which inhibits the growth of cancer cells, by the replacement of the passenger strand.

As a result, new miR-143 variants were developed with a single mismatch at the 4th position from the 3'-terminal of the guide strand and an RNA passenger strand with a G-rich flanking DNA region. A reporter gene assay showed that the 80% inhibitory concentration of the new miR-143, long miR-143, was 69 pM, which was three times lower than that of natural miR-143. Long miR-143 inhibited the growth of two cancer cell lines, HeLa-S3 and MIA PaCa-2, more effectively than natural miR-143. This method could be applied to other miRNA families and should be useful for the development of miRNA drugs.

Uniform spheroid formation on a laboratory-made, low cell attachment surface consisting of a chitin sheet

Yusaku INUBUSHI, Akira TACHIBANA

Biosci. Biotechnol. Biochem. Vol.84, pp.997-1000. (2020)

We utilized the reaction of chitosan with acetic anhydride to form a chitin gel. This gel was then dried, which formed a chitin sheet. The procedure was extremely easy for a biologist unfamiliar with materials engineering. Spheroids derived from HEK293T cells were formed on the chitin sheet, because the spheroids slightly attached and slowly moved on the chitin sheet.

Fluorescein isothiocyanate and blue light irradiation alter cell-adhesiveness of cross-linked albumin films for cell patterning

Akira TACHIBANA, Atsuko IIDA, Toshizumi TANABE

Biosci. Biotechnol. Biochem. Vol.84, pp.800-803. (2020)

Cross-linked albumin films, which are non-cell adhesive, were altered to be cell-adhesive by the combination of varied concentrations of fluorescein isothiocyanate and blue light irradiation. In this system, cell patterning was developed with two different cell lines by sequential seeding.

Chitin degradation enzyme-responsive system for controlled release of fibroblast growth factor-2

Akira TACHIBANA, Dai YASUMA, Ryo TAKAHASHI, Toshizumi TANABE

J. Biosci. Bioeng. Vol.129, pp.116-120. (2020)

Chitin is widely found in fungal cell walls and arthropod exoskeletons, and is used as a biomedical material. However, chitin is not water-soluble, restricting its use for controlled release materials. We found that water-soluble chitosan can be acetylated to produce a chitin equivalent, or chitin gel. Chitin gel, produced by mixing chitosan solution with acetic anhydride, can be degraded by lysozyme and fetal bovine serum, so could provide an ideal means for controlled release in biological systems. We tested a combination of chitin gel with a chitin binding domain (CBD) fusion protein as a controlled release system regulated by chitin degradation. A fusion protein consisting of fibroblast growth factor 2 (FGF-2) fused to CBD bound the chitin gel, and was released time-dependently rather than as an initial burst during lysozyme degradation, suggesting that this system could provide a means for controlled drug release in biological systems. Contrastingly, the trinitrophenyl residue (TNP-X) covalently bound to chitin gel, and was released by lysozyme degradation with an initial burst. If release of CBD-FGF-2 were simply dependent on lysozyme degradation of the chitin gel, the release behavior of CBD-FGF-2 would be similar to that of TNP-X, with an initial burst. Therefore, we propose that CBD-FGF-2 repeats the cycle of binding, release, and re-binding to the chitin gel during degradation. This system allows for a time-dependent, controlled release of CBD-FGF-2 without an initial burst.

Architecture and Building Engineering

COUPLING EFFECT OF NODAL DEVIATION AND MEMBER IMPERFECTION ON LOAD-CARRYING CAPACITY OF SINGLE-LAYER RETICULATED SHELL

Huijun LI, Yoshiya TANIGUCHI

International Journal of Steel Structures (2020) 20(3):919–930

Single-layer reticulated shell is sensitive to imperfections. To clarify the effect of member imperfection, nodal deviation and their couplings on load-carrying capacity of reticulated shell, the equivalent load method (ELM) is developed in the present study to establish single-layer reticulated shell with random member imperfection, and its realization procedures in FEM package are well-elaborated. The main conclusions are summarized as follows: the proposed ELM is of high efficiency to form member imperfection in space structures. For reticulated shell only with member imperfection, the limit load is more or less influenced by member imperfection. With the increase of amplitude of member bow imperfection, limit load gradually decreases. Load-carrying capacity of reticulated shell with larger amplitude of bowed member is more sensitive to bending direction of bowed member than the one with smaller amplitude. Load-carrying capacity of the reticulated shell considered is extremely sensitive to nodal deviation. For reticulated shell with nodal deviation and member imperfection, the effect of member imperfection on load-carrying capacity is closely related to the magnitude of nodal deviation. Load-carrying capacity of shell with smaller nodal deviation is obviously affected by member imperfection, while not sensitive to member imperfection for reticulated shell with larger one. Member imperfection can be neglected when nodal deviation is large enough. Load-carrying capacity of reticulated shell is also influenced by bending angle of bowed member. On the whole, load-carrying capacity of reticulated shell with larger amplitude of member imperfection is more sensitive to bending direction than the reticulated shell with smaller one.

EFFECT OF JOINT STIFFNESS AND SIZE ON STABILITY OF THREE-WAY SINGLE-LAYER CYLINDRICAL RETICULAR SHELL

Huijun LI, Yoshiya TANIGUCHI

International Journal of Space Structures, 1-18 (2020)

The main aim of the present article is to study the effect of joint stiffness and joint size on load-carrying capacity of single-layer cylindrical reticular shell. One normalized joint bending stiffness index κ_b and three proposed normalized indexes, that is, normalized joint axial stiffness κ_a , normalized joint shear stiffness κ_s , and normalized joint torsional stiffness κ_t , are used to evaluate the stiffness of joint. Through a large number of numerical computations, the main conclusions are summarized as follows: κ_b has a significant effect on limit load of reticular shell, and this effect has a close relationship to rise-to-span ratio of reticular shell. If κ_b is larger than 30, the joint can be treated as rigid joint. The relationship between the logarithm of κ_b and limit load of reticular shell can be expressed by the logistic formulation. Overall rigidity and load-carrying capacity of reticular shell are greatly influenced by joint axial stiffness. If κ_a is larger than 30, the effect of joint axial stiffness on load-carrying capacity of reticular shell is no longer obvious. Otherwise, the load-carrying capacity will be markedly reduced. The relation between the logarithm of κ_a and limit load of reticular shell can be fitted by the Dose–response formulation. The load-carrying capacity of reticular shell is also influenced by joint torsional stiffness and joint shear stiffness to some extent. The relation between the logarithm of κ_s and limit load can be fitted by the Asymptotic formulation. The effect of joint size on overall rigidity and limit load of reticular shell is evident and cannot be neglected. The limit load gradually decreases with the decrease in joint size, and there is an approximate linear relationship between limit load and joint size.

Cable Arrangement of Ceiling Suspended by Diagonal Cables and its Application to Ceiling with Conventional Method

Kentaro MATSUSHITA, Susumu YOSHINAKA, Yoshiya TANIGUCHI

Proceedings of the 12th Pacific Structural Conference, Tokyo, Japan, November 9-11, ID5-1-3, pp.1-7 (2019)

In this paper, we use a method like ground structure to determine cable arrangement for a ceiling suspended by diagonal cables. We also propose an application method for an existed ceiling with conventional method to reinforce using diagonal cables. We analytically study responses using a ceiling with cables and a ceiling with conventional method under earthquake loading. From obtained results, it was found that responses of a ceilings

with cables was very small. As the reason, a system of a ceiling added with cables does not have specific natural periods because of the material nonlinearity of cables. Consequently, a resonance between earthquake wave and a ceiling does not occur and responses of a ceiling with cables does not depend on the spectrum characteristics of each earthquake wave. As a result, we concluded that cable was superior to brace as a hanging material to resist horizontal vibration.

Summer Sleep Quality and Change of Thermal Environment

Noriko UMEMIYA, Kurumi YAMAGATA, Tomohiro KOBAYASHI

Proceedings of the 13rd HVAC World Congress, 3A-247, (2019)

Relation between bedroom thermal environment change and subjective sleep quality and thermal comfort was surveyed for 63 apartment occupants during midsummer in Osaka. Change of Wet Bulb Globe Temperature (WBGT) of 123 air conditioned and 41 naturally ventilated nights were compared. 1) If bedrooms were air conditioned, sleep quality was better for smaller change of WBGT since the beginning of sleep and faster change of WBGT to constant since the beginning of sleep, 2) If bedrooms were naturally ventilated, a) WBGT increased since the beginning of sleep and decreased toward the end of sleep for higher sleep quality nights. On the other hand, WBGT decreased since the beginning of sleep and increased toward the end of the sleep for lower sleep quality nights. b) WBGT change was smaller for thermally comfortable nights.

Simplified Prediction Method of Vertical Temperature Distribution for Impinging Jet Ventilation System

Tomohiro KOBAYASHI, Toshiya NISHIUMI, Noriko UMEMIYA

Proceedings of the 13rd HVAC World Congress, 5D-468, (2019)

The impinging jet ventilation (IJV) system is an air-distributing strategy to generate a thermal stratification in a room by supplying the air vertically toward the floor, which provides higher ventilation effectiveness than mixing ventilation. To date, however, no simplified prediction model of indoor thermal environment for an impinging jet ventilated room has been established. Therefore, this study aims to propose a simplified calculation model based on "Block Model". This paper first presents a parametric study using Computational Fluid Dynamics (CFD), where total supply airflow rate of a test room is changed as a parameter. The number of terminal is also changed. Secondly, the paper presents the simplified calculation model of vertical temperature distribution based on block model that solves heat flow by advection and diffusion. Here, in this prediction model, the most important parameter is the turbulent thermal diffusivity between two room-space blocks in vertical direction. The room-space blocks are classified into two types, i.e., lower and upper part of a room. Based on parametric study using CFD, turbulent thermal diffusivity is arranged for lower and upper block respectively, and it is finally shown that the vertical temperature distribution from block model well agrees with CFD result.

Difference of Light Environment Evaluation between Elderly and Young People

Noriko UMEMIYA, Wei QUIAO

The 29th Session of the Commission Internationale de l'Eclairage, pp.745-750, (2019)

Light and Dark conditions were evaluated by elderly people and young people in terms of brightness, glare, comfort and preference using experiments with Dark-to-Light and Light-to-Dark sequences. Results indicated the following: 1) Elderly people were less sensitive in terms of brightness to the difference of illuminance change order. 2) Elderly people were less sensitive in terms of glare to the difference of illuminance and to the difference of illuminance change order. 3) The Dark condition was evaluated as less comfortable and less preferred than the Light condition in Light-to-Dark experiments for elderly people, although no difference was found for young people between the Dark and the Light conditions in Light-to-Dark experiments. 4) The Light condition in Dark-to-Light experiments had weaker glare by elderly people than by young people. The Dark condition in Light-to-Dark experiments was evaluated as more comfortable and more preferred by young people than by elderly people.

Pupil Size Change and Light Evaluation of Elderly People

Noriko UMEMIYA, Yasuha KUREYAMA, Mika TOMITA

Proceedings of the 12th Asia Lighting Conference, pp.510-515, (2019)

This study measured pupil size and forehead illuminance simultaneously for elderly people 65 years or older and young university students during corridor walking in daily lighting. Subjective evaluation of the light environment in an experimental room was done for dark and light conditions. Brightness, glare, uniformity, flickering, lighting comfort, lighting preference, and performance were evaluated. Illuminance was 550 lux in

the dark condition and 3300 lux in the light condition. For the elderly and young people, pupil size response to illuminance and the relation of its change to forehead illuminance during walking and subjective light evaluation to dark and light conditions in the experimental room were compared. The gradient of pupil size to forehead illuminance was used as an index of the response. Results show differences in gradients between elderly and young people in lighting preference evaluation of the dark condition and in performance evaluation of the light condition.

A Comparison between Elderly People and Young People in Factors Related to Gazing Characteristics during Walking in Corridors

Mika TOMITA, Noriko UMEMIYA, Yasuha KUREYAMA,
Proceedings of the 12th Asia Lighting Conference, pp.193-200, (2019)

By measuring gazing points of elderly people (65–91) and young people (21–25) as they walked down corridors, this study examined gazing characteristics and their mutual relations, along with physical strength and two-step size. Results clarified the following five points. 1) Among these participants, 64.1% of elderly people and 21.4% of young people had equal to or less than 1.3 two-step size. People with equal to or less than 1.3 two-step size have a higher probability of falling. 2) The frequency distribution of gazing points revealed four groups: G1) 1 area concentration, G2) 2 area concentration, G3) 3 or 4 area concentration, and G4) more than 5 area distribution. 3) The two-step size was worst in G2 and greatest in G3 for elderly people. Therefore, people in G2 tend to fall, but those in G3 do not. Age is unrelated to these results. 4) Gazing characteristics are unrelated to the ease of falling for young people. 5) In G2 of elderly people, someone who is more impervious to glare has a smaller two-step size.

Relation between School Building Configuration and Heat Mitigation Effects of Lawns in Urban Regions

Noriko UMEMIYA, Takeshi KISHIMOTO, Tomohiro KOBAYASHI
Proceedings of the 16th International Building Performance and Simulation Association Conference, p.99-104, (2019)

Using CFD simulation, this study compared heat mitigation effects of partial turf planting in school yards and of overall turf planting. Typical school lots and surrounding buildings were modelled according to actual conditions. Temperature contour lines and air flow vectors on school yards showed that heat mitigation effects are dependent on wind speed and direction. The wet bulb globe temperatures were evaluated and compared. Turf planting in western parts of the school yards was most effective. Heat mitigation at leeward wind areas was slight.

Relationship Between Splashing and Wave Deformation around a Circular cylinder in Front of Vertical Wall

Takehito KAMIKAWA, Takaaki SHIGEMATSU

Journal of Japan Society of Civil Engineers, Ser. B2 (Coastal Engineering), Vol. 75, Issue 2, I_1-I_6 (2019) (in Japanese).

Most of pile-supported piers that have been used in port and harbor in Japan faced to the severe deterioration of slat damage. The purpose of this study is to investigate the conditions of splash occurrence by wave under mild weather in front of the pile-supported pier by carrying out laboratory experiment and numerical calculation. According to the experiment, it is found that there are two patterns of splash occurrence. One of them is that splash occurs on the vertical wall and the other is that at the convergence point of surface waves surrounding the circular cylinder. The calculation results show the potential which OpenFOAM can simulate the wave refraction and convergence and can predict the variation of wave convergence location due to the conditions of waves and pile-supported pier.

On the Effect of Aspect Ratio of Component Member on the Flow Through Porous Media

Yuya WATANABE, Sota NAKAJO, and Takaaki SHIGEMATSU

Journal of Japan Society of Civil Engineers, Ser. B2 (Coastal Engineering), Vol. 75, Issue 2, I_943-I_948 (2019) (in Japanese).

Various models of the porous media flow have been proposed to quantitatively examine the heat and mass transfer inside and around porous media, and the stability of the porous structures. In most studies, porous media components are approximated by spheres. However, natural gravel layers or artificial wave dissipating structures are composed by ellipsoids. Actually, the flow passing through an ellipsoidal porous media is unknown. In this study, we performed numerical simulation to study the microscopic flow in the porous media composed by ellipsoids using an immersed boundary method. Simulation results show that macroscopic pressure drop and fluid force acting on the each component of porous media are influenced by the aspect ratio of ellipsoid.

Practical Formula for Effective Height of Impermeable Hanging Curtain in Steady Water Flow

Masahide TAKEDA, Takaaki SHIGEMATSU, Yoshinosuke KURAHARA, Chisato HARA, Yamato NISHIYAMA

Journal of Japan Society of Civil Engineers, Ser. B3 (Ocean Engineering), Vol. 75, Issue 2, I_409-I_414 (2019) (in Japanese).

This study aims to propose a new prediction formula of the effective height of a hanging curtain in steady water flow. According to the hydraulic experiments and numerical calculations, the more practical calculation formula of the effective curtain height was obtained using the ratio of dynamic pressure and weight and the ratio of the effective curtain height to the curtain length. Our formula is characterized in that the experimental coefficient is without user specification, and the weight is included in the formula, and the parameter using the ratio of the initial curtain height to the water depth is used.

Development of Global Stochastic Tropical Cyclone Model by using large ensemble GCM simulation data(d4PDF)

Jinji UMEDA, Sota NAKAJO, Nobuhito MORI

Journal of Japan Society of Civil Engineers, Ser. B2 (Coastal Engineering), Vol. 75, Issue 2, I_1195-I_1200 (2019) (in Japanese).

A global stochastic tropical cyclone model (GSTM) considering time series correlation of tropical cyclone properties has been developed by using large ensemble GCM simulation data (d4PDF). The bias of d4PDF has been corrected by using the information of the average and the standard deviation of tropical cyclone properties comparing with that of IBTrACS. As a result, we could get accurate correction results at each 3 degree grid. The improvement of the reproducibility of the frequency has been observed at many area by using the joint probability distribution functions (JPDF) of GSTM approximated from the corrected d4PDF data. Especially, this improvement was significant in the area that the tropical cyclone data is insufficient. The simulation results show the variation of the change rate of future tropical cyclone frequency around Japan and the intensification of tropical cyclone depending on the SST scenario.

Pseudo Prediction Experiments of Storm Surge and Waves in 2018 Typhoon Jebi by High Resolution Weather Prediction and Coupled Surge-Wave Model

Nobuhito MORI, Tetsuya TAKEMI, Sooyoul KIM, Yoko SHIBUTANI, Tomohiro YASUDA, Sota NAKAJO, Junichi NINOMIYA, Tomoya SHIMURA

Journal of Japan Society of Civil Engineers, Ser. B2 (Coastal Engineering), Vol. 75, Issue 2, I_283-I_288 (2019)(in Japanese)

Using high-resolution numerical weather prediction model and coupled storm surges and waves, we conducted pseudo-prediction experiments on the maximum wind speed, maximum storm surge height, and maximum wave height for 2018 Typhoon Jebi. The central pressure and maximum wind speed of the typhoon become more accurate as the forecasting time length becomes shorter. The minimum central pressure and maximum wind speed of typhoon at landfall are reasonably estimated 3 days and 2.5 days before the landfall, respectively. In the 4 days length prediction, the peak appearance time of the event is estimated about 12 hours later, but the accuracy is increased as forecast length becomes shorter. The difference of the storm surge height between the prediction and hindcast is less than 0.5 m at the maximum. The reliable prediction of storm surge can be obtained from 2 days ago of landfall, quantitatively.

Hindcast of Storm Surge and Wave by Typhoon Jebi (2018) Using a Parametric Wind and Pressure Model and WRF

Sooyoul KIM, Nobuhito MORI, Tetsuya TAKEMI, Yoko SHIBUTANI, Tomohiro YASUDA, Sota NAKAJO, Tomoya SHIMURA, Junichi NINOMIYA

Journal of Japan Society of Civil Engineers, Ser. B3 (Coastal Engineering), Vol. 75, Issue 2, (2019) , I_277-I_282 (in Japanese).

This study aims to propose a new prediction formula of the effective height of a hanging curtain in steady water flow. According to the hydraulic experiments and numerical calculations, the more practical calculation formula of the effective curtain height was obtained using the ratio of dynamic pressure and weight and the ratio of the effective curtain height to the curtain length. Our formula is characterized in that the experimental coefficient is without user specification, and the weight is included in the formula, and the parameter using the ratio of the initial curtain height to the water depth is used.

Basic Study on the Estimation of Potential of Tropical Cyclone and Storm Surge around Ishigakijima Island

Sota NAKAJO, Hibiku HANAMOTO, Sooyoul KIM

Journal of Japan Society of Civil Engineers, Ser. B3 (Ocean Engineering), Vol. 75, Issue 2, I_67-I_72 (2019) (in Japanese).

The reproducibility of stochastic tropical cyclone model in Ishigaki-jima Island has been examined and showed the good performance. The reproduced typhoon intensity and the storm surge for 5000 years have been estimated from results of the combined stochastic and empirical estimation models. In this area, the tropical cyclones translate toward the north and north-east is severe to the storm surge. However, the substantial risk of the storm surge caused by the tropical cyclone translate toward the north-west is relatively higher.

2018 Typhoon Jebi Post-Event Survey of Coastal Damage in the Kansai Region, Japan

N. MORI, T. YASUDA, T. ARIKAWA, T. KATAOKA, S. NAKAJO, K. SUZUKI, Y. YAMANAKA, A. WEBB

Coastal Engineering Journal, Vol. 61, No. 3, 278 – 294 (2019)

Typhoon Jebi in 2018 caused severe damage along areas of Osaka Bay, Japan. After the storm, a Japan Society of Civil Engineers (JSCE) coastal survey group surveyed the coastal impacts and recorded watermarks inside Osaka Bay and along the Pacific. The maximum storm tide recorded by a tide gauge was 3.29 m at the Osaka Tide Station, which is a historical high for Osaka Bay. Coastal flooding consisted of both storm surge and wave run-up in almost all locations, with flooding exceeding 5 m and 12 m in elevation from mean sea level in the inner parts of Osaka Bay and along the Pacific coast, respectively. Coastal damage was severe in areas located outside of coastal barriers, such as ports and harbors, while residential areas were mainly well protected and spared due to coastal protection systems. In addition, some inland flooding occurred in the Kobe-Ashiya regions due to the storm surge propagating up several small rivers. This survey report summarizes the findings of the post-event survey by JSCE and analyzes the relation between maximum water level and resulting damage.

Low-frequency Catastrophic Coastal Disaster Events around Tonga: Survey of Coastal Boulder Distribution on Tongatapu Island and Analysis Using Stochastic Modelling of Tropical Cyclones

S. NAKAJO, J. NINOMIYA

Proceedings of the 29th International Ocean and Polar Engineering Conference, (2019)

A field survey of the coastal boulder distribution on Tongatapu Island was performed to obtain evidence of the old coastal disaster. The development potential of the tropical cyclone around this area was estimated using the stochastic tropical cyclone model. Thirty-eight boulder datasets, including boulder information not reported in previous studies were collected. Information concerning historical tropical cyclone data is very limited for the assessment of the low-frequency disaster event. A stochastic model was applied to generate a 25,000-year simulation of the tropical cyclone. If the Haiyan-like tropical cyclone attacks the Tongatapu Island, most boulders would be transported by high waves. According to the result of the frequency analysis of this study, this is not an entirely unlikely situation. The strong tropical cyclone often transverses to the Southeast around the Tongatapu Island. These characteristics are in rough agreement with the fact that the boulder distribution aggregates to the northwest coast of the Tongatapu.

Characteristics of Air-water CO₂ Exchange at the Yamato River Mouth by Continuous Water Quality Monitoring

Toru ENDO, Hironobu IMAYOSHI and Noriko HARADA

Journal of Japan Society of Civil Engineers, Ser. B2 (Coastal Engineering), Vol. 75, No. 2, I_1165-I_1170 (2019) (in Japanese).

Water quality monitoring surveys were carried out for every season at the mouth of the Yamato river in order to examine the air-water CO₂ exchange characteristics in the urban estuarine area. In addition, we obtained a regression equation between the electrical conductivity (EC) and the total alkalinity (TA) based on the relationship between EC and TA of the water sampled at some points of Yamato river in order to estimate the TA required for calculation of the partial pressure of CO₂ in water (pCO₂) from the monitoring data of EC.

The pCO_{2w} had large daily fluctuations in summer and fall, but the pCO_{2w} had small values and small daily fluctuations in winter. As a result of multiple regression analysis of pCO_{2w} and the observation items, the air-water CO₂ exchange depended on the change in salinity due to the tidal change and the change in pH due to the photosynthesis and the respiration. The averaged air-water CO₂ flux was 7.9 ± 0.6 CO₂/m²/hr in spring, 2.90 ± 0.7 CO₂/m²/hr in summer, 16.2 ± 1.3 CO₂/m²/hr in fall, -4.2 ± 0.5 CO₂/m²/hr in winter, and the Yamato river estuarine area acted net CO₂ sources except in winter.

Air-sea CO₂ Exchange and dissolved Inorganic Carbon in an Inner Part of Osaka Bay, Japan

Toru ENDO, Junpei SHIMANO, Noriko HARADA, Daiki SAKAI, Ryuichi FUJIWARA

Proceedings of the 10th International Conference on Asian and Pacific Coasts, 1073-1079. (2019)

The carbon captured by coastal oceans and ecosystems called "blue carbon" is attracting attention to reduce greenhouse gas. Recently, field surveys on air-sea CO₂ exchange have been conducted in various coastal seas to reveal the blue carbon function. In this study, we investigated the vertical distribution of the dissolved inorganic carbon (DIC) system in the inner part of Osaka Bay to reveal the air-sea CO₂ exchange characteristics in port and harbor area. Field surveys were conducted on a vertical seawall in Naruo-hama of Osaka Bay, Japan, during 12 months from November 2014 to October 2015 and during summer from August to September 2016. The vertical distributions of DIC and pH were measured on site, and the CO₂ partial pressure in water (pCO_{2w}) was calculated based on carbon acid equilibrium. Water temperature, salinity and DO were also measured to examine the relationships the vertical distribution of DIC system and water mass structure. Furthermore, the air-sea CO₂ flux (F_{CO2}) was estimated to examine the characteristics of the air-sea CO₂ exchange. DIC ranged from 787 to 2,111 μmol kg⁻¹, with seasonal and vertical change. DIC in the bottom layer increased during high water temperature period due to CO₂ production by respiration and decomposition, and DIC accumulated along with formation density stratification. The correlation between DIC and pCO_{2w} in surface layer was smaller than that in bottom layer because surface pCO_{2w} fluctuated due to inflow of river water or seawater mixing. This study area acts as CO₂ sinks under calm conditions (F_{CO2} = -3.4 mmol-C m⁻² d⁻¹), however the site acts CO₂ sources (1) when density stratification was relaxed (F_{CO2} = 2.1 mmol-C m⁻² d⁻¹); (2) when water was mixed by disturbance such as typhoon (F_{CO2} = 1.3 mmol-C m⁻² d⁻¹); and (3) when it rained (F_{CO2} = 15.5 mmol-C m⁻² d⁻¹).

Study on the Functions of Groins in Incubating Waterside Spaces: A Proposal for Planning and Maintenance to Generate Diversity of Waterside

Yasumasa FUKUSHIMA, Takashi UCHIDA

Society of Environmental Conservation engineering, Journal of Environmental Conservation engineering, Vol.48, No.4, pp.34-42, (2019) (in Japanese)

River management in recent years involves measures for waterside management, emphasizing the environment and its beneficial use as well as flood control and irrigation. Taking part in the trend of waterside management, this study, which focuses on the first author's engagement of planning so far, (1) evaluates the functions of groins in incubating waterside spaces concerning the aspects of environment, utilization, and management and (2) proposes specific measures for problems and points of attention regarding structural types, scales, and constituent materials in the planning phase to apply the groin function, based on our knowledge obtained by the process of planning, project implementation and deterioration due to aging, together with the result of our hearing survey towards the users.

Sightseeing Verbal Maps for Visually Impaired by Using Virtual Reality System Specialized in Sound

Yuta YANAGAWA, Takashi UCHIDA, Hiroko MATSUMOTO

Japan Society of Civil Engineers, Proceedings of Infrastructure Planning, No. 59, pp.109_1-6 (2019) (in Japanese)

Visually impaired people can walk on the street using a voice AR application that replaces visual information and auditory information. However, there are always some risks. It is difficult for visually impaired people to use it safely in unfamiliar areas, and to understand voice guidance correctly.

This research tries a virtual reality system that reproduces sound of the city using in sound of virtual reality in indoor space and uses the voice AR application for the visually impaired people. We will improve the recording method and reproduction method of environmental sound and aim for the development to "sightseeing verbal maps."

Current and Future Situations of Automatic Driving in China and Japan

HAINAER BULATAI, Takashi UCHIDA

Osaka City University, Memoirs of the Faculty of Engineering, Vol. 60, pp.1-11 (2019)

Conducting social acceptance surveys in Japan and China requires understanding of the current situation of automatic driving technology and the difficulties posed by transmission of future technologies. To analyze the status quo and to assess differences in automatic driving in China and Japan, this research begins with assessment of the three basic technologies of automatic driving. Then identification technology, programming technology, and control technology are analyzed by comparing the equipment of intelligent auxiliary systems of companies in China, Japan, and the United States. By analyzing the current state of development, the company plans can indicate the future of automatic driving.

Case Study on the Daily Use of Two-rider Bicycles for Persons with Reduced Mobility by Welfare Service Providers

Takuya KONISHI, Nagahiro YOSHIDA

Japan Society of Civil Engineers, Journal of Japan Society of Civil Engineers, Ser. D3 (Infrastructure Planning and Management), Vol. 75, Issue 5, pp. I_1197-I_1203 (2019) (in Japanese)

It is demanded to realize the society anyone can travel freely, and the two-rider bicycle might be a potential, practical means of transportation for persons with reduced mobility (PRM). The purpose of this study is to understand the latent opportunities for use of two-rider bicycles by PRM and welfare service providers from the questionnaire and hearing survey, and to understand the influences of the daily use of two-rider bicycles by welfare service providers from the fact-finding case survey. The results confirmed that there were latent opportunities and some influences by PRM and welfare service providers, it might lead to promotion of using two-rider bicycle for PRM and welfare service providers.

A Study on the Effect of Motorcycle Traffic Safety Workshop for High School and University Students in Phnom Penh, Cambodia

Toshiki KOYANAGI, Nagahiro YOSHIDA, Yuto KITAMURA

Transportation Research Board (TRB) 98th Annual Meeting, Poster No. 19-01976, 13 pages (2019)

In Cambodia, motorcycle use has spread rapidly in recent years, and serious accidents involving motorcycles have increased. In particular, many young motorcyclists have been involved in traffic accidents, and various

issues in traffic safety are remained. To understand the current situations related to these issues in Phnom Penh, Cambodia, a video observation survey on driving situations of motorcycle users in high school and university were conducted. Based on the results, a traffic safety workshop was held to improve their risk perception ability and basic riding skills. In this study, a statistical analysis was conducted to compare driving behavior on arterial roads before and after the workshop. The results showed that some behavioral changes are considered to be effects of the traffic safety workshop, and especially, driving skill learning is thought to have had an effect on aggressive behavior and the risk perception training on defensive behavior.

Changes in Subjective and Objective Comfort for Pedestrians and Cyclists After Road-Space Reallocation: A Case Study of Midosuji, Osaka

Haruka KAWACHI, Pola, BERENT, Nagahiro YOSHIDA, Taku FUJIYAMA

The 13th International Conference of the Eastern Asia Society for Transportation Studies (EASTS), 10 pages (2019)

In Japan, a road space reallocation project on Midosuji, the main street in Osaka, started in 2017 based on the concept of human-centered urban space. The project has widened the space for pedestrians and cyclists and narrowed the carriageways. This is an effort to ensure the comfort of pedestrians and cyclists. The Level of Service (LOS) concept is often used to evaluate user comfort. However, there is a possibility that the LOS may not be able to fully provide comfort in a mixed space of both pedestrians and cyclists. This study investigated the actual situations of pedestrians and cyclists on Midosuji in order to widen the street for them. A questionnaire survey (subjective indicator) and a video survey (objective indicator) were compared based on three sections of the road: an undeveloped section, a developed section without rest spaces, and a developed section with rest spaces.

A Review of the Contents of Bicycle Use Promotion Plans in Local Governments

Katsumasa TATSUNO, Nagahiro YOSHIDA

Japan Society of Civil Engineers, Proceedings of Infrastructure Planning, No. 60, 4 pages (2019) (in Japanese)

In June 2018, Ministry of Land, Infrastructure, Transport and Tourism (MLIT) formulated “Bicycle Utilization Promotion Plan” with the aim of promoting the use of bicycles and increasing public interests by reducing the degree of dependence on automobiles. In addition, it was obliged for prefectures nationwide to formulate “Regional Bicycle Utilization Promotion Plan” according to the local situation, and it is gradually being formulated. At present, the contents of the Regional Bicycle Utilization Promotion Plan are entrusted to local governments. Therefore, in this study, we decided to focus on the features and differences of the plan contents in the country, prefectures, and municipalities, and the relevance of each other in promoting the use of bicycles. As a result, prefectures had a higher compliance rate than municipalities, and the compliance rate was lower for municipalities, but there were doing a lot of regional specific initiatives that differed from the measures of MLIT.

An Evaluation of Bicycle Class for Preschool Children using Balance Bicycles

Nagahiro YOSHIDA

Japan Society of Civil Engineers, Proceedings of Infrastructure Planning, No. 60, 4 pages (2019) (in Japanese)

Inspired by the Danish cycle education for children, Cycling Games events with children of 3-6 years on balance bicycles have been organized in several cities of Japan including Osaka, Kyoto, Kanazawa, Shizuoka, and Tokyo since 2016 in collaboration with Urban Cycle Planning-Cycling Embassy of Denmark. The Danish Cycling Games (DCGs) promoted by the Danish Cyclists’ Federation throughout Danish kindergartens and schools are based on the method “learning by playing”, these games are considered to develop the children’s motor skills and a sense of safety and make cycling fun. To recognize cycling classes as a part of education for children in Japan, it was necessary to clarify the following: suitability for each age group, effects of conceptualizing such a program, and differences from other similar programs. Therefore, we conducted a questionnaire survey for teachers from 74 institutions: 15 city-supported kindergartens and nurseries in Kyoto City and 59 city-supported kindergartens and nurseries in Shizuoka City after performing DCGs at each institution in 2018.

Evaluation of Road Space Reallocation Arrangement and Rest Space Installation for Pedestrians and Cyclists Using the Level of Service Concept on Midosuji Boulevard

Haruka KAWACHI, Nagahiro YOSHIDA, Pola BERENT

Osaka City University, Memoirs of the Faculty of Engineering, Vol. 60, pp.13-18 (2019)

The road space reallocation project on Osaka's main street, Midosuji, started in 2017 to realize the concept of human-centered urban spaces in response to the change of social trends and conditions. The pilot project has been undertaken to increase spaces for pedestrians and cyclists. While the "Level of Service" concept was widely employed to evaluate user comfort issues in the transportation field, it is unknown whether it could apply to these space differences and evaluate the reallocation effect correctly. In this study, we show the elements that are not expressed by the Level of Service and are directed towards a more realistic comfort assessment; for example, rest spaces in road designs, and the expected and necessary speed to avoid worsening traffic flow.

Vital Reactions as a Measure of Stress Levels in Bicycle Riders According to Degree of Task

Katsumasa TATSUNO, Nagahiro YOSHIDA

Osaka City University, Memoirs of the Faculty of Engineering, Vol. 60, pp.19-25 (2019)

In this study, the amount of stress felt by bicycle riders is analyzed to obtain a method for measuring the relationship between the stress factors of the rider and the rider reaction to the environment, particularly while riding in bike lanes. Several vital reaction indices are used in a variety of traffic environments with differing stress factors. This study examines individual differences to include the level of riding experience and complexity of bicycling tasks to better explicitly consider the differences in experience related to stress and the complexity of riding in each environment. We also compare the differences in the vital reaction by the influence of individual based on biking experience and complexity of biking tasks. Results indicated that during a ride in the bike lanes, multitasking induced higher values in all indices of vital reactions, compared with the responses recorded under single-task conditions. It was also found that the vital reactions in subjects who rode their bikes daily tended to be higher under all biking conditions compared with the reactions of those who rode bikes only occasionally.

Vital Reactions as a Measure of Stress Levels in Bicycle Riders According to Task Complexity

Katsumasa TATSUNO, Nagahiro YOSHIDA

The 8th International Cycling Safety Conference 2019, Brisbane, Australia, 18-20 November 2019.

There are various types of bicycle infrastructure, including separated and shared paths on sidewalks and roadways alongside other transportation modes. Although each type of bicycle path requires different skills and confidence from cyclists, interactions between user response and path conditions have not been captured well. Previous studies have shown that safety, stress, and comfort levels of cyclists affect route choice behaviours. In terms of stress response, researchers have developed evaluations of road conditions by measuring vital reactions using heart rate interval (RRI), Galvanic skin response (GSR), Electroencephalography (EEG), and Electromyography (EMG). While riding a bicycle in various conditions affects user response through vital reactions, few studies have considered the comprehensive relationship between stress response and the task intensity, as cycling requires physical activity under complex task conditions. Therefore, in order to obtain some basic insights on vital reactions associated with road conditions during bicycle use, an experimental observation of vital reactions using RRI, EMG, and GSR in two different designated courses that required different riding tasks considering individual riding experience was conducted. Subjects were five students with different frequencies of bicycle usage on a daily basis. Results indicated that vital reactions while riding on the paths requiring multitasking, such as movement among other bicycle users and tilting the vehicle during curved driving, showed an increase on all indices compared to the reactions under single-task conditions. In addition, it was found that the vital reactions in daily users tended to be larger under any driving conditions compared to the reactions of occasional users. With respect to the next step, additional observations on different roads under heavy traffic conditions will be measured, followed by an analysis of the interrelationship between riding situations associated with traffic conditions and vital reactions.

Total Organic Carbon in the Leachate from Highly Reactive Slaked Lime and Municipal Solid Waste Incineration Fly Ash

Satoshi MIZUTANI, Katsunori MATOZAKI, Yoshinori KANJO

Proceedings of The 10th Forum on Studies of Environmental and Public Health Issues in Asian Mega-cities (EPAM 2019), December 11–15, 2019, Gifu, Japan, (2019)

High levels of total organic carbon (TOC) are often detected in leachate from municipal solid waste incineration (MSWI) fly ash in Japan. In this study, the Characteristic and influences of highly reactive slaked lime for organic load in the leachate from MSWI fly ash are discussed. First, TOC in the leachates from 13 kinds of MSWI fly ash in Japan was measured. Ignition loss (IL) of each type of fly ash was also measured to

determine the content of organic matter. There was no relationship between TOC and IL. Higher TOC levels were detected in leachate only from fly ash from incinerators with dry-acid gas treatment systems (slaked lime injection system). This suggests that the TOC of the leachate from the abovementioned fly ash was derived from slaked lime for the neutralization of acid gas. Subsequently, 18 kinds of commercially available highly reactive slaked lime were obtained and the TOC of their solution was measured. The leached TOC from unit weight of the slaked lime was in the range of 0.04–6.56 mg/g. In contrast, normal industrial slaked lime and $\text{Ca}(\text{OH})_2$ reagent do not contain organic materials. Generally, there was a positive correlation between COD and TOC in slaked lime. TOC showed 60–80% of COD_{Mn} values. Furthermore, two kinds of COD, that is COD_{Mn} and COD_{Cr} , in the solution of each highly reactive slaked lime are measured, and the chemical degradability of the materials is studied. The ratio of difference between COD_{Cr} and COD_{Mn} in COD_{Cr} was 23.5–48.1% and it suggests that approximately a quarter to a half of leached TOC from highly reactive slaked lime were organic carbon with low chemical degradability.

Evaluation of Relationship between Businesses' Handled Amount and Released / Transferred Amount of Chemical Substances Aimed for Predicting Chemical Pollution due to Earthquake Disaster by Using PRTR Data

Ryusuke SUGIURA, Satoshi MIZUTANI, Satoshi NAKAMURA, Yusuke TAWA, Yoshinori KANJO

Proceedings of The 10th Forum on Studies of Environmental and Public Health Issues in Asian Mega-cities (EPAM 2019), December 11–15, 2019, Gifu, Japan, (2019)

It is important to estimate the degree of waste that may result from natural disasters such as large earthquakes and tsunamis to effectively plan for disaster waste management. More specifically, it is especially crucial to estimate the quantity of hazardous chemical waste that a disaster may yield to plan environmental protection measures and proper waste treatment. To estimate such a phenomenon, it is necessary to first determine the amount of chemical substance present in a specific area. Although information about the release and transfer of chemicals is published under the pollutant release and transfer register (PRTR) system, PRTR data does not mean existing amount of chemicals. Notably, while information about the release and transfer of chemicals is published nationwide under the PRTR system, that on the handling of chemicals is only available at the limited number of local governments level. This study estimates for Osaka Prefecture by calculating the ratio between the amount of chemical substances released and transferred and the amount of chemical substances handled, and discusses the differences by fiscal year and by regions (i.e., local government). The difference between the years proved smaller than that between local governments. This paper argues that the larger difference between regions is due to the differences in the types of industries or industrial processes in each area.

Relationship between Melting Temperatures and Inorganic Compositions of Sewage Sludge

Yoshinori KANJO, Yuuki MATSUZAKI, Takeki SASAGAWA, Naoya KOUUDA, Satoshi MIZUTANI

Proceedings of The 10th Forum on Studies of Environmental and Public Health Issues in Asian Mega-cities (EPAM 2019), December 11–15, 2019, Gifu, Japan, (2019)

In order to decrease the emission amount of N_2O gas, which is one of the typical greenhouse gases, from these combustors for sewage sludge, more than two million tons (dry weight) of sewage sludge generated from domestic wastewater in Japan is combusted over 850 Celsius degrees. But high temperature leads to the formation and accumulation of ash deposits on heat transfer surfaces and makes clogging in heat transfer equipment. This phenomenon is called fouling, and leads to break down of the combustion systems. In this study, we measured the melting temperatures with differential thermal analyzer (DTA) and inorganic compositions of sewage sludge discharged from two sewage treatment plants for 18 months. The results show that the melting temperatures of sewage sludge tend to decrease in dry season including with winter season. Especially for January and February in 2018, the melting temperatures of sewage sludge decreased around 800 Celsius degrees, which is lower than the combustion temperature. From the viewpoint of temperature, it was supposed that a portion of the sewage sludge ash in this period melted and formed ash deposits at the surface of combustor and heat transfer equipment. Judging from the results of relationship between melting temperature and inorganic contents of sewage sludge, the melting temperatures increased with the contents of aluminum and iron, and decreased with the contents of phosphorus and potassium. The silica contents did not affect the melting temperature but decreased the peak area obtained with DTA, which is proportional to the amount of melting materials. Therefore, it will be better to use inorganic flocculation agents such as poly-aluminum chloride or poly-ferric sulfate in dewatering process prior to combustors to prevent the formation of ash deposits.

Comparison and Evaluation of Adsorption Properties of Biochars for Hydrophilic Organic Chemicals

Hiroki UENO, Satoshi ENDO, Yoshinori KANJO

Proceedings of The 10th Forum on Studies of Environmental and Public Health Issues in Asian Mega-cities (EPAM 2019), December 11–15, 2019, Gifu, Japan, (2019)

In order to evaluate the contaminated water purification ability of biochar, which is various organic carbides, adsorption experiments were performed using linear alkylbenzene sulfonate (LAS). 9 kinds of biochar (1 type from natural wood, 2 types from sawdust, 2 types from bamboo, 1 type from sewage sludge and 1 type from chicken manure) and 2 kinds of activated carbons (One each from wood and sawdust) were used as adsorbents. The adsorption coefficient and surface area of each adsorbent were measured, and adsorption isotherms were created and compared. A positive correlation was observed between the adsorption coefficient and the surface area regardless of the raw material and carbonization temperatures. Moreover, the common logarithm of the adsorption coefficient of Sawdust Charcoal produced at a carbonization temperature of 800°C was about 5.6, almost the same as that of activated carbon. As the LAS concentration increased, the biochar adsorptivity decreased within the experimental range, but the adsorptivity of activated carbon did not decrease. When the pH of the suspension solutions of adsorbents was measured, the pH was alkaline in all suspension solutions. Therefore, assuming the actual environment, the adsorption experiment was conducted by adjusting the pH of the suspension to around neutral. As a result, around neutral pH, the adsorption coefficient of activated carbon is about 2.4 times that at alkaline pH. However, in the case of Sawdust Charcoal, the adsorption coefficient at neutral pH was about 1/10. The adsorptivity of Sawdust Charcoal decreased at high concentrations of LAS or under neutral pH. The upper limit of environmental standards for LAS aquatic life conservation was 0.05 mg/L in Japan, and Sawdust Charcoal seemed to be useful in the actual environment.

Determination of Effective Diffusion Coefficient of Sodium in Municipal Solid Waste Incineration Bottom Ash by Diffusion Tube Test

Satoshi MIZUTANI, Ryotaro NAOI, Saki AIHARA, Koji ITO, Yoshinori YABUKI, Yoshinori KANJO

Proceedings of the 3R International Scientific Conference on Material Cycles and Waste Management (3RINC2020), March, Tsukuba, Japan (2020)

In order to evaluate the transport of harmful substances in landfills, we attempted to measure the diffusion coefficient in incinerated ash. The municipal waste incineration bottom ash to which sodium chloride was added was filled into a polyethylene tube, allowed to stand for 5 days, and then sliced thinly to analyze the sodium concentration. Based on the results of the experiment, a concentration profile was drawn, and the diffusion coefficient obtained by an approximation method to the theoretical equation of the diffusion phenomenon was $pDe = 9.13$. Since the diffusion coefficient was considered to be a reasonable value, this estimation method was considered to be useful.

Visualization of Chemical Substances Information by GIS Aimed for Predicting the Chemically Contaminated Wastes Generation due to Great Earthquake Disaster

Ryusuke SUGIURA, Satoshi MIZUTANI, Yusuke TAWA, Satoshi NAKAMURA, Yoshinori YABUKI, Kazushi NORO, Yoshinori KANJO

Proceedings of the 3R International Scientific Conference on Material Cycles and Waste Management (3RINC2020), March, Tsukuba, Japan (2020)

When a large-scale earthquake or tsunami occurs, hazardous chemical substances used in business establishments may leak, pollute the surrounding environment, and generate the chemically contaminated wastes. Therefore, estimating the location of chemical substances, the amount that can be leaked, and the amount of generated the chemically contaminated wastes is important in formulating a disaster waste disposal plan. In this study, the information on chemical substance amounts and handling place published in a chemical substances management system, pollutant release and transfer register (PRTR) system, was visualized using GIS. Chemical substances subject to the PRTR system were classified according to their state of ordinary temperature and pressure, and physical/chemical properties (specific gravity, vapor pressure, and solubility), assuming how the chemically contaminated wastes would be generated by earthquakes and tsunamis. Furthermore, when the amounts of released/transferred for each classified substance were shown on a map, the distribution was different from the map in which those amounts for all substances were plotted. From this, the necessity to grasp information based on the characteristics of chemical substances was confirmed.

Leaching Behavior of Lead and Cadmium from Municipal Solid Waste Incinerator Fly Ash Stabilized by Chemical Agents 24 Years Ago

Shota MASAKI, Satoshi MIZUTANI, Yoshinori KANJO, Shin-ichi SAKAI

Proceedings of the 3R International Scientific Conference on Material Cycles and Waste Management (3RINCs2020), March, Tsukuba, Japan (2020)

To confirm the long-term metal-stabilizing effects of chemical agents used 24 years ago, a Japanese standard leaching test (JLT-13) and pH-dependent test were conducted on municipal solid waste incinerator fly ash. The results were compared with previous test results. Based on the JLT-13 results, the pH decreased in nearly all samples. For some materials, the leached cadmium concentration increased. From the results of the pH-dependent test, the rough shape of the lead and cadmium pH-dependent curves were similar to those of past samples. It was confirmed that the stabilizing effect was generally maintained for 24 years. Particularly for one fly ash sample stabilized with an inorganic chemical agent, it was confirmed that lead mineralization had progressed and the stability under acidic conditions had increased. However, for the stabilized samples with a certain chelating agent, the lead and cadmium leachate concentrations increased under acidic conditions.

List of Presentations at International Conferences

Presenters are underlined in the list of authors.

[†]Undergraduate or graduate students of the Faculty of Engineering, Osaka City University

Mechanical and Physical Engineering

Mechanical Engineering

Effect of Pickling and Mechanical Grinding on Initiation of Biofilm and Microbially Influenced Corrosion of Stainless Steel Weldments

Hiroshi KAWAKAMI, Takuhiro WADA[†], Takeshi NAKANISHI, Kingo ARIYOSHI, Kouichi TSUJI, Masaya KITAMURA and Yasushi KIKUCHI

NACE East Asia & Pacific Area Conference, Yokohama, Japan, November 11-14, 2019.

Temperature Dependence of the Growth Process of Grain Boundary Steps Formed on Ultra-precision Finished Polycrystalline Copper Surface

Tatsuya USUKI[†], Hiroshi KAWAKAMI, Tatsuya TOKUYAMA[†] and Tsukasa MIYAGAWA[†]

The 8th International Conference of ASPEN, Asian Society for Precision Engineering and Nanotechnology, Matsue, Japan, November 12-15, 2019.

Localized Deformation of Electrodeposited Ni-Co-Cu/Cu Multilayered Films Subjected to Compressive Straining

Yoshihisa KANEKO, Tomohiro KUBOMAE[†] and Makoto UCHIDA

Materials Research Meeting 2019, Yokohama, Japan, December 10-14, 2019.

Dependence of Vickers Hardness on Layer Thickness in Electrodeposited Ni-Co-Cu / Cu Multilayered Films

Hiroyuki HAGIWARA[†], Naofumi KAWAKAMI[†], Yoshihisa KANEKO and Makoto UCHIDA

Materials Research Meeting 2019, Yokohama, Japan, December 10-14, 2019.

Numerical Analyses of Micro- to Macroscopic non-Uniform Deformation During Plane Strain Compression Using Second-Order Homogenization Method

Masashi SAKAMOTO[†], Takayuki OTSUKA and Makoto UCHIDA

International Conference on Computational Plasticity 2019 (Complas 2019), Barcelona, Spain, September 3-5, 2019.

Effect of Metal Type and Heating Condition on Joint Strength of Metal and Polymer Prepared by Arc Welding

Hiroaki KOBAYASHI[†], Makoto UCHIDA, Houichi KITANO and Yoshihisa KANEKO

The 5th International Symposium on Visualization in Joining & Welding Science through Advanced Measurements and Simulation, Osaka, Japan, November 21-22, 2019.

Applied Physics and Electronics

Tunneling of plasma bullets through a dielectric plate and its application to quick hydrophilicity enhancement of bone-regeneration scaffolds

Tatsuru SHIRAFUJI, Yuki HAMAMOTO[†], Ryo MATOBA[†], Jun-Seok OH, Ryo SUGAMA (Faculty of Medicine), Kumi ORITA (Faculty of Medicine), Hiromitsu TOYODA (Faculty of Medicine)

12th International Symposium on Advanced Plasma Science and its Applications for Nitrides and Nanomaterials / 13th International Conference on Plasma-Nano Technology & Science, March 8-11, 2020, Nagoya, Japan (Poster)

Plasma generated reactive species deliver onto human dermis model

Kenji MAEDA[†], Ikumi TAKAHASHI[†], Koji YAMANE[†], Miki YANAGISAWA[†], Hiroshi KAWAKAMI, Tatsuru SHIRAFUJI, Jun-Seok OH

12th International Symposium on Advanced Plasma Science and its Applications for Nitrides and Nanomaterials / 13th International Conference on Plasma-Nano Technology & Science, March 8-11, 2020, Nagoya, Japan (Poster)

Contribution of reactive nitrogen species to sterilization of radical-activated water

Naoyuki IWATA (Meijo University), Vladislav GAMALEEV (Meijo University), Jun-Seok OH, Takayuki OHTA (Meijo University), Masaru HORI (Nagoya University), Masafumi ITO (Meijo University)

The 11th Asia-Pacific International Symposium on the Basics and Applications of Plasma Technology, December 11-14, 2019, Kanazawa, Japan

Developing pressure gradient sputtering system (PGS)

Ken YONEZAWA (Kenix Corporation), Hiroki OOTA (Kenix Corporation), Jun-Seok OH, Kazunori KOGA (Kyushu University), Tatsuyuki NAKATANI (Okayama University of Science), Masafumi ITO (Meijo University), Masaharu SHIRATANI (Kyushu University)

The 11th Asia-Pacific International Symposium on the Basics and Applications of Plasma Technology, December 11-14, 2019, Kanazawa, Japan (Poster)

Humid air discharge characterization using atmospheric-pressure plasma reactor

Yusuke SASAKI[†], Tatsuru SHIRAFUJI, Jun-Seok OH

The 11th Asia-Pacific International Symposium on the Basics and Applications of Plasma Technology, December 11-14, 2019, Kanazawa, Japan (Poster)

Spatial distribution of He in a porous scaffold irradiated with He APPJ

Tatsuru SHIRAFUJI, Jun-Seok OH, Ryo SUGAMA (Faculty of Medicine), Kumi ORITA (Faculty of Medicine), Hiromitsu TOYODA (Faculty of Medicine)

The 11th Asia-Pacific International Symposium on the Basics and Applications of Plasma Technology, December 11-14, 2019, Kanazawa, Japan (Poster)

H₂O₂ synthesis using 3D integrated micro solution plasma and improvement of its efficiency by combining with ion exchange resin

Tatsuru SHIRAFUJI, Shyoma MIYAMOTO[†], Jun-Seok OH

Materials Research Meeting 2019, December 10-14, 2019, Yokohama, Japan (Invited)

Atmospheric-pressure plasma reactor generated plasma-activated water

Jun-Seok OH, Soshi IMAI[†], Yusuke SASAKI[†], Tatsuru SHIRAFUJI

Materials Research Meeting 2019, December 10-14, 2019, Yokohama, Japan (Invited)

Gas-liquid interfacial plasma polymerization of EDOT

Shoyta HIRANO[†], Jun-Seok OH, Ryo KONISHI[†], Tatsuru SHIRAFUJI

Materials Research Meeting 2019, December 10-14, 2019, Yokohama, Japan (Poster)

Renovation of water permeability of a continuous porous dielectric using propagation of plasma bullets

Yuki HAMAMOTO[†], Tatsuru SHIRAFUJI, Ryo MATOBA[†], Jun-Seok OH

Materials Research Meeting 2019, December 10-14, 2019, Yokohama, Japan (Poster)

Growth promotion effect of oxygen-radical-treated amino acids solutions

Naoyuki IWATA (Meijo University), Vladislav GAMALEEV (Meijo University), Hiroshi HASHIZIME (Nagoya University), Jun-Seok OH, Takayuki OHTA (Meijo University), Kenji ISHIKAWA (Nagoya University), Masaru HORI (Nagoya University), Masafumi ITO (Meijo University)

The 29th Annual Meeting of MRS-J, November 27-29, 2019, Yokohama, Japan

Considerations in the development of plasma sources for cosmetic science

Jun-Seok OH, Endre J. SZILI (University of South Australia)

The 1st International Meeting on Plasma Cosmetic Science, November 25-27, 2019, Orleans, France (Poster)

Plasma-bullet propagation behind a dielectric plate irradiated with an APPJ

Tatsuru SHIRAFUJI, Ryo MATOBA[†], Yuki HAMAMOTO[†], Jun-Seok OH, Ryo SUGAMA (Faculty of Medicine), Kumi ORITA (Faculty of Medicine), Hiromitsu TOYODA (Faculty of Medicine)

The 41st International Symposium on Dry Process, November 21-22, 2019, Hiroshima, Japan (Poster)

Discharge characteristics of Ar atmospheric-pressure plasma

Soshi IMAI[†], Ikumi TAKAHASHI[†], Yusuke SASAKI[†], Tatsuru SHIRAFUJI, Jun-Seok OH

The 41st International Symposium on Dry Process, November 21-22, 2019, Hiroshima, Japan (Poster)

Longer-lived chemistry and antimicrobial activity of plasma activated water

Jun-Seok OH, Naoyuki IWATA (Meijo University), Giichiro UCHIDA (Meijo University), Kosuke TAKENAKA (Osaka University), Yuichi SETSUHARA (Osaka University), Mineo HIRAMATSU (Meijo University), Masafumi ITO (Meijo University)

The 5th International Symposium on Visualization in Joining & Welding Science through Advanced Measurements and Simulation & The 8th International Conference of Welding Science and Engineering, November 21-22, 2019, Osaka, Japan (Invited)

Electrical and Information Engineering

Spin Transport in Thermally-Evaporated Polyacene Films and the Derivative Films Induced by the Spin-Pumping

Yuji TANAKA[†], Taisei KONO[†], Masahiro YAMAMOTO[†], Yoshio TEKI (Graduate School of Science, OCU), Hiroaki TSUJIMOTO, Eiji SHIKOH

64th Annual Conference on Magnetism and Magnetic Materials, Las Vegas, USA, November 4-8 (2019).

Applied Chemistry and Bioengineering

Workshop Instructor on “Micro XRF”

K. TSUJI

69th Annual Conference on Applications of X-ray Analysis Denver X-ray Conference, Rockville, Maryland, U.S.A., 3-7 August 2020 (invited)

Optimal sample preparation for TXRF analysis depending on the sample solutions

T. MATSUYAMA, K. TSUJI

69th Annual Conference on Applications of X-ray Analysis Denver X-ray Conference, Rockville, Maryland, U.S.A., 3-7 August 2020 (invited)

X-ray Elemental and Structural Imaging Techniques by using Highly Sensitive X-ray Camera

K. TSUJI, R. OZEKI[†], T. MATSUYAMA, M. YAMANASHI

69th Annual Conference on Applications of X-ray Analysis Denver X-ray Conference, Rockville, Maryland, U.S.A., 3-7 August 2020 (poster)

X-rays analytical techniques for determining trace elements in a single human hair and atmospheric aerosols

T. MATSUYAMA, T. HAYAKAWA, H. YAMAGUCHI, K. TSUJI

69th Annual Conference on Applications of X-ray Analysis Denver X-ray Conference, Rockville, Maryland, U.S.A., 3-7 August 2020 (poster)

Improvement of Detection Limit for Particle Contamination by Confocal Configuration in X-ray Fluorescence Microscope

H. NAKANO, S. KOMATANI, T. MATSUYAMA, K. TSUJI

69th Annual Conference on Applications of X-ray Analysis Denver X-ray Conference, Rockville, Maryland, U.S.A., 3-7 August 2020 (poster)

Development of confocal line X-ray fluorescence instrument and application to layer structure samples

S. SONODA[†], H. NAKANO, T. MATSUYAMA, K. TSUJI

69th Annual Conference on Applications of X-ray Analysis Denver X-ray Conference, Rockville, Maryland, U.S.A., 3-7 August 2020 (poster)

Multicolor Emission Properties of Polystyrene with Difluoroboron Avobenzone Complexes at Side Chains in Solid State

Katsuya SHIMIZU[†], Arisa OKUMA (Shinshu University), Shiho KATSUMI (Shinshu University), Fuyuki ITO (Shinshu University), Seiya KOBATAKE

International Research Conference on Engineering and Technology, Seoul, Korea, January 7-9, 2020 (poster)

Outer membrane vesicles of Gram-negative bacteria and its application to microbial biotechnology

Yoshihiro OJIMA, Masayuki AZUMA

ICGEB-IMBT Workshop2019, I5, Hanoi, Vietnam, November 5-6, 2019

Urban Engineering

Urban Design and Engineering

Vital Reactions as a Measure of Stress Levels in Bicycle Riders According to Task Complexity

Katsumasa TATSUNO[†], Nagahiro YOSHIDA

The 8th International Cycling Safety Conference 2019, Brisbane, Australia, 18-20 November 2019.

Extreme Wave and Storm Surge Assessment Due to Typhoon and Low Pressure Weather System on the Sanin Coast, Japan

Sooyoul KIM, Keishiro CHIYONOBU, Junichi NINOMIYA, Sota NAKAJO, Tomohiro YASUDA, Takao OTA

The 16th Annual Meeting, AOGS, OS18-A006, Singapore, July 28 – August 2, 2019

The Propagation Characteristics of Micro-barometric Wave Estimated from Observational Data and the Response of Meteotsunami in the West Kyushu Island

Sota NAKAJO

The first World Conference on Meteotsunamis, Split, Republika Hrvatska, May 8-11, 2019

Low-frequency Catastrophic Coastal Disaster Events around Tonga: Survey of Coastal Boulder Distribution on Tongatapu Island and Analysis Using Stochastic Modelling of Tropical Cyclones

Sota NAKAJO, J. NINOMIYA

The 29th International Ocean and Polar Engineering Conference, Honolulu, USA, June 17-21, 2019.

Air-Sea CO₂ Exchange and Dissolved Inorganic Carbon Distribution in an Inner Part of Osaka Bay, Japan

Toru ENDO, Junpei SHIMANO, Noriko HARADA[†], Daiki SAKAI, Ryuichi FUJIWARA

10th International Conference on Asian and Pacific Coasts, 2019, Hanoi Vietnam, September 25-28, 2019.

